Doctoral thesis

Electroweak baryogenesis in a complex singlet extension of the Standard Model with degenerate scalars

Chikako Idegawa

Graduate school of Humanities and Sciences,
Ochanomizu University, Tokyo 112-8610, Japan

Acknowledgement

First of all, I would like to express my sincere gratitude to my advisor, Prof. Gi-Chol Cho, who has given me much guidance in my research in particle physics. I am also very grateful to Dr. Eibun Senaha, who has guided me through most of my research. Furthermore, I am grateful to members of theoretical particle physics group in Ochanomizu University, Ms. Rio Sugihara and Ms. Rie Inumiya for their fruitful collaboration. During my doctoral studies, my work is supported by JST, the establishment of university fellowships towards the creation of science technology innovation, Grant No. JPMJFS2113, by Fujukai Foundation and by Ochanomizu University Nagase Research Scholarship. Finally, I would like to thank my family for their understanding and warm support.

Abstract

The Standard Model (SM) of elementary particles was once completed with the discovery of the Higgs boson in 2012. The SM has demonstrated some success in providing experimental predictions, but there are several phenomena that cannot be explained by the SM. Example includes the origin of baryon asymmetry, identity of dark matter (DM). Therefore, the SM needs to be extended. On the other hand, it is also true that the SM accurately describes the behavior of elementary particles at the present time, so I treat the extended scalar (Higgs) model on the basis of "minimality," which is the smallest extension to the SM.

Various possible scenarios have been considered to explain baryon asymmetry, including leptogenesis and neutrino oscillations. Among many scenarios, I now attempt to generate baryon numbers using electroweak baryogenesis (EWBG), which is closely related to Higgs physics, in order to use the extended Higgs model. This scenario is the most testable and attractive because, as the name suggests, the energy scale is on the electroweak scale. Since the CP violation (CPV) that the SM contains is not sufficient to drive EWBG, the introduction of new sources of CPV is needed for models beyond the SM.

Possible DM candidates include warm DM, which has small mass and relativistic motion, and cold DM, which has relatively large mass and non-relativistic motion. Among cold DM, weekly interacting massive particle (WIMP), which can thermally explain the observed DM relic density, is a representative candidate. This study deals with WIMP-DM with a mass of $\mathcal{O}$(10-100) GeV. WIMP-DM search experiments include direct detection experiments in which scattering with nucleons is observed. However, no DM signal has yet been found, and strong constraints have been placed on the scattering cross section. Thus, constructing a model that includes WIMP-DM without violating this bound is a major challenge.

We consider the extension of the SM by adding one complex singlet scalar field (complex singlet extension of the SM : CxSM). This series of studies can be divided into two main parts: the CP-conserving CxSM and the CP-violating CxSM. First, In the CP-conserving CxSM, the imaginary part of the newly introduced scalar field behaves as a DM. In addition, the SM Higgs and the real part of the singlet scalar mix and two Higgs bosons appear. When the masses of these two Higgs bosons are degenerate, the strong constraints from the direct detection experiment can be satisfied, which we call the degenerate scalar scenario. On the other hand, a strong first-order electroweak phase transition

(EWPT) is essential for the realization of EWBG, and we investigate its feasibility in the degenerate scalar region.

Next, we consider the CP-violating CxSM for the completion of EWBG. In this case, there are three Higgs bosons and the imaginary part of the singlet scalar no longer behaves as a DM. We first investigate the effect of the CPV phase of the scalar potential on EWPT and estimate the gravitational waves originating from EWPT. We then introduce higher dimensional operators to propagate the CPV phase to the SM sector and check its consistency with electric dipole moment experiments which is sensitive to CPV. Finally, the generated baryon number is estimated.

Contents

Chapter 1

Introduction

The Standard Model (SM) in particle physics is a successful theory and can explain many results in various experiments/observations, including collider experiments and cosmological observations. On the other hand, several phenomena have been observed that cannot be explained by the SM, such as the baryon asymmetry of the universe (BAU) and the identity of dark matter (DM). Thus, despite its success, the SM has been forced to expand. The construction of models involving physics beyond the SM (BSM) that can explain the unsolved problems and the scrutiny of the testability for them is an important challenge for particle physics.

The Higgs boson was discovered by the Large Hadron Collider (LHC) experiment in 2012 [1, 2]. The SM contains one isospin doublet scalar field, which is the Higgs field. However, there is no principle that limits the number of Higgs fields or their structure, and the existence of one Higgs doublet in the SM is only an assumption. Therefore, in considering the BSM model, it is a natural procedure to extend the Higgs sector. Extended Higgs models include the two Higgs doublet model and models that add a singlet scalar field to the SM.

Of the outstanding issues that I focus on in this study, I first discuss the BAU. Every elementary particle has an antiparticle, as the antiparticle of a quark is an antiquark. The baryon number is one of the quantum numbers, and is assigned $1/3$ for quarks and $-1/3$ for antiquarks. The universe began with the Big Bang, and the hot and dense universe cooled and expanded rapidly. At the beginning of the universe, there were equal amounts of particles and antiparticles and the overall baryon number was zero. But at some point, particles became a little more abundant. Then, as the universe cooled, particles and antiparticles were annihilated, and now only particles remain. The process from zero baryon number to positive baryon number is called baryogenesis. Evidence for the BAU comes from two observations. One is Big Bang Nucleosynthesis (BBN), which represents the formation of nuclei of light elements [3]. The physical quantity used to describe the degree of the BAU is the ratio of the baryon number density n_B to the photon density n_γ. η_B is given by the ratio of n_B to n_γ as $\eta_B^{\rm BBN} = (5.8 - 6.5) \times 10^{-10}$ (95% CL). n_B is also determined by the

Cosmic Microwave Background (CMB) observations [4]. The baryon-to-photon ratios are given as $\eta_B^{\rm CMB} = (6.105 \pm 0.055) \times 10^{-10}$ (95% CL). It can be seen that the two observations provide consistent values and baryogenesis is the correct explanation for these values.

There are three necessary conditions to realize baryon asymmetry which are called Sakharov's conditions [5] and consist of (1) Baryon number violation, (2) C and CP symmetry violation, and (3) Out of thermal equilibrium. Many scenarios have been proposed that satisfy these conditions, e.g., GUT baryogenesis [6, 7], Electroweak Baryogenesis (EWBG)[8], Leptogenesis [9]. Of these scenarios, EWBG is the most testable because it produces baryon numbers at relatively low energy scales. Furthermore, EWBG is closely related to the Higgs boson and thus holds the key to the elucidation of Higgs physics. In the framework of the SM, each of the Sakharov's conditions is explained by the following phenomena; (1) Baryon number violation : sphaleron process, (2) C and CP symmetry violation : chiral gauge interaction, the Cabibbo-Kobayashi-Maskawa (CKM) matrix, and (3) Out of thermal equilibrium : strong first-order electroweak phase transition (EWPT). However, EWBG cannot be achieved using the SM for two reasons. First, CP violation (CPV) introduced by the complex phase of the CKM matrix is too small [10, 11, 12, 13]. The second problem is the inability to achieve a strong firs-order EWPT in the SM with the observed 125 GeV Higgs boson [14, 15, 16, 17]. Therefore, since EWBG cannot be realized in the SM, it is necessary to consider BSM model that extends the Higgs sector and has new CPV phases.

Next, a brief review of DM is provided. DM has been suggested to exist by cosmological observations, but is impossible to observe optically. DM accounts for about 26.8 % of all matter and energy in the universe. In addition, several properties of DM are known from cosmological observations; (1) massive, (2) not interact electromagnetically, and (3) stable. The SM does not contain particles that satisfy all of these properties, so the SM expansion is necessary in terms of DM. Among the various DM candidates, weakly interacting large particle (WIMP) is one of the most attractive candidates. It is known to be in good agreement with data on the thermal abundance of DM from the CMB observations (the so-called "WIMP miracle").

One of the WIMP-DM search experiments is a direct detection experiment. DM from space collides with liquid Xe stored in an underground laboratory, and the signal emitted when the nucleus recoils is detected. Direct detection experiments are currently being attempted around the world. Despite improvements in measurement accuracy, no DM signal has so far been observed, and in particular, the recent LUX-ZEPLIN (LZ) experiment provides strict upper bounds on the spin-independent cross section between DM and nucleons [18]. Thus, Constructing a model that includes DM without violating this bound is a major challenge.

In order to satisfy the severe constraints of direct detection experiments, it has been assumed that either (1) the mass scale of DM is too large to be reached experimentally, or (2) the coupling constants for the interactions between DM and the SM particles are too small to detect with

current experimental facilities. Both of these assumptions imply decoupling from the SM sector. Here, it is quite natural to ask about the possibilities other than (1) and (2) as conditions for a BSM model that is consistent with current experimental and observational results. In other words, we consider a BSM model in which the DM mass scale is within the range reachable by current experiments and the interactions are not suppressed.

In this study, complex singlet extension of the SM (CxSM) is used as a minimal extended Higgs mode [19, 20, 21]. As the name implies, the CxSM is the extension of the SM by adding the complex SU(2) gauge singlet scalar field S. Depending on whether the scalar potential of the CxSM is invariant or not under CP transformation, the discussion of DM and EWPT would change; since CPV is essential for the realization of EWBG, I discuss the CP-conserving CxSM as a first step and then evaluate the CP-violating CxSM.

When the CP-conserving CxSM is taken into account, the imaginary parts of S do not mix with the real part of S and the SM Higgs, and the stability of the imaginary parts of S is guaranteed, making it a DM candidate. On the other hand, the real part of S and the SM Higgs mix to form the mass eigenstates and two Higgs bosons appear. The scattering of DM and quarks in this model occurs with two Higgs bosons as mediator particles. It is known that when the masses of Higgs bosons are equal, this scattering is suppressed, which is consistent with the direct detection bound. This is called a degenerate scalar scenario.

The addition of the new scalar field would be beneficial to EWPT. In general, thermal loops make a significant contribution to EWPT, but in the CxSM, the structure of the tree-level potential, represented by the mixing of the scalar singlet and doublet, is more important rather than this. However, the suppression mechanism of the degenerate scalar scenario and the strong first-order EWPT provide conflicting conditions for the parameters. Thus, we study the feasibility of strong first-order EWPT in a degenerate-scalar scenario in the CxSM.

In addition, two studies on the degenerate scalar scenarios will be presented. One is the application of the Multi-critical Point Principle (MPP) to the CxSM. The MPP discussed in this study chooses model parameters so that the two low-energy vacua realized by the scalar field are degenerate. We investigate the possibility that this predicts the degenerate Higgs. The other concerns the origin of the degenerate scalar scenario. We study the origin of the cancellation mechanism of the degenerate scalar scenario and show that the operators describing the Higgs-singlet scalar mixing play essential role.

Next, for the BAU realization, the CPV phase is introduced into the scalar potential of the CxSM. In this case, there are three Higgs bosons and the imaginary part of S no longer behaves as a DM. We examine CPV effects on EWPT, and then find that the strength of the first-order EWPT would get weaker as the CPV effect becomes larger. Furthermore, as a phenomenological consequence of the first-order EWPT, we also evaluate gravitational waves (GWs). As a result,

GW amplitudes are diminished by the size of the CPV. Future GW experiments may shed light on CPV in the singlet scalar sector as well as the experimental blind spot due to the degenerate Higgs.

Finally we study the possibility of EWBG in the CxSM. In our setup, CPV is provided by dimensional-5 Yukawa interactions involving the complex scalar field. In contrast to previous studies in the literature, we exemplify a case in which a complex phase in the singlet scalar potential is transmitted to the fermion sector via the higher-dimensional operators and drives BAU. Experimental searches for CPV are essential for probing the EWBG possibility. This study focuses on an electric dipole moment (EDM) of the electron because the electron EDM are currently the most sensitive to CPV. We point out that the electron EDM can be suppressed due to the Higgs mass degeneracy and the presence of a new electron Yukawa coupling. Thus, viable parameter space for EWBG is still wide open for the latest experimental bound set by recent EDM experiments. Here, BAU is generated by using the Boltzmann equations which are based on the semi-classical force mechanism.

The CP-conserving CxSM study is based on [22, 23, 24] and that of the CP-violating CxSM is based on [25, 26]. The five papers I have submitted to the journal are a series of studies examining and validating the CxSM in terms of DM and EWBG, and this doctoral thesis includes quoted and reprinted portions of these. The structure of this thesis is as follows. Chapter 2 gives an overview of the SM. Chapters 3 and 4 discuss BAU and DM, phenomena that cannot be explained by SM. Chapter 5 presents the study of the CP-conserving CxSM, and Chapter 6 extends the previous model and presents the study of the CP-violating CxSM. Chapter 7 summarizes this thesis.

Chapter 2

Overview of the standard model

In this chapter, a review of the standard model (SM) is presented. First, I explain the particles included in the SM and the SM Lagrangian. Then, the Higgs mechanism and the electroweak symmetry breaking caused by it are described, and the masses of gauge bosons and fermions are expressed. Lastly, I describe the CKM matrix including the CP symmetry violating phases.

2.1 Components and Lagrangian

Four interactions, gravitational interaction, electromagnetic interaction, weak interaction, and strong interaction, are known to exist in nature. The SM of elementary particles describes the three interactions other than gravity. Glashow, Weinberg and Salam proposed a model that integrates the electromagnetic and weak forces (The unified model of electroweak interactions), and the addition of quantum chromodynamics describing strong force to it is called the SM.

The SM is a gauge theory that describes strong, electromagnetic, and weak interactions based on $\mathrm{SU}(3)_C \times \mathrm{SU}(2)_L \times \mathrm{U}(1)_Y$ gauge symmetry. As a consequence of gauge symmetry, there are gauge bosons mediating forces on quarks, leptons and Higgs bosons. $\mathrm{SU}(3)_C$ represents the symmetry corresponding to strong interactions and the gauge bosons are gluons. The electromagnetic and weak interactions are described by $\mathrm{SU}(2)_L \times \mathrm{U}(1)_Y$. This gauge symmetry is spontaneously broken by the Higgs field, leaving only $\mathrm{U}(1)_{EM}$. Three of the three gauge bosons in $\mathrm{SU}(2)_L$ and one in $\mathrm{U}(1)_Y$ become massive and mediate the weak interaction as $W^{\pm}, Z$ bosons. Furthermore, $\mathrm{U}(1)_{EM}$ represents the symmetry corresponding to the electromagnetic interaction and the gauge bosons are photons.

All particles that make up the SM are summarized in Fig. 2.1. The horizontal direction of quarks and leptons represents generations, and in the SM, the number of generations of quarks and leptons is 3. The vertical direction of quarks and leptons represents the difference in electric charge. For quarks, up (u), charm (c),top (t) have charge 2/3, down (d), strange (s), bottom (b)

quarks			leptons			Higgs boson
u	c	t	ν_e	ν_μ	ν_τ	h
d	s	b	e	μ	τ	
gauge bosons						
(electromagnetic) γ			(weak) $W^\pm$, Z			(strong) g

Table 2.1: Particles included in the SM.

	$Q = \begin{pmatrix} u_L \\ d_L \end{pmatrix}$	u_R	d_R	$L = \begin{pmatrix} \nu_L \\ e_L \end{pmatrix}$	e_R	$\varphi = \begin{pmatrix} \phi^+ \\ \phi^0 \end{pmatrix}$
spin	$\frac{1}{2}$	$\frac{1}{2}$	$\frac{1}{2}$	$\frac{1}{2}$	$\frac{1}{2}$	0
$SU(3)_C$	3	3	3	1	1	1
$SU(2)_L$	2	1	1	2	1	2
$U(1)_Y$	$\frac{1}{6}$	$\frac{2}{3}$	$-\frac{1}{3}$	$-\frac{1}{2}$	-1	$\frac{1}{2}$

Table 2.2: Quantum numbers for quarks, leptons, and Higgs field in the SM.

have charge -1/3. For leptons, electron neutrino (ν_e), muon neutrino (ν_μ), tauon neutrino (ν_τ) have no charge, electron (e), muon (μ), tauon (τ) have charge -1. In addition, gauge bosons mediating electromagnetic interactions is photon (γ), weak interactions are $W^\pm, Z$ bosons, and strong interactions is gluon (g).

In the SM, left-handed fermions are treated as $SU(2)_L$ doublet and right-handed fermions as singlet. Furthermore, the Higgs field is an $SU(2)_L$ doublet; the $SU(3)_C$ symmetry is characterized by color charge, the $SU(2)_L$ symmetry by weak isospin, and the $U(1)_Y$ symmetry by weak hypercharge. Furthermore, the generator of $U(1)_{EM}$ symmetry is charge Q and it is known that the following relation holds;

$$Q = I_3 + Y, \tag{2.1}$$

where I_3 is the third component of weak isospin, the generator of $SU(2)_L$. Assignments of quantum numbers to quarks, leptons, and Higgs field are shown in Table. 2.2.

The Lagrangian of the SM consists of the following elements;

$$\mathcal{L} = \mathcal{L}_{\text{kin}} + \mathcal{L}_{\text{Yukawa}} - V_{\text{Higgs}}, \tag{2.2}$$

where $\mathcal{L}_{\text{kin}}$ is kinetic terms for gauge fields, fermions and Higgs field, $\mathcal{L}_{\text{Yukawa}}$ is Yukawa interaction terms and V_{Higgs} is Higgs potential. Here, the Yukawa interaction terms and the Higgs potential are discussed in detail.

The interaction between quarks, leptons and the Higgs field is called the Yukawa interaction and is given by

$$-\mathcal{L}_{\text{Yukawa}} = f_u \bar{Q} u_R \phi^c + f_d \bar{Q} d_R \phi + f_e \bar{L} e_R \phi + \text{ h.c. } . \tag{2.3}$$

f_u, f_d and f_e is Yukawa coupling constants of up-type quark, down-type quark and electron. The introduction of $\phi^c \equiv i\sigma_2 \phi^*$ preserves the $\mathrm{U}(1)_Y$ gauge invariance, where ϕ^* is complex conjugate of the Higgs field ϕ and σ_2 is the second component of Pauli matrices.

The term given by the self-interaction of the Higgs field is called the Higgs potential, which takes the form;

$$V = \mu^2 \phi^\dagger \phi + \lambda (\phi^\dagger \phi)^2. \tag{2.4}$$

For the potential to have a finite minimum, $\lambda > 0$ is required. If $\mu^2 > 0$, the potential takes minimum value at $\phi = 0$. On the other hand, if $\mu^2 < 0$, the potential has extrema other than $V = 0$. When one such vacuum is chosen, $\mathrm{SU}(2)_L$ symmetry that the potential had is broken. This is called spontaneous symmetry breaking and will be explained in detail in the next section.

2.2 Higgs mechanism and spontaneous symmetry breaking

I consider the following $\mathrm{U}(1)_{EM}$ invariant Lagrangian;

$$\mathcal{L} = -\frac{1}{4} F_{\mu\nu} F^{\mu\nu} + |D_\mu \phi|^2 - V(\phi). \tag{2.5}$$

The strength of the gauge field $F_{\mu\nu}$ is given by $F_{\mu\nu} = \partial_\mu A_\nu - \partial_\nu A_\mu$, where A_μ is the electromagnetic field. The covariant derivative is $D_\mu \phi = (\partial_\mu - igA_\mu)\,\phi$. The Higgs potential $V(\phi)$ is given by Eq. (2.4). If $\mu^2 < 0$, when the scalar field takes the vacuum expectation value (VEV) as follows, the potential is minimized and spontaneously breaks the gauge symmetry;

$$\langle \phi \rangle \equiv \frac{v}{\sqrt{2}} \qquad \text{where} \quad v^2 = -\frac{\mu^2}{\lambda}. \tag{2.6}$$

The fluctuations of the scalar field from the VEV can be expressed as

$$\phi = \frac{v}{\sqrt{2}} + \frac{1}{\sqrt{2}} (\phi_1 + i\phi_2)\,, \tag{2.7}$$

where ϕ_1, ϕ_2 are real scalar fields. Then Eq. (2.5) eventually takes the form

$$\mathcal{L} = -\frac{1}{4} F_{\mu\nu} F^{\mu\nu} + \frac{1}{2} (\partial_\mu \phi_1)^2 + \frac{1}{2} \mu^2 \phi_1^2 + \frac{1}{2} (gv)^2 \left(A_\mu - \frac{1}{gv} \partial_\mu \phi_2 \right)^2 + \cdots . \tag{2.8}$$

Here, by redefinition of the gauge field as follows, a new gauge field with mass gv appears;

$$\tilde{A}_\mu \equiv A_\mu - \frac{1}{gv} \partial_\mu \phi_2 \tag{2.9}$$

Thus, the gauge symmetry is spontaneously broken when the scalar field takes VEV and, accordingly, massless particle (Nambu-Goldstone boson) appears. Furthermore, this particle (ϕ_2) is absorbed as a longitudinal wave component of the redefined gauge field ($\tilde{A}_\mu$), and the gauge field acquires mass. This is called the Higgs mechanism.

2.3 Masses of gauge bosons and fermions

In the SM, when $\mathrm{SU}(2)_L \times \mathrm{U}(1)_Y$ is spontaneously broken to $\mathrm{U}(1)_{EM}$, the Higgs field is generally represented by four real fields and VEV as

$$\phi = \begin{pmatrix} \rho + i\xi \\ \frac{1}{\sqrt{2}}(v + h + i\eta) \end{pmatrix}. \tag{2.10}$$

Here, h, v reapresent the Higgs boson and its VEV, respectively. ρ, ξ and η are Nambu-Goldstone bosons and absorbed into $W^\pm, Z$ bosons by the Higgs mechanism and photon A remains as a massless gauge boson.

The interaction between the Higgs field and gauge bosons is given by the kinetic term $|D_\mu \phi|^2$, which gives the mass terms of $W^\pm, Z$ bosons. The covariate derivative D_μ in the SM is written as

$$D_\mu = \partial_\mu + ig_s \frac{\lambda^a}{2} G^a_\mu + ig \frac{\sigma^a}{2} W^a_\mu + ig_Y Y B_\mu, \tag{2.11}$$

where g_S, g and g_Y are gauge coupling constants for $\mathrm{SU}(3)_C$, $\mathrm{SU}(2)_L$ and $\mathrm{U}(1)_Y$, respectively. λ^a represents Gell-Mann matrices. Here, for convenience, I define the linear combination of the Pauli matrices $\sigma_1, \sigma 2$ as follows;

$$T^\pm \equiv \frac{\sigma^1 \pm i\sigma^2}{2}, \quad T^+ = \begin{pmatrix} 0 & 1 \\ 0 & 0 \end{pmatrix}, T^- = \begin{pmatrix} 0 & 0 \\ 1 & 0 \end{pmatrix}. \tag{2.12}$$

The charged gauge bosons are defined by the following equation;

$$W^\pm \equiv \frac{W^1 \pm iW^2}{\sqrt{2}}. \tag{2.13}$$

Then, one finds

$$\frac{\sigma^a}{2} W^a_\mu = \frac{1}{\sqrt{2}}(T^+ W^+_\mu + T^- W^-_\mu) + \frac{\sigma_3}{2} W^3_\mu. \tag{2.14}$$

Therefore, the mass term of $W^\pm$ boson becomes

$$\mathcal{L}_{\text{mass}} = \left| i\frac{g}{\sqrt{2}} \left(T^+ W^+_\mu + T^- W^-_\mu\right) \begin{pmatrix} 0 \\ \frac{v}{\sqrt{2}} \end{pmatrix} \right|^2 = \frac{g^2 v^2}{4} W^+_\mu W^{\mu -}, \tag{2.15}$$

where only the Higgs VEV is extracted, i.e., $\phi = \begin{pmatrix} 0 \\ \frac{v}{\sqrt{2}} \end{pmatrix}$. Thus, $W^{\pm}$ boson mass is given by

$$m_W = \frac{gv}{2}. \tag{2.16}$$

Next, I discuss Z boson mass. I define the relation between two electrically neutral gauge bosons B, W^3 and photon A, Z boson as follows;

$$\begin{pmatrix} B \\ W^3 \end{pmatrix} = \begin{pmatrix} \cos\theta_W & -\sin\theta_W \\ \sin\theta_W & \cos\theta_W \end{pmatrix} \begin{pmatrix} A \\ Z \end{pmatrix}, \tag{2.17}$$

where θ_W is called Weinberg angle. Then one finds

$$\frac{\sigma_3}{2} W^3_\mu + g_Y Y B_\mu = eQA_\mu + g_Z(I_3 - Q\sin^2\theta_W)Z_\mu, \tag{2.18}$$

where $g_Z \equiv g/\cos\theta_W$. Therefore, the mass term of $Z^{\pm}$ boson becomes

$$\mathcal{L}_{\text{mass}} = \left| i g_Z \left(I_3 - Q\sin^2\theta_W\right) Z_\mu \frac{v}{\sqrt{2}} \right|^2 = \left(\frac{g_Z v}{2\sqrt{2}}\right)^2 Z_\mu Z^\mu. \tag{2.19}$$

Thus, Z boson mass is given by

$$m_Z = \frac{g_Z v}{2}. \tag{2.20}$$

The fermion masses are obtained by the Higgs field taking VEV in the Yukawa interaction (2.3).

$$-\mathcal{L}_{\text{Yukawa}} = f_u \left(\bar{u}_L \;\; \bar{d}_L\right) u_R \begin{pmatrix} \frac{v}{\sqrt{2}} \\ 0 \end{pmatrix} + f_d \left(\bar{u}_L \;\; \bar{d}_L\right) d_R \begin{pmatrix} 0 \\ \frac{v}{\sqrt{2}} \end{pmatrix} + f_e \left(\bar{\nu}_e \;\; \bar{e}_L\right) e_R \begin{pmatrix} 0 \\ \frac{v}{\sqrt{2}} \end{pmatrix} + \text{ h.c..} \tag{2.21}$$

Therefore,

$$m_u = f_u \frac{v}{\sqrt{2}}, \quad m_d = f_u \frac{v}{\sqrt{2}}, \quad m_e = f_e \frac{v}{\sqrt{2}}. \tag{2.22}$$

2.4 CKM matrix

Generalizing the Yukawa interaction of quark fields to account for generations, I can write

$$-\mathcal{L}_{\text{Yukawa}} = f_u^{ij} \bar{u}_L u_R \frac{v}{\sqrt{2}} + f_d^{ij} \bar{d}_L d_R \frac{v}{\sqrt{2}} + \text{ h.c.} \equiv \bar{u}_L M_u^{ij} u_R + \bar{d}_L M_d^{ij} d_R + \text{ h.c.}, \tag{2.23}$$

where i, j are indices that distinguish the quark generations and M_u^{ij}, M_d^{ij} are called mass matrices. The mass matrix is diagonalized by unitary matrices to obtain the mass eigenvalues. Therefore, expressing Eq. (2.23) in terms of the mass eigenstates, we get

$$-\mathcal{L}_{\text{Yukawa}} = = \bar{u}'_L \begin{pmatrix} m_u & 0 & 0 \\ 0 & m_c & 0 \\ 0 & 0 & m_t \end{pmatrix} u'_R + \bar{d}'_L \begin{pmatrix} m_d & 0 & 0 \\ 0 & m_s & 0 \\ 0 & 0 & m_b \end{pmatrix} d'_R + \text{ h.c. }, \tag{2.24}$$

where the prime symbol represents the mass eigenstates and by using unitary matrices, the following relationship holds;

$$u_L = U_L^u u'_L, \quad u_R = U_R^u u'_R, \quad d_L = U_L^d d'_L, \quad d_R = U_R^d d'_R. \tag{2.25}$$

Flavor-Changing interactions of quarks occur via $W^\pm$ bosons;

$$\begin{aligned}\mathcal{L} &= -\frac{g}{\sqrt{2}}\bar{u}_L\gamma^\mu d_L W_\mu^- + \text{h.c.} = -\frac{g}{\sqrt{2}}\bar{u}'_L\gamma^\mu \left(U_L^{u\dagger}U_L^d\right) d'_L W_\mu^- + \text{h.c.} \\ &\equiv -\frac{g}{\sqrt{2}}\bar{u}'_L\gamma^\mu V_{\text{CKM}} d'_L W_\mu^- + \text{h.c.}.\end{aligned} \tag{2.26}$$

V_{CKM} is called the CKM matrix and is a unitary matrix representing the strength of the flavor-changing weak interaction.

The CKM matrix is a 3×3 matrix, but I first discuss why CP symmetry cannot be broken in the two-generation model. Considering an $N \times N$ unitary matrix U, it has N^2 complex matrix elements, so it is described by $2N^2$ real parameters. Here, the condition to be satisfied by the unitary matrix is

$$(UU^\dagger)_{ij} = \delta_{ij}. \tag{2.27}$$

When $i = j$, N real conditionals and when $i \neq j$, ${}_NC_2 \times 2$ real conditionals are given. Therefore, the degree of freedom of an $N \times N$ unitary matrix U is

$$2N^2 - N - \frac{N(N-1)}{2} \times 2 = N^2. \tag{2.28}$$

Next, I consider an $N \times N$ orthogonal matrix. Since an orthogonal matrix can be treated as a unitary matrix restricted to real numbers, its degree of freedom is

$$N^2 - N - \frac{N(N-1)}{2} \times 2 = \frac{N(N-1)}{2}. \tag{2.29}$$

In fact, among the N^2 parameters, there are $N(N-1)/2$ rotation angles, so the number of phases is $N(N+1)/2$. Note here that the quark retains a degree of freedom in the transformation, called re-phasing. By considering the following phase transformation for each quark q;

$$q \to e^{i\phi_q} q, \tag{2.30}$$

the number of degrees of freedom to eliminate the phase is $2N - 1$. Thus, the number of physical CP-violating (CPV) phases is

$$\frac{N(N+1)}{2} - (2N-1) = \frac{(N-1)(N-2)}{2}. \tag{2.31}$$

As can be seen from this, CP symmetry is not broken when the number of generations is 1 or 2, while the symmetry is broken when the number of generations is 3 or more.

The CKM matrix is expressed using the three mixing angles $\theta_{12}, \theta_{23}, \theta_{13}$ and CPV phases δ as follows;

$$V_{\rm CKM} = \begin{pmatrix} c_{12}c_{13} & s_{12}c_{13} & s_{13}e^{-i\delta} \\ -s_{12}c_{23} - c_{12}s_{23}s_{13}e^{i\delta} & c_{12}c_{23} - s_{12}s_{23}s_{13}e^{i\delta} & s_{23}c_{13} \\ s_{12}s_{23} - c_{12}c_{23}s_{13}e^{i\delta} & -c_{12}s_{23} - s_{12}c_{23}s_{13}e^{i\delta} & c_{23}c_{13} \end{pmatrix}, \tag{2.32}$$

where $c_{ij} = \cos\theta_{ij}$ and $s_{ij} = \sin\theta_{ij}$ $(i, j = 1 - 3)$.

Chapter 3

Baryon asymmetry of the universe

According to cosmic inflation, inflation results in a rapid decrease in the energy density of matter, regardless of the initial conditions at the birth of the universe. Therefore, in such a universe, matter and antimatter must have existed in equal amounts. However, in the present universe, there is extremely little antimatter relative to matter. This problem is called the baryon asymmetry of the universe and there is interest in how and at what point this asymmetry occurred. The process that can generate baryon number is called baryogenesis.

Evidence for the baryon asymmetry of the universe (BAU) comes from two observations. One is Big Bang Nucleosynthesis (BBN), which represents the formation of nuclei of elements such as helium and lithium. The physical quantity used to describe the degree of the BAU is the ratio of the baryon number density n_B to the photon density n_γ. η_B calculated from BBN can be expressed as [3]

$$\eta_B^{\rm BBN} = (5.8 - 6.5) \times 10^{-10} \quad (95\%\ \text{CL}). \tag{3.1}$$

n_B is also determined by the Cosmic Microwave Background (CMB) observations [4]. The baryon density parameter observed by Planck $\Omega_B h^2$ is

$$\Omega_B h^2 = 0.0224 \pm 0.0001 \quad (95\%\ \text{CL}). \tag{3.2}$$

Using this, the baryon-to-photon ratios are given as

$$\eta_B^{\rm CMB} = (6.105 \pm 0.055) \times 10^{-10} \quad (95\%\ \text{CL}). \tag{3.3}$$

Therefore, baryogenesis is the process by which such η_B can be generated.

To explain the baryon asymmetry, the following Sakharov conditions must be satisfied [5];

- Baryon number violation
- C and CP symmetry violation

- Out of thermal equilibrium

The reasons why each of these conditions is necessary are described below. First, since the baryon number should have been zero in the early universe, if the interactions of particles are all baryon number conserving, the present baryon number should also be zero. Therefore, the baryon number must be violated. Next, consider C,CP symmetry violation. Suppose reactions occur that produce positive baryon number. Since C symmetry is a symmetry that exchanges particles and antiparticles, the reverse reactions occur at the same probability. In other words, the reverse reactions would produce negative baryon number and the total baryon number would be zero. Therefore, the C symmetry must be broken. When CP symmetry exists, quarks and antiquarks that have opposite chirality are equivalent and the total baryon number cannot be generated. Therefore, CP symmetry violation is also necessary. Furthermore, even if the baryon number is produced by reactions that violate the baryon number, when thermal equilibrium is realized in the early universe, the reverse reactions occur at the same rate, which would wash out the baryon number produced. Therefore, departure from thermal equilibrium is also needed.

The BAU is considered to have been realized after inflation and before BBN. Various hypotheses have been considered to generate baryon numbers during this period such as electroweak baryogenesis (EWBG) [8], leptogenesis [9] and Affleck-Dine baryogenesis [27]. Among these scenarios, EWBG is related to electroweak scale physics, which is expected to be tested by experiment. Experiments that can be used for verification range from colliders to cosmological observations. From this perspective, I focused on EWBG and the following sections describe the mechanism in more detail.

3.1 Sphaleron process

In the standard model (SM), baryon number B and lepton number L are conserved respectively in the classical level, i.e., [28]

$$\begin{aligned} \partial_\mu j_B^\mu &= \partial_\mu \left\{ \frac{1}{3}(\bar{u}_{L,R}\gamma^\mu u_{L,R} + \bar{d}_{L,R}\gamma^\mu d_{L,R}) \right\} = 0, \\ \partial_\mu j_L^\mu &= \partial_\mu \left(\bar{e}_{L,R}\gamma^\mu e_{L,R} + \bar{\nu}_{e,L}\gamma^\mu \nu_{e,L} \right) = 0, \end{aligned} \tag{3.4}$$

where j_B^μ, j_L^μ is the four-vector currents corresponding to these conserved quantities. $u_{L,R}, d_{L,R}, e_{L,R}, \nu_{L,R}$ represent three generations of quarks and leptons. However, these currents do not conserve at the quantum level because the SM is a chiral theory and the electroweak gauge interactions of quarks

and leptons vary with chirality. Therefore one gets

$$\partial_\mu j_B^\mu = \frac{N_g}{32\pi^2} g^2 F^a_{\mu\nu} \tilde{F}^{a,\mu\nu},$$
$$\partial_\mu j_L^\mu = \frac{N_g}{32\pi^2} g^2 F^a_{\mu\nu} \tilde{F}^{a,\mu\nu}, \tag{3.5}$$

where the strength tensor is defined as $\tilde{F}_{\mu\nu} = \frac{1}{2}\epsilon^{\mu\nu\rho\sigma} F_{\rho\sigma}$ and N_g is the number of generations. Note that $B - L$ has no quantum anomaly and is strictly conserved;

$$\partial_\mu (j_B^\mu - j_L^\mu) = 0. \tag{3.6}$$

On the other hand, $B + L$ is not conserved;

$$\partial_\mu (j_B^\mu + j_L^\mu) = \frac{N_g}{16\pi^2} g^2 F^a_{\mu\nu} \tilde{F}^{a,\mu\nu} = \frac{N_g}{16\pi^2} \left[g_2^2 \,\mathrm{Tr}\left(F_{\mu\nu} \tilde{F}^{\mu\nu} \right) - g_1^2 B_{\mu\nu} \tilde{B}^{\mu\nu} \right]. \tag{3.7}$$

It is known that integrating both sides over the entire space-time interval yields

$$\Delta(B + L) = 2 N_g n, \tag{3.8}$$

where n is an integer called topological charge. In this way, $B+L$ varies with the effect of quantum anomaly and the configuration of the gauge field that causes this change is called instanton. When $n = 1$, instanton represents the tunneling effect between degenerate vacua, whose transition rate is

$$\Gamma_{\text{instanton}} \propto e^{-2S_{\text{instanton}}} = e^{-4\pi/\alpha_W} \simeq 10^{-162}. \tag{3.9}$$

where $S_{\text{instanton}}$ is the substitution of the instanton solution for the action of SU(2) gauge fields and $\alpha_W = g_2^2/4\pi$. Thus, $B + L$ is not conserved, but such a transition rate is very small.

Looking a little closer at Eq. (3.8), the infinitely degenerate vacua is characterized by an integer called the Chern-Simons number N_{CS}, which is given by

$$N_{\text{CS}}(t) = \frac{1}{32\pi^2} \int d^3x \epsilon_{ijk} \left[g_2^2 \left(F^a_{ij} A^a_k + \frac{g_2}{3} \epsilon^{abc} A^a_i A^b_j A^c_k \right) - g_1^2 B_{ij} B_k \right]_t. \tag{3.10}$$

Note that in vacua, the Hamiltonian is zero, and "pure gauge" is employed such that the field strength is zero. With pure gauge configuration, one gets

$$A_\mu = \frac{i}{g_2} (\partial_\mu U) U^{-1} \quad B_\mu = \frac{2i}{g_1} (\partial_\mu U_1) U_1^{-1} \quad F^a_{ij} = B_{ij} = 0, \tag{3.11}$$

where U and U_1 are unitary matrices that are elements of SU(2) and U(1), respectively. Therefore, the amount of change in $B + L$ when the Euclideanized time $\tau = -it$ changes from $-\infty$ to ∞ is represented by

$$\Delta(B + L) = N_g \Delta N_{\text{CS}}. \tag{3.12}$$

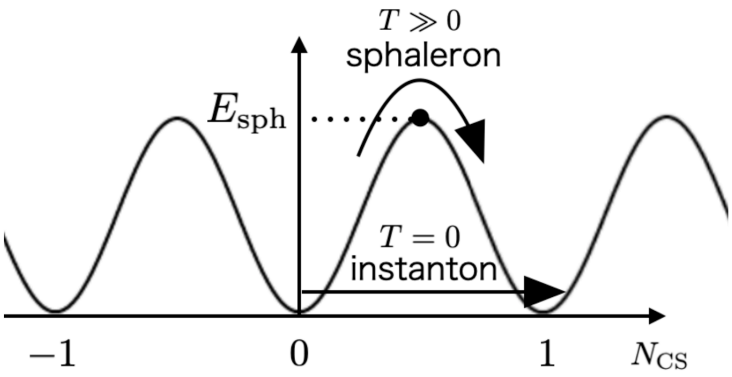

Figure 3.1: Degenerate vacua labeled by Chern-Simons number. Transitions due to instanton occur at zero temperature, but the rate is very small. On the other hand, at high temperature, transitions due to sphaleron processes occur.

Thus, when the gauge field transitions from one classical vacuum to a different vacuum, the fermion number changes due to quantum anomalies.

As mentioned earlier, the transition rate between two vacua by instantons is very small. On the other hand, in the 1980s, F.R.Klinkhammner and N.S.Manton discovered an unstable classical solution in the SU(2) gauge-Higgs system and found that its energy gives the height of the energy barrier between the classical vacua. This classical solution is called a sphaleron, and transitions across the barrier occur at high temperature, such as in the early universe. This classical solution is called sphaleron, and transitions across the barrier occur at high temperature, such as in the early universe. Fig. 3.1 shows the transitions between the degenerate vacua due to instanton and sphaleron.

Note that $\Gamma_{\rm sph}$ in the symmetric phase is different from that in the broken phase. When $\Gamma_{\rm sph}^{\rm sym}/T^3 > H$, the sphaleron process is in chemical equilibrium, where T represents temperature. Here, H is the Hubble parameter and $\Gamma_{\rm sph}^{\rm sym} \sim \alpha_W^5 T^4$. In view of the above, baryogenesis through the sphaleron process must occur at $T \lesssim 10^{12}$ GeV. On the other hand, in order for the baryon number created in the symmetric phase not to be washed out in the broken phase, the sphaleron transition rate must be small around $T \sim 100$ GeV, where the electroweak phase transition (EWPT) occurs (see below for details). Therefore, baryogenesis must be realized at 100 GeV$\lesssim T \lesssim 10^{12}$ GeV.

3.2 Electroweak baryogenesis

From here, I focus on EWBG among the various baryogenesis scenarios. First, I discuss EWBG in the SM. In this case, each of the Sakharov conditions is explained by the following phenomena;

- Baryon number violation : sphaleron process

- C and CP symmetry violation : chiral gauge interaction, CKM matrix
- Out of thermal equilibrium : strong first-order EWPT with expanding bubbles

In practice, however, EWBG is not realized in the SM for two reasons. First, CP symmetry violation introduced by the complex phase of the CKM matrix is too small. The second problem is the inability to achieve a strong first-order EWPT in the SM with the 125 GeV Higgs boson. In order for strong first-order EWPT to occur, there must be an upper limit on the Higgs mass, which is about 70 GeV. This is inconsistent with the Higgs mass observed in the Large Hadron Collider (LHC) experiment. Therefore, since EWBG cannot be realized in the SM, it is necessary to consider new physics beyond the SM that extends the Higgs sector and has new CP-violating (CPV) phases.

3.2.1 Electroweak phase transition

As discussed above, strong first-order EWPT is needed for departure from thermal equilibrium. In this section, I see how first-order EWPT is realized and how the strength of EWPT is evaluated.

In the SM, the electroweak symmetry is spontaneously broken when the Higgs field takes vacuum expectation value (VEV), i.e., $\langle\phi\rangle = v = 246$ GeV. The behavior of the effective potential with temperature is as follows. First, at high temperature, the Higgs field does not take VEV, and the effective potential takes a minimum value at $\langle\phi\rangle = 0$. When a certain temperature is reached, the effective potential takes two degenerate minima. This temperature is called critical temperature T_C and the nonzero Higgs VEV at this time is denoted v_C. As the temperature then decreases, this nonzero Higgs VEV becomes the global minimum.

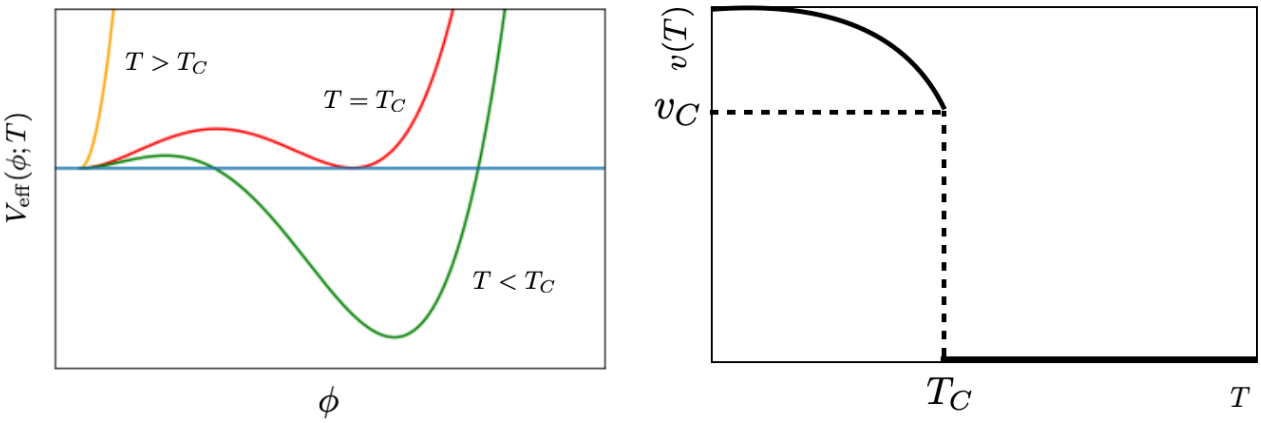

Figure 3.2: The behavior of the effective potential (left panel) and Higgs VEV (right panel) during first-order EWPT.

Such behavior of the effective potential and Higgs VEV is shown in Fig. 3.2. Looking at the right panel, Higgs VEV at T_C changes discontinuously. This discontinuous change from symmetric phase

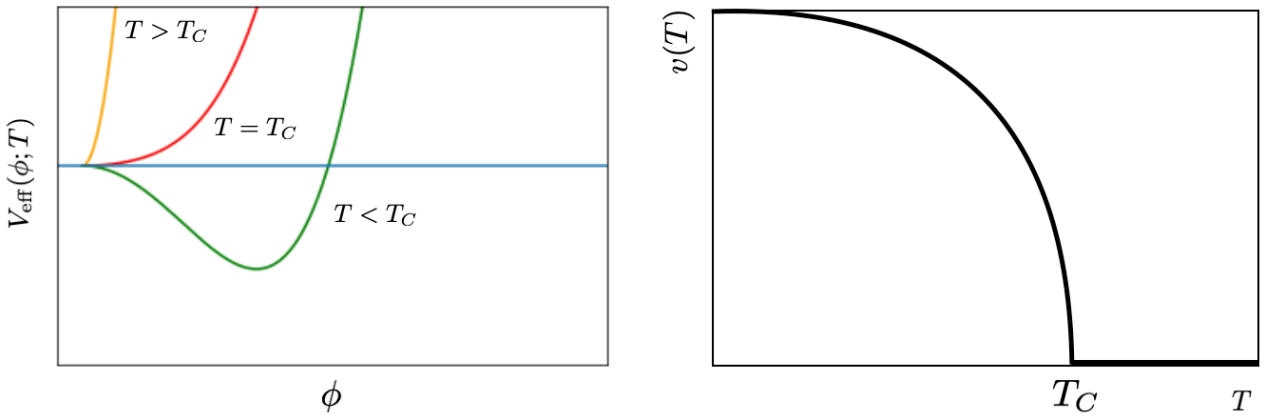

Figure 3.3: The behavior of the effective potential (left panel) and Higgs VEV (right panel) during second-order EWPT.

to broken phase is called first-order EWPT. In addition, the right panel shows that a potential barrier exists between the two degenerate vacua at $T = T_C$. This is what causes tfirst-order EWPT. On the other hand, during second-order EWPT, the behavior of the effective potential and Higgs VEV is as shown in Fig. 3.3. In second-order EWPT, the origin $\phi = 0$ becomes the inflection point when $T = T_C$. Since no potential barrier is created, $v(T)$ varies continuously as shown in the right panel.

Therefore, it is necessary to create a potential barrier at $T = T_C$ for first-order EWPT required for departure from thermal equilibrium. In order to create the barrier, the potential must be lowered once, i.e., negative contributions to the potential are needed. There are two main possible origins of this negative contributions. One is thermal boson-loop, which can occur in both the SM and beyond the SM (BSM). The other is the origin of the tree-level potential, which can occur only in the BSM. Before discussing thermal boson-loop-derived first-order EWPT using the SM, I see how strong first-order EWPT can be defined quantitatively.

In EWBG, the baryon number is generated by an expanding bubble created during first-order EWPT. As shown in Fig. 3.4, outside the bubble is the symmetry phase, in which the Higgs field has no VEV in the high-temperature and inside is the broken phase, in which the Higgs field has VEV in the low-temperature. Considering quarks that pass through or reflect off the bubble wall, left-handed (right-handed) quarks and their antiparticles have different transmissivities and reflectivities. However, right-handed quarks and their antiparticles have the same transmission and reflection rates as left-handed quark antiparticles and left-handed quarks, respectively.

On the bubble wall, the net baryon number n_B becomes zero, i.e.,

$$n_B = n_b^L - n_{\bar{b}}^L + n_b^R - n_{\bar{b}}^R = 0. \tag{3.13}$$

The index b ($\bar{b}$) represents particles (antiparticles) and the index L (R) represents left-handed (right-

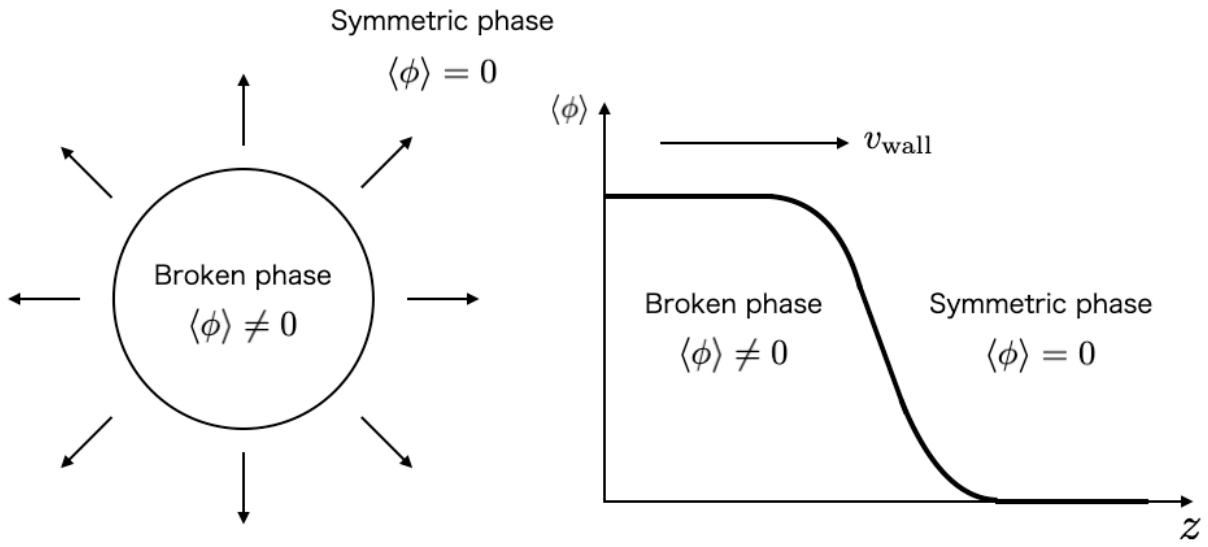

Figure 3.4: Expanding bubble associated EWPT. Outside the bubble is the symmetry phase with no Higgs VEV and inside is the broken phase with nonzero Higgs VEV. z represents the radial axis of the bubble and $v_{\rm wall}$ represents the expansion velocity of the bubble.

handed). On the other hand, in the symmetric phase, since $B + L$ is broken by the sphaleron process, one finds

$$n_B = n_b^L - n_{\bar{b}}^L + n_b^R - n_{\bar{b}}^R \neq 0. \tag{3.14}$$

At this time, the B-changing rate in the symmetric phase is larger than the Hubble constant $\Gamma_B^{\rm sym} > H$. However, in the broken phase, if the same sphaleron process is activated, the opposite reaction to that in the symmetric phase occurs, and the generated baryon number is washed away. Therefore, the B-changing rate in the broken phase should be as follows;

$$\Gamma_B^{\rm bro} < H. \tag{3.15}$$

Although the broken phase is a low-temperature phase, the transition rate by instanton is very small, so the B-changing rate is evaluated using the sphaleron transition rate. The phaleron transition rate in the broken phase is expressed as

$$\Gamma_B^{\rm bro} \propto \Gamma_{\rm sph}^{\rm bro} \propto e^{-E_{\rm sph}/T}. \tag{3.16}$$

Note here that the sphaleron energy is proportional to the Higgs VEV, i.e., $E_{\rm sph} \propto v(T)$. Thus, a large Higgs VEV is required to satisfy the sphaleron decoupling condition (3.15). Specifically, the condition

$$\frac{v_C}{T_C} \gtrsim 1, \tag{3.17}$$

is derived from $\Gamma_B^{\rm bro}(T) < H(T)$. Thus, EWPT must be strong first-order, and Eq. (3.17) is the most important condition for testing EWBG.

EWPT does not actually begin at the critical temperature T_C, but at a slightly lower temperature T_N which is called nucleation temperature. Now let us define T_N and study to what extent this temperature deviates from T_C.

A bubble nucleation rate $\Gamma_N(T)$ per unit time and per unit volume may take the form [29]

$$\Gamma_N(T) \simeq T^4 \left(\frac{S_3(T)}{2\pi T}\right)^{3/2} e^{-S_3(T)/T}, \tag{3.18}$$

where $S_3(T)$ is three-dimensional bounce action describing an energy of a bubble that has a critical radius (critical bubble) at T. The nucleation temperature T_N is defined by a relation

$$\frac{\Gamma_N\left(T_N\right)}{H^3\left(T_N\right)} = H\left(T_N\right) \simeq 1.66\sqrt{g_*(T_N)}\frac{T_N^2}{m_{\rm P}}, \tag{3.19}$$

where $H\left(T_N\right)$ is the Hubble parameter, $m_{\rm P} \simeq 1.22 \times 10^{-19}$ GeV, $g_*(T_N)$ denotes the massless degrees of freedom at T_N, and we take $g_*(T_N) = 108.75$ in the numerical analysis. With $\Gamma_N(T)$ in Eqs. (3.18) and (3.19) is recast into the form

$$\frac{S_3\left(T_N\right)}{T_N} - \frac{3}{2}\ln\left(\frac{S_3\left(T_N\right)}{T_N}\right) = 143.4 - 2\ln\left(\frac{g_*\left(T_N\right)}{100}\right) - 4\ln\left(\frac{T_N}{100\ \text{GeV}}\right), \tag{3.20}$$

which implies that $S_3(T_N)/T_N \lesssim 140$ would be required for the occurrence of EWPT.

From here, I use the Higgs potential of the SM to focus on the thermal boson-loop, which plays an important role in achieving a strong first-order EWPT. First, we consider the 1-loop level effective potential. See App. A for definition and derivation of the effective potential. Note that the following discussion will be based on the basic premise that Eq. (A.67) holds. The Higgs field H with a real background field ϕ_c, Higgs boson h, and Nambu Goldstone bosons χ_a $(a = 1, 2, 3)$ is represented as

$$H = \begin{pmatrix} \chi_1 + i\chi_2 \\ \frac{\phi_c + h + i\chi_3}{\sqrt{2}} \end{pmatrix}. \tag{3.21}$$

The tree-level potential using the background field is

$$V_0(\phi_c) = -\frac{m^2}{2}\phi_c^2 + \frac{\lambda}{4}\phi_c^4. \tag{3.22}$$

The effective potential at the 1-loop level takes the form

$$V_1\left(\phi_c; T\right) = \sum_i n_i \left[V_{\rm CW}\left(\bar{m}_i^2\right) + \frac{T^4}{2\pi^2} I_{B,F}\left(\frac{\bar{m}_i^2}{T^2}\right)\right], \tag{3.23}$$

where $i = h, W, Z$ and t, and degrees of freedom of each particle is respectively given by $n_h = 1, n_W = 6, n_Z = 3$ and $n_t = -12$. $V_{\rm CW}$ is the zero temperature piece, the so-called Coleman-Weinberg potential and is given by

$$V_{\rm CW}(\phi_c) = \sum_i n_i \frac{\bar{m}_i^4}{64\pi^2}\left(\ln\frac{\bar{m}_i^2}{\bar{\mu}^2} - c_i\right). \tag{3.24}$$

$\bar{m}_i$ denote the field dependent masses of the species i and their values in the vacuum represent m_i. Also, μ denotes a renormalization scale and $c_i = 3/2$ for scalars and fermions while $c_i = 5/6$ for gauge bosons. On the other hand, $I_{B,F}$ are the nonzero temperature pieces, which are given by[1]

$$I_{B,F}\left(a^2\right) = \int_0^\infty dx x^2 \ln\left(1 \mp e^{-\sqrt{x^2+a^2}}\right). \tag{3.25}$$

I_B with the upper sign is the thermal function for bosons while I_F with the lower one is that for fermions.

At high temperature, where $\bar{m}_i^2 \ll T^2$, I_B, I_F can be expanded by a^2;

$$I_B\left(a^2\right) = -\frac{\pi^4}{45} + \frac{\pi^2}{12}a^2 - \frac{\pi}{6}\left(a^2\right)^{3/2} - \frac{a^4}{32}\left(\log\frac{a^2}{\alpha_B} - \frac{3}{2}\right) + \mathcal{O}\left(a^6\right), \tag{3.26}$$

$$I_F\left(a^2\right) = \frac{7\pi^4}{360} - \frac{\pi^2}{24}a^2 - \frac{a^4}{32}\left(\log\frac{a^2}{\alpha_F} - \frac{3}{2}\right) + \mathcal{O}\left(a^6\right), \tag{3.27}$$

where $\log\alpha_B = 2\log 4\pi - 2\gamma_E \simeq 3.91$ and $\log\alpha_F = 2\log\pi - 2\gamma_E \simeq 1.14$ with Euler's constant $\gamma_E \simeq 0.577$. Using this high-temperature expansion, the 1-loop effective potential in the SM takes the following form;

$$V_{\rm eff}\left(\phi_c; T\right) = D\left(T^2 - T_0^2\right)\phi_c^2 - ET\phi_c^3 + \frac{\lambda_T}{4}\phi_c^4, \tag{3.28}$$

where

$$D = \frac{2m_W^2 + m_Z^2 + 2m_t^2}{8v^2} \tag{3.29}$$

$$E = \frac{2m_W^3 + m_Z^3}{4\pi v^3} \tag{3.30}$$

$$T_0^2 = \frac{m_h^2 - 8Bv^2}{4D} \tag{3.31}$$

$$B = \frac{3}{64\pi^2 v^4}\left(2m_W^4 + m_Z^4 - 4m_t^4\right) \tag{3.32}$$

$$\lambda_T = \frac{m_h^2}{2v^2}\left[1 - \frac{3}{8\pi^2 v^2 m_h^2}\left\{2m_W^4\log\frac{m_W^2}{\alpha_B T^2} + m_Z^4\log\frac{m_Z^2}{\alpha_B T^2} - 4m_t^4\log\frac{m_t^2}{\alpha_F T^2}\right\}\right]. \tag{3.33}$$

Here, $\log\alpha_B \simeq 3.91$ and $\log\alpha_F \simeq 1.14$. Note that first-order EWPT occurs when $E \neq 0$. In other words, the negative cubic terms of the field make a negative contribution to the potential,

[1] For the derivation of finite temperature effective potential, see App. A.2

thereby creating a potential barrier. This cubic terms arise from the gauge boson-loop at finite temperature.

The critical temperature T_C and the Higgs VEV v_C are expressed as

$$T_C = \frac{T_0}{\sqrt{1 - E^2/(\lambda_{T_C} D)}}, \quad v_C = \frac{2ET_C}{\lambda_{T_C}}. \tag{3.34}$$

From the sphaleron decoupling condition (3.17), one gets

$$\frac{v_C}{T_C} = \frac{2E}{\lambda_{T_C}} \gtrsim 1. \tag{3.35}$$

It can be seen that the condition for a strong first-order EWPT is given by the ratio of the cubic term coefficient to the quartic term one. Since T corrections to quartic coupling are logarithmic, using the approximation $\lambda_{T_C} \simeq \lambda = m_h^2/2v^2$,

$$m_h \lesssim 48 \text{ GeV}. \tag{3.36}$$

This constraint is inconsistent with the Higgs mass observations at the LHC experiments, so we need to consider physics beyond the SM.

3.2.2 Types of effective potential

Effective potential is essential to the evaluation of EWPT, and several methods exist to evaluate it. Here, we employ two gauge-invariant calculation schemes on the scalar potential and two familiar resummation methods in evaluating 1-loop (gauge dependent) effective potential.

First, a gauge-independent method is presented. The quadratic terms of the field extracted from the finite temperature effective potential (the second term in Eq. (3.23)) makes the most dominant contribution to the potential at high temperature and are called the thermal masses. They correspond to the second terms in Eqs. (3.26) and (3.27). The effective potential composed of thermal masses and tree-level potential is called the high-temperature (HT) potential, which is useful for qualitatively evaluating EWPT originating from tree-level structures because it does not include cubic terms of the field derived from thermal boson-loop. In Chapter 5, the specific HT potential of the complex singlet extension of the SM (CxSM) is given. In Eq. (3.28), B, D and T_0^2 are gauge-independent quantities. Thus, note that both thermal masses and high temperature (HT) potential are gauge-invariant.

Even though the HT potential is of much use to discuss EWPT qualitatively, validity of the high-temperature expansions of $I_{B,F}$ would not been guaranteed as temperature goes down. Furthermore, 1-loop contributions at $T = 0$ would not be negligible for quantitative study. In order to incorporate higher-order corrections in a gauge-invariant way, we employ Patal-Ramsey-Musolf

(PRM) scheme [30]. In this formalism, T_C and the corresponding VEVs at T_C are determined separately, and the higher-order corrections can be taken into account based on the Nielsen-Fukuda-Kugo (NFK) identity [31, 32]

$$\frac{\partial V_{\rm eff}(\varphi,\xi)}{\partial \xi} = -C(\varphi,\xi)\frac{\partial V_{\rm eff}(\varphi,\xi)}{\partial \varphi}, \tag{3.37}$$

where $C(\varphi,\xi)$ denotes some functional that is calculable order by order in perturbation theory. One can obtain the NFK identity to given order by expanding each term in the both sides in powers of $\hbar$. In the PRM scheme, T_C is determined using some degeneracy condition [30] (Specific examples are given in chapter 5) and after that v_C is determined by use of $V^{\rm HT}$. It is noticed in Refs. [33, 34] that the $\overline{\mu}$ dependence is rather large in the $\mathcal{O}(\hbar)$ calculation, and $\mathcal{O}(\hbar^2)$ contributions are necessary for the quantitative study. In the current investigation, however, we confine ourselves to the $\mathcal{O}(\hbar)$ calculation as a first step toward more complete analysis, and set $\overline{\mu} = m_t = 172.76$ GeV as a reference point.

We have so far discussed two methods (HT and PRM) to evaluate the effective potential in the gauge invariant manner. For comparisons, we also evaluate strength of EWPT using the 1-loop

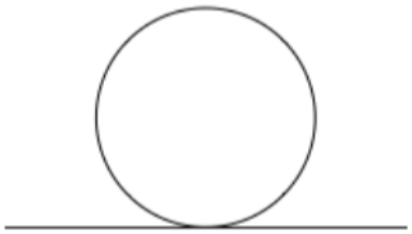

Figure 3.5: 1-loop self-energy diagram.

potential (3.23) with the so-called daisy resummations. Using the ϕ^4 theory, I confirm that the perturbation theory is broken by higher-order diagram effects. The Lagrangian is given by

$$\mathcal{L} = \frac{1}{2}\partial_\mu\phi_c\partial^\mu\phi_c - V_0(\phi_c), \quad V_0(\phi_c) = -\frac{m^2}{2}\phi_c^2 + \frac{\lambda}{4!}\phi_c^4, \tag{3.38}$$

where $\lambda > 0$ and $m^2 > 0$. The mass term receives temperature-dependent contributions and can be expressed as

$$\bar{M}^2 = \overline{m}^2 + \Sigma_{\phi_c}(\phi_c;T), \tag{3.39}$$

where $\Sigma_{\phi_c}(\phi_c;T)$ is a temperature-dependent self-energy and the overline corresponds field dependent masses (See App. B for derivation of field dependent masses.). At 1-loop order, one obtains

$$\bar{M}^2 = \overline{m}^2 + \frac{\lambda}{2}I(\overline{m}^2), \tag{3.40}$$

where

$$\frac{\lambda}{2} I\left(\overline{m}^2\right) = \frac{\lambda}{2} \int \sum_k \frac{1}{K^2 + \overline{m}^2} \underset{T>0}{\longrightarrow} \frac{\lambda}{2} \frac{I_B'\left(a^2\right)}{\pi^2} = \frac{\lambda}{2} \left[\frac{T^2}{12} - \frac{T\overline{m}}{4\pi} + \cdots\right]. \tag{3.41}$$

$I(m^2)$ is in Eqs. (3.26) and (3.27) and $I_B'\left(a^2\right) = \partial I_B\left(a^2\right)/\partial a^2$. Eq. (3.40) can be represented by a diagram as in Fig. 3.5.

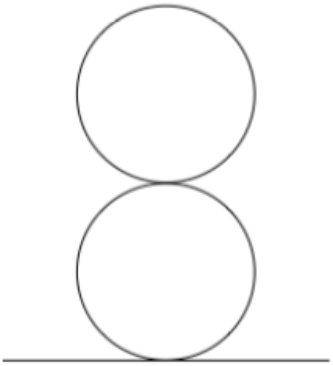

Figure 3.6: The figure-8 diagram.

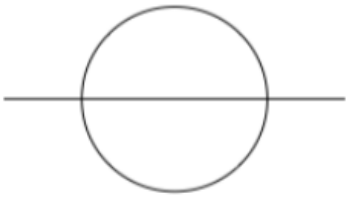

Figure 3.7: Sunset diagram.

There are two possible two-loop diagrams: the figure-8 diagram (Fig. 3.6) and the sunset diagram (Fig. 3.7). Dropping the coefficients, the self energies from the two diagrams in the high-T limit are given as follows:

$$\text{(the figure-8)} \approx \lambda T^2 \left(\frac{\lambda T}{\overline{m}}\right), \tag{3.42}$$

$$\text{(sunset)} \approx \lambda^2 T^2 \ln \frac{\overline{m}}{T}. \tag{3.43}$$

Therefore, the figure-8 diagram is more dominant at high temperature.

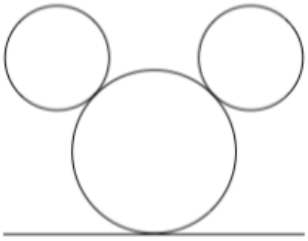

Figure 3.8: Mouse diagram.

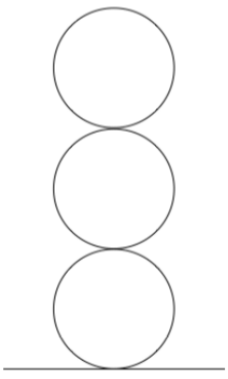

Figure 3.9: Cactus diagram.

The figure-8 diagrams with one more loop added are called the mouse diagram (Fig. 3.8) and the cactus diagram (Fig. 3.9). Dropping the coefficients, the self energies from the two diagrams in the high temperature limit are given as follows:

$$(\text{mouse}) \approx \left(\lambda T^2\right)^2 \left(\frac{\lambda T}{\overline{m}^3}\right), \tag{3.44}$$

$$(\text{cactus}) \approx \lambda T^2 \left(\frac{\lambda T}{\overline{m}}\right)^2, \tag{3.45}$$

Therefore, the mouse diagram is more dominant at high temperature.

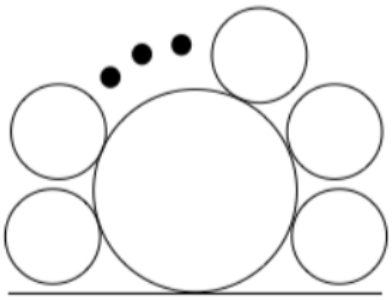

Figure 3.10: daisy diagram.

The figure-8 diagram plus n loops is called a daisy diagram and is shown in Fig. 3.10. The self-energy of this diagram is

$$(\text{daisy}) \sim \frac{\lambda^2 T^3}{\overline{m}} \left(\frac{\lambda T^2}{\overline{m}^2}\right)^{n-2}. \tag{3.46}$$

For the perturbation expansion to take place, $\lambda T^2/\overline{m}^2 < 1$ must be obtained. Therefore, it is necessary to review the effective potential in the high temperature region where temperature T is considerably larger than the mass $\overline{m}$. This treatment is also known as resummation.

As commonly done in the literature, Parwani [35] and Arnold-Espinosa (AE) [36] schemes are used for the resummation. For the former, we replace $\overline{m}_i^2$ appearing in I_B and I_F with thermally corrected field dependent masses (See App. B for details.) denoted as $\bar{M}_i^2$. For the latter, on the other hand, we add

$$V_{\text{daisy}}(\varphi, \varphi_S; T) = \sum_{\substack{i=h_{1,2},\chi \\ W_L, Z_L, \gamma_L}} -n_i \frac{T}{12\pi} \left[\left(\bar{M}_i^2\right)^{3/2} - \left(\overline{m}_i^2\right)^{3/2}\right] \tag{3.47}$$

to the 1-loop effective potential $V_0 + V_1$, where $\overline{m}_i^2$ in V_1 remain intact. W_L, Z_L, and γ_L are the longitudinal parts of the gauge fields whose degrees of freedom are $n_{W_L}/2 = n_{Z_L} = n_{\gamma_L} = 1$, respectively. In principle, the transverse parts of the gauge fields also receive non-perturbative thermal corrections. Since the first-order EWPT is predominantly induced by the tree-level potential in our case, such a correction has little effect on v_C/T_C.

3.2.3 WKB approximation for top transport scenario

WKB approximation and semiclassical force

This section describes the WKB method for calculating charge accumulation in top transport scenario [37, 38, 39, 40, 41, 42]. The WKB approximation is valid when the bubble wall thickness L_w separating broken and symmetric phases is larger than the typical interaction length. At temperature T, the interaction length is expressed as $l \simeq 1/T$, so $L_w > 1/T$ is required, which is called a thick wall regime.

When a bubble expands in space, the Higgs VEV is not uniform. Outside the bubble, the Higgs takes no VEV and has a finite value inside the bubble. Around the wall, the Higgs VEV varies continuously (See Fig. 3.4). SM particles acquire mass by the Higgs mechanism as mentioned in Sec. 2.3. In other words, local VEV means that the mass of the particle changes spatially. The interaction of particles with the wall of an expanding bubble can be described using the local mass of particles.

To consider the process by which the baryon number is generated, we begin with the Dirac equation for fermion ψ with local mass. I solve the Dirac equation using the WKB method and derive the forces acting on particles from bubble wall. I consider a system in which the wall is stationary at $z = 0$. The positive direction of z corresponds to the symmetric phase, and the negative direction to the broken phase. From here on, the calculations will be based primarily on ref. [41].

The mass term of fermion ψ is expressed as

$$\begin{aligned}\mathcal{L}_{\psi\text{-mass}} &= -M(z)\bar{\psi}P_R\psi + M(z)^*\bar{\psi}P_L\psi \\ &= \mathrm{Re}[M(z)]\bar{\psi}\psi + i\,\mathrm{Im}[M(z)]\bar{\psi}\gamma_5\psi. \end{aligned} \tag{3.48}$$

$M(z)$ is local mass of fermion ψ. Since $\bar{\psi}\gamma_5\psi$ is CP-odd, the imaginary part of local mass is the source of CPV.

The Dirac equation for ψ is

$$\left(i\gamma^\mu\partial_\mu - M(z)P_R - M^*(z)P_L\right)\psi = 0. \tag{3.49}$$

A wave function with positive energy can be written like

$$\psi_s = e^{-i\omega}\begin{pmatrix} L_s \\ R_s \end{pmatrix} \otimes \chi_s, \quad \sigma^3\chi_s = s\chi_s, \tag{3.50}$$

where s is spin along z-axis and ω is energy of ψ. Substituting ψ_s into the Dirac equation, then one finds

$$(\omega - is\partial_z)\,L_s = MR_s, \tag{3.51}$$

$$(\omega + is\partial_z)\,R_s = M^*L_s. \tag{3.52}$$

Putting these two equations together, I derive the equation for L_s;

$$\left((\omega + is\partial_z) \frac{1}{M} (\omega - is\partial_z) - M^* \right) L_s = 0. \tag{3.53}$$

Assuming that the mass term varies sufficiently slowly along the z direction, under the WKB approximation, the solution L_s is

$$L_s = \omega e^{i\int^z p_{cz}(z')\mathrm{d}z'} \tag{3.54}$$

Here p_{cz} is the canonical momentum along the z direction, not a physical momentum. Substituting this equation into the equation for L_s (3.53) derives the formula for ω and p_{cz};

$$\begin{cases} \omega^2 - m^2 - p_{cz}^2 + (s\omega + p_{cz})\,\theta' - \frac{m'}{m}\frac{\omega'}{\omega} + \frac{\omega''}{\omega} = 0, \\ 2p_{cz}\omega' + p_{cz}'\omega - \frac{m'}{m}(s\omega + p_{cz})\,\omega - \theta'\omega' = 0, \end{cases} \tag{3.55}$$

where prime means to derivative with respect to z. In addition,

$$m(z) = |M(z)|, \quad \theta(z) = \arg M(z). \tag{3.56}$$

The energy of ψ is given by

$$\omega = \sqrt{(p_{cz} - \alpha_{\mathrm{CP}})^2 + m^2} \mp \frac{s\theta'}{2}. \tag{3.57}$$

The sign of the third term of the right-hand side of Eq. (3.57) is + (-) for the particle (antiparticle). This is the dispersion relation for frame where ψ has no momentum in the direction parallel to the bubble wall; if ψ has momentum in the x, y direction, the dispersion relation is

$$\omega = \omega_0 \mp \frac{s\theta'}{2}\frac{\omega_{0z}}{\omega_0}, \tag{3.58}$$

where ω_0 and ω_{0z} is defined as

$$\omega_0 = \sqrt{p_x^2 + p_x^2 + (p_{cz} - \alpha_{\mathrm{CP}})^2 + m^2}, \tag{3.59}$$

$$\omega_{0z} = \sqrt{(p_{cz} - \alpha_{\mathrm{CP}})^2 + m^2}, \tag{3.60}$$

where p_x and p_y are physical momenta. The physical momentum in the z direction p_z is calculated as $p_z = \omega v_{gz}$, where $v_{gz} = \partial\omega/\partial p_{cz}$ is a group velocity.

Using only physical quantities, the energy and group velocity of particles can be expressed as

$$E = E_0 \mp \Delta E, \tag{3.61}$$

$$v_{gz} = \frac{p_z}{E_0}\left(1 \pm \frac{s\theta'}{2}\frac{m^2}{E_0^2 E_{0z}}\right), \tag{3.62}$$

where

$$\Delta E = -\frac{sm^2\theta'}{2E_0E_{0z}}, \tag{3.63}$$

$$E_0 = \sqrt{p_x^2 + p_y^2 + p_z^2 + m^2}, \tag{3.64}$$

$$E_{0z} = \sqrt{p_z^2 + m^2}. \tag{3.65}$$

From this, we derive the force acting on particles. The force in the z direction F_z is

$$F_z = \frac{\mathrm{d}p_z}{\mathrm{d}t} = \omega\dot{v}_{gz} = \omega\left\{v_{gz}\left(\frac{\partial v_{gz}}{\partial z}\right)_{p_{cz}} - \left(\frac{\partial\omega}{\partial z}\right)_{p_{cz}}\left(\frac{\partial v_{gz}}{\partial p_{cz}}\right)_z\right\}, \tag{3.66}$$

where the energy conservation $\dot{\omega} = 0$ and canonical equations of motion were used. Substituting the equations of ω (3.58) and v_{gz} (3.62), I obtain

$$F_z = -\frac{(m^2)'}{2E_0} \pm \frac{s\,(m^2\theta')'}{2E_0E_{0z}} \mp \frac{sm^2\theta'\,(m^2)'}{4E_0^3E_{0z}}. \tag{3.67}$$

This equation shows that the forces exerted on particles and antiparticles are different: the CP-violating force is

$$F_z^{CP} = \pm\frac{s\,(m^2\theta')'}{2E_0E_{0z}} \mp \frac{sm^2\theta'\,(m^2)'}{4E_0^3E_{0z}}. \tag{3.68}$$

This force causes a difference between the motion of the particle and the motion of the antiparticle.

Charge transport equation

The CP-violating force due to local mass causes a difference between the motion of the particles and that of the antiparticles. This difference generates a current of hypercharge, which accumulates around the bubble wall. This accumulation is described by the chemical potential of the particles. Using the Boltzmann equation and the CP-violating force, I derive the transport equation for the chemical potential. Solving this yields the distribution of current accumulation.

In interactions where the mean free path $\Gamma^{-1}$is less than the wall thickness L_w, the fermion state represented by Eq. (3.54) is assumed to behave like a particle with momentum (p_x, p_y, p_z). In other words, I now assume that momentum is conserved in the scattering process between WKB states and behaves as a free particle at infinity. Under these assumptions, the thermal equilibrium distribution function in the wall frame of the WKB state takes the form

$$f_i^{eq}(x, \boldsymbol{p}) = \frac{1}{e^{\beta\gamma_w(E_{i0} \pm \Delta E_i + v_w p_{iz})} + 1}, \tag{3.69}$$

where $\beta = 1/T$ and $\gamma_w = 1/\sqrt{1 - v_w^2}$. v_w is the wall velocity in a frame where all plasma is stationary. Each particle is labeled with i. The deviation from the thermal equilibrium caused by the passage of wall can be expressed as

$$f_i(x, \boldsymbol{p}) = \frac{1}{e^{\beta[\gamma_w(E_{i0} \pm \Delta E_i + v_w p_{iz}) - \mu_i(x)]} + 1} + \delta f_i(x). \tag{3.70}$$

The chemical potentials $\mu_i(x)$ represent local deviations from equilibrium. The perturbations $\delta f_i(x)$ model a departure from kinetic equilibrium and allow the particles to move in response to the force exerted by the bubble wall. This does not contribute to the particle density and is therefore referred to as $\int \mathrm{d}^3 p \delta f_i = 0$.

Particles and antiparticles can be identified by equations like

$$\mu_i = \mu_{\mathrm{i,1e}} + \mu_{\mathrm{i,2o}} + \mu_{\mathrm{i,2e}}, \quad \delta f_i = \delta f_{\mathrm{i,1e}} + \delta f_{\mathrm{i,2o}} + \delta f_{\mathrm{i,2e}}, \tag{3.71}$$

Indices 1 and 2 denote the order of perturbation, and the CP-even (odd) part is denoted with indices e (o). Also, the CP-violating effect appears only at the second order of perturbation. I expand the distribution function to second order in derivatives as

$$\begin{aligned} f_i \simeq & f_{i0,v_w} + f'_{i0,v_w} \left(\gamma_w \Delta E_i - \mu_{\mathrm{i,1e}} - \mu_{\mathrm{i,20}} - \mu_{\mathrm{i,2e}}\right) \\ & + \frac{1}{2} f''_{i0,v_w} \left(\gamma_w^2 (\Delta E)^2 - 2\gamma_w \Delta E \mu_{\mathrm{i,1e}}^2\right) + \delta f_{\mathrm{i,1e}} + \delta f_{\mathrm{i,20}} + \delta f_{\mathrm{i,2e}}, \end{aligned} \tag{3.72}$$

where f_{i0,v_w} is the unperturbed distribution function expressed as

$$f_{i0,v_w} = \frac{1}{e^{\beta\gamma_w (E_{i0} + v_w p_{iz})} + 1}, \tag{3.73}$$

and $f'_{i0,v_w} = (d/dE_{i0})\, f_{i0,v_w}$.

The Boltzmann equation for $f_i(x, \boldsymbol{p})$ is given by

$$L\left[f_i\right] \equiv \left(v_{gz} \frac{\partial}{\partial z} + F_{iz} \frac{\partial}{\partial p_{iz}}\right) = C\left[f_i\right], \tag{3.74}$$

where $L\left[f_i\right]$ and $C\left[f_i\right]$ are the Liouville operator and the collision term for f_i, respectively. Substituting the expansion equation for f_i (3.72), the force in the z direction (3.67), and the group velocity (3.62) into the Boltzmann equation (3.74) and subtracting the particle and antiparticle results in the CP-odd part;

$$\begin{aligned} \mathbf{L}[f]|_{\mathrm{CP-\ odd}} =& \frac{1}{2}\left(L\left[f_i\right] - L\left[\overline{f_i}\right]\right) \\ =& v_\omega f_{i0,v_w} \left(\frac{s\left(m^2\theta'\right)'}{2E_{i0}E_{i0z}} - \frac{s\theta' m^2 \left(m^2\right)'}{4E_{i0}^3 E_{i0z}}\right) + v_\omega f''_{i0,v_\omega} \left(\frac{s\theta' m^2 \left(m^2\right)'}{4E_{i0}^2 E_{i0z}}\right) \\ & + \frac{\left(m^2\right)' \mu_{io}}{2E_{i0}\gamma_w} v_w f''_{i0,v_\omega} - \frac{p_{iz}\mu'_{io}}{E_{i0}\gamma_w} f'_{i0,v_w} + \frac{p_{iz}}{E_{i0}} \left(\partial_z \delta f_{io}\right) \\ & - \frac{\left(m^2\right)'}{2E_{i0}} \left(\partial_{p_{iz}} \delta f_{io}\right). \end{aligned} \tag{3.75}$$

Assuming that the wall velocity is slow enough, expand f_{i0,v_w} to the linear order of v_w;

$$f_{i0,v_\omega} = f_{i0} + v_\omega p_{iz} f'_{i0} + \mathcal{O}\left(v_w^2\right), \tag{3.76}$$

where f_{i0} are defined as

$$f_{i0} = \frac{1}{e^{\beta E_{i0}} + 1}. \tag{3.77}$$

Integrating Eq. (3.75) by three-momentum $\mathbf{p}_i$ yields

$$\frac{1}{2}\left\langle L\left[f_i\right] - L\left[\bar{f}_i\right]\right\rangle = \mu_{io} v_w \left(m^2\right)' \left\langle \frac{1}{2E_{i0}} f''_{i0} \right\rangle - \mu'_{io} v_\omega \left\langle \frac{p_{iz}^2}{E_{i0}} f''_{i0} \right\rangle \tag{3.78}$$

$$+ \left\langle \frac{p_{iz}}{E_{i0}} \left(\partial_z \delta f_{io}\right) \right\rangle - \left(m^2\right)' \left\langle \frac{1}{2E_{i0}} \left(\partial_{p_{iz}} \delta f_{io}\right) \right\rangle, \tag{3.79}$$

where $\langle \cdots \rangle$ is defined as

$$\langle X \rangle = \frac{\int \mathrm{d}^3 p_i X}{\int \mathrm{d}^3 p_i f'_{i0} \left(m_i = 0\right)}. \tag{3.80}$$

Eq. (3.79) includes δf_{io}, and the plasma velocity u_i can be expressed as

$$u_i = \left\langle \frac{p_{iz}}{E_{i0}} \delta f_{io} \right\rangle. \tag{3.81}$$

Finally, we obtain the following result;

$$\frac{1}{2}\left\langle L\left[f_i\right] - L\left[\bar{f}_i\right]\right\rangle = v_w K_{i1} \mu'_{io} + v_w \left(m^2\right)' K_{i2} \mu_{io} + u'_i, \tag{3.82}$$

where

$$K_{i1} = \left\langle f'_{i0} \right\rangle, \quad K_{i2} = \left\langle \frac{1}{2E_{i0}} f''_{i0} \right\rangle. \tag{3.83}$$

In the same way, we also obtain the following relation;

$$\frac{1}{2}\left\langle \frac{p_{iz}}{E_{i0}} \left(L\left[f_{i0}\right] - L\left[\bar{f}_{i0}\right]\right) \right\rangle = \lambda_i v_w \left(m^2 \theta'\right)' K_{i8} - \lambda_i v_w \theta' m^2 \left(m^2\right)' K_{i9} \tag{3.84}$$

$$- \mu'_{io} K_{i4} + v_w \left(m^2\right)' u_i \tilde{K}_{i6} - v_w u'_i, \tag{3.85}$$

where λ_i is the helicity of the particle i and

$$K_{i4} = \left\langle \frac{p_{iz}^2}{E_{i0}^2} f'_{i0} \right\rangle, \quad \tilde{K}_{i6} = \left[\frac{1}{2E_{i0}} f'_{i0} \right], \quad K_{i8} = \left\langle \frac{|p_{iz}|\, f'_{i0}}{2E_{i0}^2 E_{i0z}} \right\rangle, \tag{3.86}$$

$$K_{i9} = \left\langle \frac{|p_{iz}|}{4E_{i0}^3 E_{i0z}} \left(\frac{f'_{i0}}{E_{i0}} - f''_{i0} \right) \right\rangle. \tag{3.87}$$

$[\cdots]$ is defined as

$$[X] = \frac{\int \mathrm{d}^3 p_i X}{\int \mathrm{d}^3 p_i f_{i0,v_w}}. \tag{3.88}$$

The results obtained from the integration of the collision terms are

$$\frac{1}{2}\left\langle C\left[f_i\right]-C\left[\overline{f_i}\right]\right\rangle=\beta K_{i0}\sum_{\sigma\in\text{ inela}}\Gamma_\sigma\sum_j s_j^\sigma\mu_{jo}, \tag{3.89}$$

$$\frac{1}{2}\left\langle\frac{p_{iz}}{E_{i0}}\left(C\left[f_i\right]-C\left[\overline{f_i}\right]\right)\right\rangle=\Gamma_{\text{tot}}\,u_i+v_w\beta K_{i0}\sum_{\sigma\in\text{ inela}}\Gamma_\sigma\sum_j s_j^\sigma\mu_{jo}, \tag{3.90}$$

where Γ_σ is the thermally averaged reaction rate for an inelastic scattering σ and $\Gamma_{\text{tot}}=\sum_{\sigma\in\text{ inela}}\Gamma_\sigma$. The symbol s_j^σ is defined as $s_j^\sigma=1$ ($s_j^\sigma=-1$) for j in the initial (final) state of the process σ. The normalization factor is expressed as

$$K_{i0}=-\left\langle f_{i0}\right\rangle/T_n, \tag{3.91}$$

where T_n is the bubble nucleation temperature. Substituting Eqs. (3.82),(3.85),(3.89) and (3.90) into the Boltzmann equation results in the following transport equation;

$$\begin{cases} u_i'+v_wK_{i1}\mu_{io}'+v_w\left(m^2\right)'K_{i2}\mu_{io}-\beta K_{i0}\sum_{\sigma\in\text{ inela}}\Gamma_\sigma\sum_j s_j^\sigma\mu_{j0}=0 \\ -\mu_{io}'K_{i4}-v_wu_i'+v_w\left(m^2\right)'\tilde{K}_{i6}u_i+\Gamma_{\text{tot}}\,u_i+v_w\beta K_{i0}\sum_{\sigma\in\text{inela}}\Gamma_\sigma\sum_j s_j^\sigma\mu_{jo}=S_i. \end{cases} \tag{3.92}$$

CK-shceme

The derivation of the transport equation presented in the previous section is based on ref [41]. This is a good approximation when v_w is small, but ref. [42] points out that it is controversial when the wall velocity is large. Cline and Kainulainen give a transport equation at high wall velocities, which takes the form

$$\begin{cases} -D_{i,1}\mu_i'+u_i'+\gamma_wv_w\left(m_i^2\right)'Q_{i,1}\mu_i-K_{i,0}\bar{\Gamma}_i=S_{i,1} \\ -D_{i,2}\mu_i'-v_wu_i'+\gamma_wv_w\left(m_i^2\right)'Q_{i,2}\mu_i+\left(m_i^2\right)'\bar{R}_iu_i+\Gamma_{i,\text{ tot}}\,u_i+v_wK_{i,0}\bar{\Gamma}_i=S_{i,2}, \end{cases} \tag{3.93}$$

where $\gamma=1/\sqrt{1-v_w^2}$. The functions $K,D,Q,\bar{R}$ can be expressed as

$$\begin{aligned} &K_{i,0}=-\langle f_{i0}\rangle/T_n,\ D_{i,1}=-v_wK_{i,1}=\left\langle f_{i0}'\right\rangle,\ Q_{i,1}\simeq K_{i,2}=\left\langle\frac{1}{2E_{i0}}f_{i0}''\right\rangle \\ &D_{i,2}\simeq K_{4,i}=\left\langle\frac{p_{iz}^2}{E_{i0}^2}f_{i0}'\right\rangle,\quad Q_{i,2}=\left\langle\frac{p_{iz}}{2E_{i0}^2}f_{i0}''\right\rangle,\quad \bar{R}_i=\left[\frac{1}{2E_{i0}p_{iz}}\right]\neq\tilde{K}_{i,6}. \end{aligned} \tag{3.94}$$

Plasma velocity in the wall frame u_i is defined by $u_i=\int d^3p_i\left(p_{iz}/E_{i0}\right)\delta f_{i0}$. The inelastic reaction

rates for each particle is defined as [42]

$$\begin{aligned}
\bar{\Gamma}_t =& \Gamma_{SS}\left(\left(1+9D_{t,0}\right)\mu_t + 10\mu_b + \left(1-9D_{t,0}\right)\mu_{t^c}\right) \\
&+ \Gamma_W\left(\mu_t - \mu_b\right) + \Gamma_y\left(\mu_t + \mu_{t^c} + \mu_h\right) + 2\Gamma_m\left(\mu_t + \mu_{t^c}\right), \qquad (3.95)\\
\bar{\Gamma}_b =& \Gamma_{SS}\left(\left(1+9D_{t,0}\right)\mu_t + 10\mu_b + \left(1+9D_{t,0}\right)\mu_{t^c}\right) \\
&+ \Gamma_W\left(\mu_b - \mu_t\right) + \Gamma_y\left(\mu_b + \mu_{t^c} + \mu_h\right), \qquad (3.96)\\
\bar{\Gamma}_{t^c} =& \Gamma_{SS}\left(\left(1+9D_{t,0}\right)\mu_t + 10\mu_b + \left(1-9D_{t,0}\right)\mu_{t^c}\right) \\
&+ 2\Gamma_m\left(\mu_{t^c} + \mu_t\right) + \Gamma_y\left(2\mu_{t^c} + \mu_t + \mu_b + 2\mu_h\right), \qquad (3.97)\\
\bar{\Gamma}_h =& \frac{3}{4}\Gamma_y\left(2\mu_h + \mu_t + \mu_b + 2\mu_{t^c}\right) + \Gamma_h\mu_h, \qquad (3.98)
\end{aligned}$$

where

$$\begin{aligned}
&D_{i,0} = K_{i,1} = \langle f'_{i0}\rangle, \quad \Gamma_{ss} = 4.9\times10^{-4}T, \quad \Gamma_y = 4.2\times10^{-3}T,\\
&\Gamma_m = m_t^2(z)/(63T), \quad \Gamma_h = m_W^2(z)/(50T), \quad \Gamma_W = \Gamma_{h,\mathrm{tot}}. \qquad (3.99)
\end{aligned}$$

Furthermore the total interaction rate can be expressed by the diffusion constant, $\Gamma_{i,\mathrm{tot}} = D_{i,2}/D_{i,0}D_i$, where the quark diffusion constant is given by $D_q = 6/T$ and the Higgs diffusion constant by $D_h = 20/T$.

From Eq. (3.93), the transport equations for the chemical potentials of the top quarks μ_t and μ_{t^c} , left-handed bottom quarks μ_b, Higgs doublets μ_h, and the relevant plasma velocities u_i $(i = t, b, t^c, h)$ are represented as

$$\begin{aligned}
S_{t,1} &= -D_{t,1}\mu'_t + u'_t + \gamma_w v_w\left(m_t^2\right)' Q_{t,1}\mu_t - K_{t,0}\bar{\Gamma}_t, \qquad (3.100)\\
0 &= -D_{b,1}\mu'_b + u'_b - K_{b,0}\bar{\Gamma}_b, \qquad (3.101)\\
S_{t,1} &= -D_{t,1}\mu'_{t^c} + u'_{t^c} + \gamma_w v_w\left(m_t^2\right)' Q_{t,1}\mu_{t^c} - K_{t,0}\bar{\Gamma}_{t^c}, \qquad (3.102)\\
0 &= -D_{h,1}\mu'_h + u'_h - K_{h,0}\bar{\Gamma}_h, \qquad (3.103)\\
S_{t,2} &= -D_{t,2}\mu'_t - v_w u'_t + \gamma_w v_w\left(m_t^2\right)' Q_{t,2}\mu_t + \left(m_t^2\right)'\bar{R}_t u_t + \Gamma_{t,\ \mathrm{tot}}\ u_t + v_w K_{t,0}\bar{\Gamma}_t, \qquad (3.104)\\
0 &= -D_{b,2}\mu'_b - v_w u'_b + \Gamma_{b,\ \mathrm{tot}}\ u_b + v_w K_{b,0}\bar{\Gamma}_b, \qquad (3.105)\\
S_{t,2} &= -D_{t,2}\mu'_{t^c} - v_w u'_{t^c} + \gamma_w v_w\left(m_t^2\right)' Q_{t,2}\mu_{t^c} + \left(m_t^2\right)'\bar{R}_t u_{t^c} + \Gamma_{t,\ \mathrm{tot}}\ u_{t^c} + v_w K_{t,0}\bar{\Gamma}_{t^c}, \qquad (3.106)\\
0 &= -D_{h,2}\mu'_h - v_w u'_h + \Gamma_{h,\ \mathrm{tot}}\ u_h + v_w K_{h,0}\bar{\Gamma}_h, \qquad (3.107)
\end{aligned}$$

with the source terms for the top quark,

$$S_{t,l} = -\gamma_w v_w\left(m_t^2\theta'_{CP}\right)' Q^8_{t,l} + \gamma_w v_w m_t^2\theta'_{CP}\left(m_t^2\right)' Q^9_{t,l} \quad (l = 1, 2), \qquad (3.108)$$

where

$$\begin{aligned}
Q^8_{i,l} &\equiv \left\langle \frac{s_{\mathrm{p}} p_z^{\ell-1}}{2E^l E_z} f'_{0w}\right\rangle \qquad (3.109)\\
Q^9_{i,l} &\equiv \left\langle \frac{s_{\mathrm{p}} p_z^{\ell-1}}{4E^{l+1} E_z}\left(\frac{1}{E} f'_{0w} - \gamma_w f''_{0w}\right)\right\rangle. \qquad (3.110)
\end{aligned}$$

For large velocities, there is no hierarchy between $S_{t,1}$ and $S_{t,2}$ and one must include both sources [42]. One would take the masses of the bottom quarks and Higgs as massless because their impacts are small [41].

First derivatives of Eqs. (3.104)-(3.107) with respect to z are respectively given by

$$\mu_t'' = \frac{\partial_z S_{t,2} + \gamma_w v_w (m_t^2)' Q_{t,2} \mu_t' + (m_t^2)' \bar{R}_t u_t' + \Gamma_{t,\mathrm{tot}} u_t' + v_w K_{t,0} \bar{\Gamma}_t'}{D_{t,2}} \tag{3.111}$$

$$\mu_b'' = \frac{\Gamma_{b,\mathrm{tot}} u_b' + v_w K_{b,0} \bar{\Gamma}_b'}{D_{b,2}} \tag{3.112}$$

$$\mu_{t^c}'' = \frac{\partial_z S_{t,2} + \gamma_w v_w (m_t^2)' Q_{t,2} \mu_{t^c}' + (m_t^2)' \bar{R}_t u_{t^c}' + \Gamma_{t,\mathrm{tot}} u_{t^c}' + v_w K_{t,0} \bar{\Gamma}_{t^c}'}{D_{t,2}} \tag{3.113}$$

$$\mu_h'' = \frac{\Gamma_{h,\mathrm{tot}} u_h' + v_w K_{h,0} \bar{\Gamma}_h'}{D_{h,2}}. \tag{3.114}$$

Substituting u_i' obtained from Eqs. (3.100)-(3.103) and $\partial_z S_{t,l}$ obtained from Eq. (3.108) into the above equations, I obtain the second order differential equation for μ_i.

Solving the above transport equations yields distributions of chemical potentials. The boundary conditions are as follows [43];

$$\mu_i(z)|_{z\to\mathrm{inf}} = 0, \quad \mu_i'(z)|_{z\to\mathrm{inf}} = 0, \tag{3.115}$$

where infinity z corresponds to the symmetric phase. Using these distributions, the baryon number density normalized by the entropy density is evaluated as

$$\eta_B = \frac{405\Gamma_{\mathrm{sph}}^{\mathrm{sym}}}{4\pi^2 \gamma_w v_w g_* T} \int_0^\infty dz \mu_{B_L} f_{\mathrm{sph}} \exp\left(-\frac{45\Gamma_{\mathrm{sph}}^{\mathrm{sym}} z}{4\gamma_w v_w}\right), \tag{3.116}$$

where

$$\mu_{B_L} = \frac{1}{2}\left(1 + 4D_{0t}\right)\mu_t + \frac{1}{2}\left(1 + 4D_{0b}\right)\mu_b - 2D_{0t}\mu_{t^c}. \tag{3.117}$$

The effective degrees of freedom of the plasma given by $g_* = 106.75$ in the SM. $\Gamma_{\mathrm{sph}}^{\mathrm{sym}}$ is evaluated as $\Gamma_{\mathrm{sph}}^{\mathrm{sym}} = 1.0 \times 10^{-6} T$. The function f_{sph} describes the suppression of the sphaleron rate outside the bubble caused by the nonzero VEVs. This suppression factor is given by

$$f_{\mathrm{sph}}(z) = \min\left[1, \frac{2.4T}{\Gamma_{\mathrm{sph}}^{\mathrm{sym}}} \exp\left(\frac{-40\phi(z)}{T}\right)\right]. \tag{3.118}$$

Chapter 4

Dark matter

Dark matter (DM) is a general term for matter whose existence has been suggested astronomically but which cannot be observed optically. In 1933, Fritz Zwicky postulated DM to explain the missing mass in the orbital velocity of galaxies in a galaxy cluster. Other observations also suggest the existence of DM, such as galaxy rotation speeds and gravitational lensing effects.

From these observations, DM is expected to have the properties of (1) being massive, (2) having no electric charge, and (3) being stable (at least for a lifetime longer than the age of the universe). Furthermore, Planck's observations of the Cosmic microwave background (CMB) indicate that DM, dark energy, and ordinary matter account for 26.8%, 68.3%, and 4.9%, respectively, of the average energy density of the current universe. The observations are in agreement with DM values predicted from simulations of the large-scale structure of the universe.

There are many possible candidates for DM, which can be divided into hot DM with relativistic motion and cold DM with non-relativistic motion. Predictions of cold DM paradigm are generally consistent with observations of cosmological large-scale structure. One of the most promising candidates for cold DM is the weakly interacting massive particle (WIMP). They are known to be in good agreement with data on the thermal abundance of DM obtained from observations of the CMB (the so-called "WIMP miracle"). In the following subsections, I discuss the thermal abundance of DM, as well as the direct detection experiments that strongly constraint the scattering of DM and nucleons.

4.1 Relic abundance of DM

The density parameter of DM Ω_χ in the current universe (time: $t = t_0$, temperature: $T = T_0$), according to the CMB observations, is given by [4]

$$\Omega_\chi (t_0)\, h^2 \equiv \frac{\rho_\chi (T_0)\, h^2}{3 M_{\rm Pl}^2 H_0^2} = 0.120 \pm 0.001, \tag{4.1}$$

where ρ_χ is DM mass density and is given by $\rho_\chi(t) = m_\chi n_\chi(t)$ with particle number density n_χ. $M_{\rm Pl}$ is Planck mass, H_0 is the Hubble parameter that determines the current rate of cosmic expansion, and h is Planck constant.

In a scenario using a freeze out mechanism, DM is stable and does not decay, but DM pair annihilates into lighter arbitrary particles $A(\bar{A})$, i.e.,

$$\chi + \bar{\chi} \leftrightarrow A + \bar{A}. \tag{4.2}$$

In the early universe, it was in thermal equilibrium where rightward and leftward reactions of the process (4.2) were constantly taking place, but when the temperature decreases due to cosmic expansion and the universe is not in thermal equilibrium, DM can no longer be produced from light particles, and only rightward reactions of the process (4.2) occur. Then, at some point, the reaction rate of annihilation becomes less than the expansion rate of the universe. In other words, the annihilation process freezes out. The observed relic density is the frozen remnant.

The time variation of the particle number density $n(t)$ follows Boltzmann's equation as follows;

$$\frac{dn(t)}{dt} + 3\frac{\dot{a}(t)}{a(t)}n(t) = -\left\langle \sigma v_{\rm rel} \right\rangle \left(n(t)^2 - n_{\rm eq}(t)^2 \right), \tag{4.3}$$

where $\langle \sigma v_{\rm rel} \rangle$ is defined as the thermal average of the DM annihilation cross section. This equation includes the contribution of the universe expansion. To solve Eq. (4.3), I introduce dimensionless quantities;

$$Y = \frac{n(t)}{s}, \quad z = \frac{m_\chi}{T}, \tag{4.4}$$

where s is the entropy density, and Y is a constant as long as the baryon number is conserved since both $n(t)$ and s are proportional to a^{-3} (a: scale factor). Furthermore, the Hubble constant $H(t)$ and mass density $\rho_{\rm rad}$ are known to behave as follows;

$$H(t) \sim \frac{1}{2t}, \quad \rho_{\rm rad} \sim \frac{\pi^2}{30} g^* T^4, \tag{4.5}$$

where g^* is the sum of degrees of freedom of particles in thermal equilibrium. From the Friedman equation for the radiation-dominant period, the relationship between $H(t)$ and $\rho_{\rm rad}$ is obtained;

$$H(t)^2 \sim \frac{\rho_r(t)}{3M_{\rm Pl}^2} = \frac{1}{3M_{\rm Pl}^2}\frac{\pi^2}{30} g^* T^4 = \left(\frac{\pi\sqrt{g^*}}{\sqrt{90}} \frac{T^2}{M_{\rm Pl}} \right)^2. \tag{4.6}$$

Thus, Boltzmann equation of (4.3) can be rewritten as

$$\frac{dY}{dz} = -\sqrt{\frac{8\pi^2 g^*}{45}} m_\chi M_{\rm Pl} \left\langle \sigma v_{\rm rel} \right\rangle \times \frac{1}{z^2}(Y^2 - Y_{\rm eq}^2). \tag{4.7}$$

From Eq. (4.7), the relationship shown in Fig. 4.1 is derived. When z is small, Y decreases with

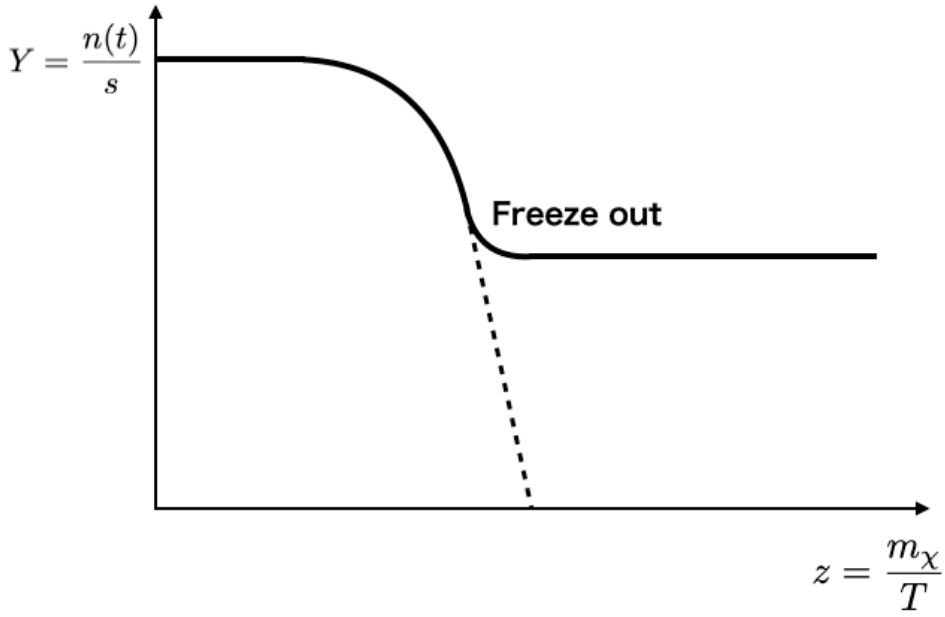

Figure 4.1: The schematic illustration of the freeze out mechanism.

increasing z due to the contribution of $Y_{\rm eq}$, but at some point $Y_{\rm eq}$ contribution cease to work and the annihilation reaction freezes out. After the decoupling, Y is kept at approximately the same value. Specifically, the following equation is obtained;

$$Y(z \to \infty) \simeq \frac{1}{m_\chi M_{\rm pl} \langle \sigma v_{\rm rel} \rangle}. \tag{4.8}$$

Therefore, the current DM density parameter is

$$\begin{aligned} \Omega_\chi(t_0) &= \frac{\rho_\chi(t_0)}{\rho_{\rm crit}(t_0)} = \frac{m_\chi n(t_0)}{\rho_{\rm crit}(t_0)} = m_\chi \left(\frac{n(t_0)}{s(t_0)} \right) \frac{1}{(\rho_{\rm crit}(t_0)/s(t_0))} \\ &\simeq \frac{1}{M_{\rm pl} \langle \sigma v_{\rm rel} \rangle} \frac{1}{1.8 \times 10^{-9}\ {\rm GeV}} \simeq 0.2 \left(\frac{1\ {\rm pb}}{\langle \sigma v_{\rm rel} \rangle} \right). \end{aligned} \tag{4.9}$$

Comparison with the current observed value (4.1) shows that $\langle \sigma v_{\rm rel} \rangle \sim 1$ pb. Here, the annihilation cross section of WIMP DM is approximately given by the ratio of the weak coupling and the weak scale mass;

$$\langle \sigma v_{\rm rel} \rangle \simeq \frac{\mathcal{O}(\alpha^2)}{m_\chi^2} \simeq \frac{\mathcal{O}(10^{-4})}{\mathcal{O}(10^2)} \sim 1\ {\rm pb}. \tag{4.10}$$

Thus, considering the freeze out mechanism with WIMP DM naturally explains the currently observed DM relic density. This is so-called "WIMP miracle".

4.2 DM direct detection experiment

The search for DM has been attempted in a variety of ways, yet no sign of DM has been detected. Among them, I focus on direct detection experiments. In this experiment, a huge tank filled with

liquid xenon is buried underground, and DM from space collides with xenon nuclei. Then the signals emitted when the nuclei recoil are detected. In particular, the recent LUX-ZEPLIN (LZ) experiment provides strict upper bounds on the spin-independent cross section between DM and nucleons [18]. Therefore, an important task in the construction of DM models is to suppress the scattering of DM and nucleons.

Here, I assume that DM χ is a gauge singlet scalar particle and derive spin-independent scattering cross sections between DM and nucleons [44, 45]. Nucleons consist of quarks q and gluons g. I first consider the scattering $\chi q \to \chi q$. The effective Lagrangian is written as

$$\mathcal{L}_{\text{eff}} = C^q \chi^2 m_q \bar{q} q, \tag{4.11}$$

where C^q is the Wilson coefficient. The expectation values of the scalar bilinear operators of quarks are parametrized as

$$\langle N \left| m_q \bar{q} q \right| N \rangle / m_N = f_q^N, \tag{4.12}$$

which are called mass fractions. $|N\rangle$ $(N = p, n)$ is the nucleon states at rest and m_N is nucleon mass. The mass fractions of nucleons f_N are given by using the mass fractions of each quark as follows;

$$\begin{aligned} f_N/m_N &= C^q \left\{ \sum_{q=u,d,s} f_q^N + 3 \times \frac{2}{27} \left(1 - \sum_{q=u,d,s} f_q^N \right) \right\} \\ &= \begin{cases} C^q \times 0.286333 & (N = p), \\ C^q \times 0.288820 & (N = n). \end{cases} \end{aligned} \tag{4.13}$$

The effective Lagrangian describing the interaction between scalar DM χ and nucleons N is written as

$$\mathcal{L}_{\text{eff}} = f'_N m_\chi \chi^2 \bar{N} N. \tag{4.14}$$

The spin-independent cross section σ_{SI}^N can be expressed as

$$\sigma_{\text{SI}}^N = \frac{1}{\pi} \left(\frac{m_\chi m_N}{m_\chi + m_N} \right)^2 \left| f'_N \right|^2, \tag{4.15}$$

where f_N is dimension $[\text{M}]^{-1}$ and f'_N is dimension $[\text{M}]^{-2}$, so replace $f'_N m_\chi$ with f_N. Then the cross section is

$$\sigma_{\text{SI}}^N = \frac{1}{\pi} \left(\frac{m_\chi m_N}{m_\chi + m_N} \right)^2 \frac{1}{m_\chi^2} \left| f_N \right|^2. \tag{4.16}$$

Therefore, the scattering cross section between DM and nuclei (mass number: A, proton number: Z) can be written as

$$\sigma_{\rm SI} = \frac{1}{\pi}\left(\frac{m_\chi m_T}{m_\chi + m_T}\right)^2 \frac{1}{m_\chi^2}\left|Zf_p + (A-Z)f_n\right|^2, \tag{4.17}$$

where m_T represents mass of the target nucleus.

Defining the converted masses of DM-proton and DM-nucleus as μ_p and μ_N, respectively, the scattering cross sections between DM and the protons in xenon nucleus ($A = 131,\ Z = 54$) $\sigma^p_{\rm SI}$ are obtained as follows;

$$\begin{aligned}
\sigma^p_{\rm SI} &= \sigma_{\rm SI}\frac{1}{A^2}\frac{\mu_p}{\mu_N} \\
&= \frac{1}{\pi}\left(\frac{m_p}{m_\chi + m_p}\right)^2 \frac{1}{A^2}\left|Zf_p + (A-Z)f_n\right|^2 \\
&\simeq \frac{1}{\pi}\left(\frac{C^q m_p^2}{m_\chi + m_p}\right)^2 \frac{1}{A^2}\left|Z\times 0.286333 + (A-Z)\times 0.288820\right|^2\Big|_{A=131,Z=54} \\
&\simeq 1.026\times 10^{-35}\ {\rm cm}^2 \cdot \left(\frac{C^q m_p^2}{0.1}\right)^2 \left(\frac{100\ {\rm GeV}}{m_\chi + m_p}\right)^2,
\end{aligned} \tag{4.18}$$

where C^q is the coefficient of $\chi\chi\bar{q}q$ as in Eq. (4.11) and is a model-dependent quantity. Thus, by calculating C^q for each model, we can compare the cross section with the bounds of direct detection experiments.

Chapter 5

CP-conserving CxSM

5.1 The Model

The CxSM is the extension of the SM by adding the complex SU(2) gauge singlet scalar field [19]. In our study, we adopt the following scalar potential:

$$V_0(H,S) = \frac{m^2}{2}H^\dagger H + \frac{\lambda}{4}\left(H^\dagger H\right)^2 + \frac{\delta_2}{2}H^\dagger H|S|^2 + \frac{b_2}{2}|S|^2 + \frac{d_2}{4}|S|^4 + \left(a_1 S + \frac{b_1}{4}S^2 + \text{H.c.}\right), \tag{5.1}$$

where a global U(1) symmetry for S is softly broken by both a_1 and b_1. In the following, all the couplings in (5.1) are assumed to be real. When the linear term of S is absent, there is a Z_2 symmetry ($S \to -S$) in the scalar potential. Once the singlet S develops the VEV, the Z_2 symmetry is spontaneously broken, and it causes the domain-wall problem [46]. Therefore, we add the linear term of S to the scalar potential (5.1) because it explicitly breaks the Z_2 symmetry, and the model does not suffer from the domain-wall problem. Though various U(1) breaking terms are present in the potential, not all of them must address the strong first-order EWPT and viable DM, so we adopt a minimal set of operators that close under renormalization.

We parametrize the scalar fields as

$$H = \begin{pmatrix} G^+ \\ \frac{1}{\sqrt{2}}\left(v + h + iG^0\right) \end{pmatrix}, \tag{5.2}$$

$$S = \frac{1}{\sqrt{2}}\left(v_S + s + i\chi\right), \tag{5.3}$$

where v ($\simeq 246$ GeV) and v_S represent the VEVs of H and S, respectively. The Nambu-Goldstone bosons G^+ and G^0 are eaten by W and Z bosons, respectively, after the electroweak symmetry breaking. Since we assumed no complex parameters in (5.1), the scalar potential is invariant under CP-transformation ($S \to S^*$). Therefore, the real and imaginary parts of S do not mix, and the stability of χ is guaranteed, making it a pseudoscalar DM candidate.

First derivatives of V_0 for h and s are respectively given by

$$\frac{1}{v}\left\langle \frac{\partial V_0}{\partial h} \right\rangle = \frac{m^2}{2} + \frac{\lambda}{4}v^2 + \frac{\delta_2}{4}v_S^2 = 0, \tag{5.4}$$

$$\frac{1}{v_S}\left\langle \frac{\partial V_0}{\partial s} \right\rangle = \frac{b_2}{2} + \frac{\delta_2}{4}v^2 + \frac{d_2}{4}v_S^2 + \frac{\sqrt{2}a_1}{v_S} + \frac{b_1}{2} = 0, \tag{5.5}$$

where $\langle \cdots \rangle$ is defined as taking all fluctuation fields to zero. Note that Nonzero v_S is enforced by $a_1 \neq 0$.

The mass matrix of the CP-even states (h, s) is expressed as

$$\mathcal{M}_S^2 = \begin{pmatrix} \lambda v^2/2 & \delta_2 v v_S/2 \\ \delta_2 v v_S/2 & \Lambda^2 \end{pmatrix}, \quad \Lambda^2 \equiv \frac{d_2}{2}v_S^2 - \sqrt{2}\frac{a_1}{v_S}. \tag{5.6}$$

The mass matrix (6.7) is diagonalized by an orthogonal matrix $O(\alpha)$ as

$$O(\alpha)^\top \mathcal{M}_S^2 O(\alpha) = \begin{pmatrix} m_{h_1}^2 & 0 \\ 0 & m_{h_2}^2 \end{pmatrix}, \quad O(\alpha) = \begin{pmatrix} \cos\alpha & -\sin\alpha \\ \sin\alpha & \cos\alpha \end{pmatrix}, \tag{5.7}$$

where α is a mixing angle. The mass eigenstates $(h_1,\ h_2)$ are given through the mixing angle α as

$$\begin{pmatrix} h \\ s \end{pmatrix} = \begin{pmatrix} \cos\alpha & \sin\alpha \\ -\sin\alpha & \cos\alpha \end{pmatrix} \begin{pmatrix} h_1 \\ h_2 \end{pmatrix}. \tag{5.8}$$

We emphasize that $\alpha \to 0$ corresponds to the SM-like limit ($h_1 \to h,\ h_2 \to s$). The mass eigenvalues are expressed as

$$m_{h_1,h_2}^2 = \frac{1}{2}\left(\frac{\lambda}{2}v^2 + \Lambda^2 \mp \frac{\frac{\lambda}{2}v^2 - \Lambda^2}{\cos 2\alpha} \right) \tag{5.9}$$

$$= \frac{1}{2}\left(\frac{\lambda}{2}v^2 + \Lambda^2 \mp \sqrt{\left(\frac{\lambda}{2}v^2 - \Lambda^2\right)^2 + 4\left(\frac{\delta_2}{2}v v_S\right)^2} \right), \tag{5.10}$$

$$\cos 2\alpha = \frac{\frac{\lambda}{2}v^2 - \Lambda^2}{m_{h_1}^2 - m_{h_2}^2} \tag{5.11}$$

We fix h_1 as the Higgs boson observed in the LHC experiments, i.e., $m_{h_1} = 125$ GeV. The mass of CP-odd state χ is given by the soft breaking terms a_1 and b_1 as

$$\begin{aligned} m_\chi^2 &= \frac{b_2}{2} - \frac{b_1}{2} + \frac{\delta_2}{4}v^2 + \frac{d_2}{4}v_S^2 \\ &= -\frac{\sqrt{2}a_1}{v_S} - b_1, \end{aligned} \tag{5.12}$$

where the tadpole condition (5.5) is used in the second equality.

For later convenience, we mention the relationship between input and output parameters. In the following study, we adopt $\{v, v_S, m_{h_1}, m_{h_2}, \alpha, m_\chi, a_1\}$ as inputs while the Lagrangian parameters

$\{m^2, b_2, \lambda, d_2, \delta_2, b_1\}$ can be expressed as functions of inputs. Among the Lagrangian parameters, m^2 and b_2 are eliminated from the tadpole conditions (5.4) and (5.5),

$$m^2 = -\frac{\lambda}{2}v^2 - \frac{\delta_2}{2}v_S^2 \tag{5.13}$$

$$b_2 = -\frac{\delta_2}{2}v^2 - \frac{d_2}{2}v_S^2 - \sqrt{2}\frac{a_1}{v_S} - b_1. \tag{5.14}$$

The remaining four parameters in the six Lagrangian parameters are given as

$$\lambda = \frac{2}{v^2}\left(m_{h_1}^2 \cos^2\alpha + m_{h_2}^2 \sin^2\alpha\right), \tag{5.15}$$

$$\delta_2 = \frac{1}{vv_S}\left(m_{h_1}^2 - m_{h_2}^2\right)\sin 2\alpha, \tag{5.16}$$

$$d_2 = 2\left(\frac{m_{h_1}}{v_S}\right)^2 \sin^2\alpha + 2\left(\frac{m_{h_2}}{v_S}\right)^2 \cos^2\alpha + 2\sqrt{2}\frac{a_1}{v_S^3}, \tag{5.17}$$

$$b_1 = -m_\chi^2 - \frac{\sqrt{2}}{v_S}a_1. \tag{5.18}$$

Theoretical constraints on the quartic couplings in the scalar potential are summarized as follows. (See App. C for details.) A requirement on the scalar potential that is bounded from below is given by[1]

$$\lambda > 0, \quad d_2 > 0. \tag{5.19}$$

The couplings λ and d_2 should also satisfy the following conditions from the perturbative unitarity [46]

$$\lambda < \frac{16\pi}{3}, \quad d_2 < \frac{16\pi}{3}. \tag{5.20}$$

In addition, by requiring that eigenvalues of the mass matrix (5.10) be positive, the stability condition of the tree-level potential follows as [19]

$$\frac{2\lambda\Lambda^2}{v_s^2} = \lambda\left(d_2 - \frac{2\sqrt{2}a_1}{v_S^3}\right) > \delta_2^2. \tag{5.21}$$

5.2 Degenerate scalar scenario

As mentioned in Chapter. 4, the presence of DM offers direct proof of physics beyond the Standard Model and one of the primary candidates for DM is WIMP. Despite cosmological observations affirming the existence of DM, no signal of WIMP has been detected either in high-energy accelerator experiments like the LHC experiment or in the direct detection experiments. Notably, the recent

[1]For $\delta_2 < 0$, $\lambda d_2 > \delta_2^2$ is also needed. In this paper, we assume that δ_2 is positive.

LUX-ZEPLIN (LZ) experiment imposes stringent upper limits on the spin-independent cross section between DM and nucleons. Consequently, a pivotal objective in the formulation of DM models is to suppress the scattering of DM and nucleons.

Several ideas have been proposed to suppress the scattering of DM and nucleons. In general, we consider the possibility that (1) the DM mass is very large or very small, and (2) the interaction between DM and SM particles is very weak. Here, however, we consider other possibilities. That is, both the DM mass and the strength of the interaction with the SM particles are in the experimentally reachable range, but some built-in mechanism suppresses the scattering of the DM and nucleons. In particular, the so-called pseudo Nambu-Goldstone (pNG) DM model, including our model, is known to have this mechanism. This model extends the SM by introducing a complex singlet scalar, denoted as S. The imaginary part of S gives rise to a pNG boson due to the breaking of global U(1) symmetry in the scalar potential. The CP symmetry of the scalar potential prevents the pNG boson from decaying, leading it to serve as DM. Conversely, the real component of S undergoes mixing with the SM Higgs boson, resulting in two CP-even mass eigenstates, namely h_1 and h_2. Consequently, the DM-quark scattering can be described by two scattering amplitudes, one mediated by h_1 and the other by h_2. In ref. [47], the global U(1) symmetry of the scalar potential is softly broken by a dimension-2 operator S^2. Then, the scattering amplitudes mediated by h_1 and h_2 cancel independently of the DM coupling and mass in the limit of zero momentum transfer.

On the other hand, in our model, we introduce a linear term of S in the scalar potential to avoid the model suffering from the so-called domain-wall problem due to the discrete symmetry of S ($S \to -S$). As a result, the suppression mechanism in ref. [47] no longer works, and the cancellation of the amplitudes could be achieved when masses of two mediator particles (h_1, h_2) degenerate. This is called the degenerate scalar scenario and we will discuss this in detail in the next subsection.

5.2.1 Cancellation mechanism of DM-quark scattering

In this section, we study a suppression mechanism of the scattering process of the DM χ off a quark q, $\chi q \to \chi q$, described by the Feynman diagram in Fig. 5.1. The interaction Lagrangian of DM χ to the CP-even scalars h_1, h_2 is given by

$$\begin{aligned}\mathcal{L}_S &= C_{\chi\chi h_1}\chi^2 h_1 + C_{\chi\chi h_2}\chi^2 h_2 \\ &= -\frac{m_{h_1}^2 + \frac{\sqrt{2}a_1}{v_S}}{2v_S}\sin\alpha\ \chi^2 h_1 + \frac{m_{h_2}^2 + \frac{\sqrt{2}a_1}{v_S}}{2v_S}\cos\alpha\ \chi^2 h_2,\end{aligned} \tag{5.22}$$

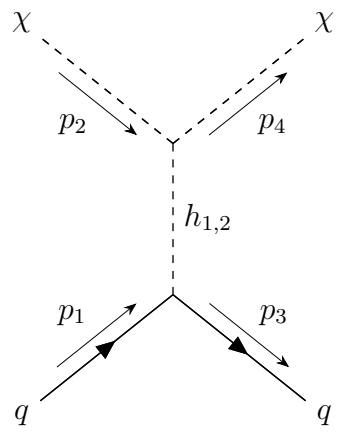

Figure 5.1: Feynman diagram of the scattering process $\chi q \to \chi q$ mediated by h_1 and h_2.

while that of a quark q to h_1 or h_2 is given by

$$\begin{aligned}\mathcal{L}_Y &= C_{qqh_1}\bar{q}qh_1 + C_{qqh_2}\bar{q}qh_2 \\ &= \frac{m_q}{v}\bar{q}q\left(h_1\cos\alpha - h_2\sin\alpha\right), \end{aligned} \tag{5.23}$$

where m_q denotes a mass of the quark q. Then, the scattering amplitude $\mathcal{M}$ is given by a sum of two amplitudes $\mathcal{M}_1$ and $\mathcal{M}_2$ mediated by h_1 and h_2, respectively;

$$i\mathcal{M} = i(\mathcal{M}_1 + \mathcal{M}_2), \tag{5.24}$$

$$\begin{aligned} i\mathcal{M}_1 &= -i2C_{\chi\chi h_1}C_{qqh_1}\frac{1}{t-m_{h_1}^2}\bar{u}(p_3)u(p_1) \\ &= -i\frac{m_q}{vv_S}\frac{m_{h_1}^2 + \frac{\sqrt{2}a_1}{v_S}}{t-m_{h_1}^2}\sin\alpha\cos\alpha\bar{u}\left(p_3\right)u\left(p_1\right), \end{aligned} \tag{5.25}$$

$$\begin{aligned} i\mathcal{M}_2 &= -i2C_{\chi\chi h_2}C_{qqh_2}\frac{1}{t-m_{h_2}^2}\bar{u}(p_3)u(p_1) \\ &= -i\frac{m_q}{vv_S}\frac{m_{h_2}^2 + \frac{\sqrt{2}a_1}{v_S}}{t-m_{h_2}^2}\sin\alpha\cos\alpha\bar{u}\left(p_3\right)u\left(p_1\right), \end{aligned} \tag{5.26}$$

where $t \equiv (p_1 - p_3)^2$ is a momentum transfer and $u(p)$ ($\bar{u}(p)$) represents an incoming (outgoing) quark spinor with a momentum p. A factor 2 in the r.h.s of the first lines of (5.25) and (5.26) is a symmetry factor for the $\chi\chi h_i$ vertex. When $t \ll m_{h_1}, m_{h_2}$, the sum of the two amplitudes can be expressed as

$$\begin{aligned} i\mathcal{M} = i\frac{m_f}{vv_S}\bar{u}\left(p_3\right)u\left(p_1\right)\sin\alpha\cos\alpha \\ \times\left\{\left(-\frac{m_{h_1}^2}{t-m_{h_1}^2}+\frac{m_{h_2}^2}{t-m_{h_2}^2}\right)+\frac{\sqrt{2}a_1}{v_S}\left(-\frac{1}{t-m_{h_1}^2}+\frac{1}{t-m_{h_2}^2}\right)\right\}. \end{aligned} \tag{5.27}$$

The first term in the brackets on the right-hand side becomes insignificant as t approaches zero, as demonstrated in ref. [47]. Conversely, the second term disappears when the masses of two scalar

particles are degenerate ($m_{h_1} = m_{h_2}$). This cancellation by a degenerate scalar comes from the orthogonality of the mixing matrix, $O_{ik}O_{jk} = \delta_{ij}$. Consequently, in this model, to satisfy the results of the direct detection experiment, the mass of the CP-even scalar h_2 must be close to the mass of h_1 ($m_{h_1} = 125$ GeV). It should also be emphasized that if the masses of the two Higgs bosons are degenerate, this scattering can be suppressed without setting the momentum transfer to zero.

5.2.2 Collider signals

The possibility for investigating the degenerate scalar scenario through collider experiments has been studied by ref. [46]. The authors noted that while the mass difference $|m_{h_1} - m_{h_2}| \lesssim 3$ GeV has not been conclusively ruled out by LHC experiments [48]. The mixing angle α is generally constrained by the presence of an extra Higgs boson, but when the Higgs boson masses are degenerate, α is not limited and can take the maximum value $\alpha = \pi/4$. Furthermore, ref. [46] indicates that the narrow range of $|m_{h_1} - m_{h_2}| \lesssim 1$ GeV may soon be tested with an e^+e^- linear collider.

We mention that the degenerate scalar scenario is compatible with the Higgs search experiments at the LHC. As shown in Eq. (5.23), the couplings between h_1 (h_2) and the SM particles are those with the SM Higgs boson multiplied by $\cos\alpha$ ($-\sin\alpha$). For example, decay rates from h_1 and h_2 to the SM particle X is expressed as follows;

$$\Gamma_{h_1\to XX} = \cos^2\alpha\ \Gamma^{\rm SM}_{h\to XX}(m_{h_1}), \tag{5.28}$$

$$\Gamma_{h_2\to XX} = \sin^2\alpha\ \Gamma^{\rm SM}_{h\to XX}(m_{h_2}), \tag{5.29}$$

where $\Gamma^{\rm SM}_{h\to XX}(m_{h_{1(2)}})$ is the Higgs partial decay width in the SM as a function of $m_{h_{1(2)}}$. Experimentally, when two scalar masses are degenerate, it is hard to distinguish the production and decay processes of h_2 from those of h_1 so that the sum of two processes by h_1 and h_2 is to be observed, i.e.,

$$\Gamma_{h_1\to XX} + \Gamma_{h_2\to XX} \simeq \Gamma^{\rm SM}_{h\to XX}(m_h), \tag{5.30}$$

holds for any α. Therefore, the signal strength of Higgs bosons in the CxSM is identical to that in the SM in the degenerate limit of two scalars.

Finally, some approximations should be briefly mentioned. For illustration, we consider the process $gg \to h_i \to VV^*$ where g is gluon and V denotes gauge bosons ($V = W^\pm, Z$). Since $|m_{h_1} - m_{h_2}| > (m_{h_1}\Gamma_{h_1} + m_{h_2}\Gamma_{h_2})/(m_{h_1} + m_{h_2})$ in our model, where Γ_{h_i} are the total decay width of h_i, we can use a narrow decay width approximation [49, 50]. Then the interference terms could be important if $|m_{h_1} - m_{h_2}| \lesssim \Gamma_{h_1} + \Gamma_{h_2}$ [49, 50] (for recent study, see ref. [51]). In our benchmark points, however, the smallest mass differences is 500 MeV and the sum of the total decay widths

are at most $\Gamma_h^{\rm SM} = 4.1$ MeV [52], so the interference terms can be neglected. We also note that the total decay width of the Higgs boson is currently constrained as $\Gamma_h^{\rm exp} < 14.4$ MeV (ATLAS [53]) and $\Gamma_h^{\rm exp} = 3.2^{+2.4}_{-1.7}$ MeV (CMS [54]) and they are not precise enough to constrain Γ_{h_i} in our scenario.

5.2.3 The sum rules for the cancellation mechanism

So far, the degenerate scalar scenario that suppress DM-quark scattering has been discussed using the scalar potential (5.1). This potential is not in general form and employs some global U(1) symmetry breaking terms. The general one takes the form [19]

$$\begin{aligned} V(H,S) = {} & \frac{m^2}{2}H^\dagger H + \frac{\lambda}{4}\left(H^\dagger H\right)^2 + \frac{\delta_2}{2}H^\dagger H|S|^2 + \frac{b_2}{2}|S|^2 + \frac{d_2}{4}|S|^4 \\ & + \left(|a_1|e^{i\phi_{a_1}}S + \frac{|b_1|e^{i\phi_{b_1}}}{4}S^2 + \frac{|\delta_3|e^{i\phi_{\delta_3}}}{4}H^\dagger H S^2 + \frac{|\delta_1|e^{i\phi_{\delta_1}}}{4}H^\dagger H S + \frac{|c_1|e^{i\phi_{c_1}}}{6}S^3 \right. \\ & \left. + \frac{|c_2|e^{i\phi_{c_2}}}{6}S|S|^2 + \frac{|d_1|e^{i\phi_{d_1}}}{8}S^4 + \frac{|d_3|e^{i\phi_{d_3}}}{8}S^2|S|^2 + \text{c.c.}\right), \end{aligned} \tag{5.31}$$

where all terms in parentheses are global U(1) symmetry breaking terms. We now see if the degenerate scalar scenario can be realized using the general potential, and if not, what constraints are brought to the potential.

For the sake of general discussion, we start with the DM-quark scattering amplitudes as in the first lines of Eqs. (5.25) and (5.26). The amplitude with $t \to 0$ becomes

$$i\mathcal{M} = 2i\bar{u}(p_3)u(p_1)\frac{\sqrt{2}m_q}{v}\left(\frac{1}{m_{h_1}^2}C_{\chi\chi h_1}\cos\alpha - \frac{1}{m_{h_2}^2}C_{\chi\chi h_2}\sin\alpha\right), \tag{5.32}$$

where the Yukawa couplings (5.23) are used instead of C_{qqh_1} and C_{qqh_2}.

The general scalar potential in the CxSM allows us to rewrite the trilinear couplings $C_{\chi\chi h}$ and $C_{\chi\chi s}$ by the bilinear couplings C_{hs} and C_{ss} as

$$C_{\chi\chi h} = \frac{A}{v_s}(C_{hs} + \Delta_h), \quad C_{\chi\chi s} = \frac{A}{v_s}(C_{ss} + \Delta_s), \tag{5.33}$$

where parameters A, Δ_h and Δ_s are given by parameters besides C_{hs} and C_{ss} in the scalar potential. Then, we summarize relations of coefficients C_{ij} between the current and mass eigenstates:

$$C_{hh}\cos\alpha + C_{hs}\sin\alpha = C_{11}\cos\alpha, \tag{5.34}$$

$$-C_{hh}\sin\alpha + C_{hs}\cos\alpha = -C_{22}\sin\alpha, \tag{5.35}$$

$$C_{hs}\cos\alpha + C_{ss}\sin\alpha = C_{11}\sin\alpha, \tag{5.36}$$

$$-C_{hs}\sin\alpha + C_{ss}\cos\alpha = C_{22}\cos\alpha. \tag{5.37}$$

Here, for simplicity, $C_{h_1h_1}$ is abbreviated as C_{11} and $C_{h_2h_2}$ as C_{22}. Taking account of Eqs. (5.36), (5.37) and (5.33), we find that the inside of parentheses in (5.32) can be written as

$$\begin{aligned}&\frac{C_{h_1\chi\chi}}{m_{h_1}^2}\cos\alpha-\frac{C_{h_2\chi\chi}}{m_{h_2}^2}\sin\alpha\\&=\frac{A}{v_s}\left[\sin\alpha\cos\alpha\left(\frac{m_{h_1}^2+\Delta_s}{m_{h_1}^2}-\frac{m_{h_2}^2+\Delta_s}{m_{h_2}^2}\right)+\Delta_h\left(\frac{\cos^2\alpha}{m_{h_1}^2}+\frac{\sin^2\alpha}{m_{h_2}^2}\right)\right].\end{aligned}\tag{5.38}$$

Thus, the amplitude (5.32) vanishes in the degenerate scalar scenario when Δ_h satisfies

$$\Delta_h=0.\tag{5.39}$$

In other words, the DM-quark scattering amplitude is not suppressed in the degenerate limit of the mediating mass in the general CxSM, and the coupling $C_{\chi\chi h}$ must be given by C_{hs} alone to suppress DM-quark scattering. The origin of this condition (5.39) can be easily understood using Feynman diagrams of the current eigenstates. Fig. 5.2 shows the Feynman diagram of DM-quark scattering in the current eigenstate of the mediator. Since the singlet scalar s cannot couple with the quark q, the scalar s emitted from DM χ is transformed into the SM Higgs h through the coupling C_{hs} and propagates DM-quark scattering (see right panel of Fig. 5.2). On the other hand, the amplitude mediated by the SM Higgs h is proportional to the coupling $C_{\chi\chi h}$ (middle panel of Fig. 5.2). Thus, the two diagrams cancel only when C_{hs} and $C_{\chi\chi h}$ have a specific relationship. Such a relationship is possible if the origin of the bilinear coupling (C_{hs}) and the trilinear coupling ($C_{\chi\chi h}$) is common, which is why the condition (5.39) is necessary.

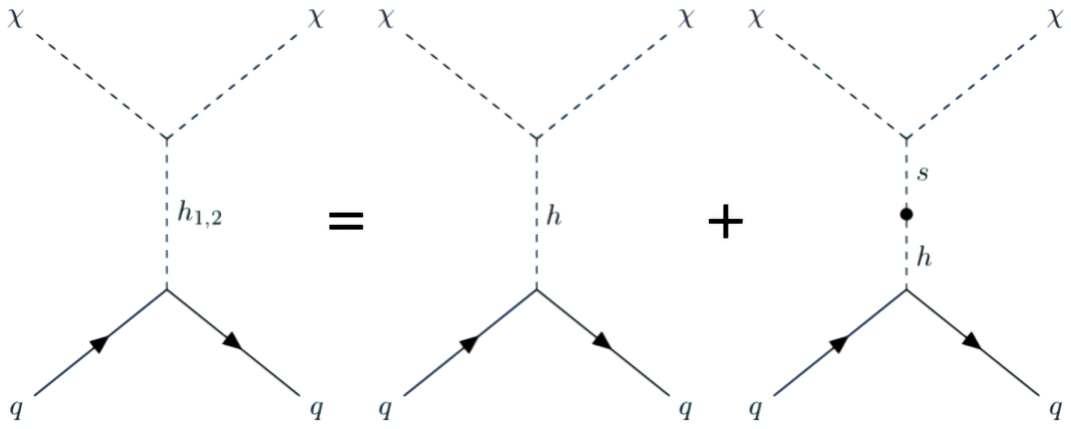

Figure 5.2: Feynman diagrams of the DM-quark scattering in the current and mass eigenstates of scalar mediators.

First, we use the minimal scalar potential (5.1) to confirm that the condition (5.39) is satisfied. In this case, couplings C_{hs} and $C_{\chi\chi h}$, which represent the mixing between the SM Higgs h and the

singlet s or the DM χ are given by

$$\begin{aligned} V_0(H,S) &\supset \frac{\delta_2}{2}|H|^2|S|^2 \\ &\supset C_{\chi\chi h} h\chi^2 + C_{hs} hs, \end{aligned} \tag{5.40}$$

where two couplings are given by

$$C_{\chi\chi h} = \frac{\delta_2}{4} v, \tag{5.41}$$

$$C_{hs} = \frac{\delta_2}{2} v_s v. \tag{5.42}$$

Comparing (5.41) and (5.42) with (5.33), one gets

$$A = \frac{1}{2}, \quad \Delta_h = 0. \tag{5.43}$$

We also evaluate another parameter Δ_s (5.33) for completeness. The couplings $C_{\chi\chi s}$ and C_{ss} are similarly given by

$$\begin{aligned} V_0(H,S) &\supset \frac{\delta_2}{2}|H|^2|S|^2 + \frac{b_2}{2}|S|^2 + \frac{d_2}{4}|S|^4 + \frac{b_1}{4}\left(S^2 + S^{*2}\right) \\ &= C_{\chi\chi s} s\chi^2 + \frac{1}{2} C_{ss} s^2, \end{aligned} \tag{5.44}$$

where two couplings are given by

$$C_{\chi\chi s} = \frac{d_2}{4} v_s, \tag{5.45}$$

$$C_{ss} = \frac{3}{4} d_2 v_S^2 + \frac{\delta_2}{4} v^2 + \frac{b_1}{2} + \frac{b_2}{2}. \tag{5.46}$$

Since (5.43) requires $A = \frac{1}{2}$, Δ_s is given as

$$\begin{aligned} \Delta_s &= -\frac{d_2}{4} v_s^2 - \frac{\delta_2}{4} v^2 - \frac{b_1 + b_2}{2} \\ &= \sqrt{2} \frac{a_1}{v_S}, \end{aligned} \tag{5.47}$$

where we used a tadpole condition (5.5).

Next, we extend the above analysis to the general CxSM. The couplings $C_{\chi\chi h}$ and C_{hs} in the scalar potential of the general CxSM (5.31) are given as follows:

$$\begin{aligned} V(H,S) &\supset \frac{\delta_2}{2}|H|^2|S|^2 + \left(\frac{\delta_1}{4}|H|^2 S + \frac{\delta_3}{4}|H|^2 S^2 + \text{c.c.}\right) \\ &= C_{\chi\chi h} h\chi^2 + C_{hs} hs, \end{aligned} \tag{5.48}$$

where

$$C_{\chi\chi h} = \frac{\delta_2 - \delta_3}{4} v, \tag{5.49}$$

$$C_{hs} = \frac{v}{2}\left(\frac{\delta_1}{\sqrt{2}} + \delta_2 v_S + \delta_3 v_S\right). \tag{5.50}$$

Since δ_1 appears only in C_{hs} (5.50), non-zero δ_1 conflicts with the proportionality between Eqs. (5.49) and (5.50). Comparing (5.49) with (5.50), the condition $\Delta_h = 0$ (5.39) demands one of the following conditions

$$\text{(i)} \quad \delta_1 = \delta_2 = 0, \tag{5.51}$$

$$\text{(ii)} \quad \delta_1 = \delta_3 = 0. \tag{5.52}$$

Note that δ_2 preserves the global U(1) symmetry while δ_1 and δ_3 break it softly. Condition (ii) corresponds to the minimal case. In terms of the symmetry, condition (i) is unnatural because requiring $\delta_2 = 0$ does not recover any symmetry. For completeness, we give couplings $C_{\chi\chi s}$ and C_{ss}

$$C_{\chi\chi s} = \frac{1}{2\sqrt{2}}\left(-c_1 + \frac{c_2}{3}\right) + \frac{d_2 - 3d_1}{4} v_S, \tag{5.53}$$

$$C_{ss} = \frac{b_1 + b_2}{2} + \frac{v_S}{\sqrt{2}}(c_1 + c_2) + \frac{3}{4}(d_1 + d_2 + d_3)v_S^2 + \frac{\delta_2 + \delta_3}{4} v^2. \tag{5.54}$$

Here, we explore the criteria for maintaining the cancellation mechanism within the context of the CxSM with degenerate scalars. Our investigation reveals that the operators in the scalar potential, which describe the mixing between H and S (H-S mixing), play a crucial role in achieving the cancellation. Specifically, the relevant operators for H-S mixing in the general CxSM include δ_1, δ_2, and δ_3. However, we observe that the cancellation mechanism is effective when either the coupling δ_2 and δ_3 is present, and the simultaneous existence of both couplings precludes the cancellation. In contrast, the diverse operators governing the self-interaction of the singlet S operate independently of the cancellation mechanism. Consequently, the scalar potential described by Eq. 5.1 represents the minimal set that successfully realizes the cancellation mechanism.

Finally, we discuss the degenerate scalar scenario of the loop level. In our study [24], we investigated the feasibility of the degenerate scalar scenario in the 1-loop level using the minimal potential (5.1). The results showed that each 1-loop DM-quark scattering diagram was found to cancel (See App. D for details.).

5.2.4 Multi-critical Point Principle

Before concluding the CPC CxSM discussion, a study of the guidelines that predict a degenerate Higgs is conducted. Some parameters, which are introduced in new physics models, are adjusted manually to match the experimental data at low-energy. The Multi-critical Point Principle (MPP) has been proposed as a guiding principle for choosing the model parameters at a low-energy scale[55, 56, 57]. The MPP was used by Froggatt and Nielsen to predict the mass of the SM Higgs accurately, even before the Higgs boson was discovered [58].

In ref. [58], the MPP requires two degenerate vacua in the SM, one at the electroweak scale and the other near the Planck scale. On the other hand, in BSM models with extended scalar sectors, such as the CxSM, there are multiple vacua at low energy scales. The authors of ref. [59] claim that if the MPP is a fundamental principle, the MPP should be applied to all vacua, including ones dominated by the tree-level potential in models with the extended scalar sector. We call this tree-level MPP and we apply this tree-level MPP for the CxSM and study if the degenerate scalar scenario is realized.

Before getting down to business, we review the two vacua in the CxSM. When $(\langle H\rangle,\ \langle S\rangle) = (v,\ v_S)$, the tadpole conditions are given by Eqs. (5.4) and (5.5). On the other hand, the tadpole condition at $(\langle H\rangle,\ \langle S\rangle) = (0,\ v'_S)$ is as follows;

$$\frac{1}{v'_S}\left\langle \frac{\partial V_0}{\partial s}\right\rangle = \frac{b_2}{2} + \frac{d_2}{4}v'^2_S + \frac{\sqrt{2}a_1}{v'_S} + \frac{b_1}{2} = 0. \tag{5.55}$$

Again, the vacuum $(v, 0)$ does not appear in this model because the nonzero v_S is enforced by $a_1 \neq 0$.

We apply the tree-level MPP to the CxSM whose the tree-level scalar potential is given by Eq. (5.1). The difference between the energy densities at these vacua is expressed as

$$\begin{aligned}\Delta V_0 &\equiv V_0(v, v_S) - V_0(0, v'_S)\\ &= \frac{m^2}{8}v^2 + \frac{3\sqrt{2}a_1}{4}(v_S - v'_S) + \frac{b_1 + b_2}{8}(v_S^2 - v'^2_S).\end{aligned} \tag{5.56}$$

When $a_1 = 0$, ΔV_0 is evaluated as

$$\begin{aligned}\Delta V_0 &= \frac{m^2}{8}v^2 + \frac{b_1 + b_2}{8}(v_S^2 - v'^2_S)\\ &\propto -\frac{1}{\lambda d_2 - \delta_2^2}\frac{1}{d_2} \times \left[\delta_2\left(b_2 + b_1\right) - d_2 b_2\right]^2 < 0.\end{aligned} \tag{5.57}$$

If we consider the denominator in Eq. (5.57), it is always positive due to (5.21) with $a_1 = 0$. Consequently, ΔV_0 consistently takes on negative values when the global U(1) symmetry is softly broken solely through the S^2 term, implying the absence of degenerate vacua in this case [59]. However, this outcome undergoes a modification when we introduce the linear term of S into the scalar potential, as illustrated below.

To begin, let us provide a qualitative analysis of the model parameters within the context of the tree-level MPP in the CxSM. It is apparent that the requirement for degenerating two vacua is the non-equality of v_S and v'_S because the first term of the r.h.s. in (5.56) is nonzero and negative. The two VEVs, v_S and v'_S, are determined through tadpole conditions given by (5.5) and (5.55), respectively. The distinction lies in the existence of δ_2 (5.16), representing the mixing between $\mathrm{SU}(2)_L$ doublet and singlet. Hence, in order to achieve $\Delta V_0 = 0$, it is necessary for both δ_2 and

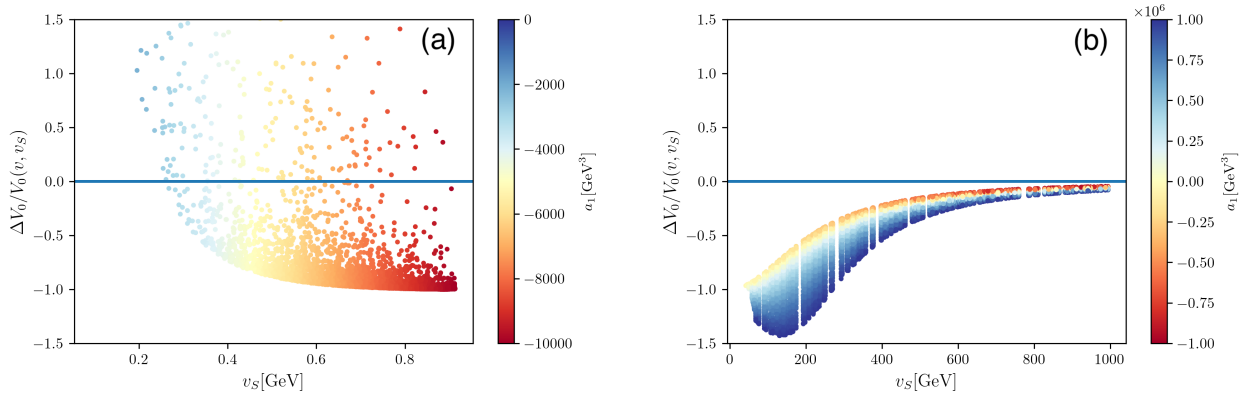

Figure 5.3: The potential difference for $v_S = 0.1 - 1$ GeV (a) and $v_S = 100 - 1000$ GeV (b) in the degenerate scalar scenario. The color bar represents the change in a_1.

$v_S - v'_S$ to be sizable. In the degenerate scalar scenario, since the mass difference ($m^2_{h_1} - m^2_{h_2}$ in (5.16)) is small, v_S should be small to make δ_2 sizable as can be seen from Eq. (5.16). Large δ_2 is realized by small v_S and large $\sin 2\alpha$.

We quantitatively discuss the parameter space in the CxSM with degenerate scalars chosen by applying the tree-level MPP. We set $m_\chi = 62.5$ GeV and the second Higgs mass $m_{h_2} = 124$ GeV. While the degenerate scalar scenario imposes no constraints on the mixing angle α as discussed in Section 5.1, a significant α is essential for enhancing the magnitude of δ_2. Therefore, we adopt the mixing angle $\alpha = \pi/4$ here. Fig. 5.3 shows the potential difference scaled by the energy density of the electroweak vacuum $\Delta V_0/V_0(v, v_S)$ as a function of v_S. The range of v_S is $0.1-1$ GeV (Fig. 5.3(a)) and $100-1000$ GeV (Fig. 5.3(b)). Considering the theoretical constraints for the scalar potential outlined in Eqs.(5.19)-(5.21), There was no parameter space allowed for $v_S = 10$ 100 GeV. Consequently, this particular range is excluded from the figure. The color bar represents the a_1 dependence. In the case of small v_S (Fig. 5.3(a)), $\Delta V_0/V_0(v, v_S)$ can be either positive or negative. Conversely, for large v_S (Fig. 5.3(b)), $\Delta V_0/V_0(v, v_S)$ approaches zero but does not reach zero. Consequently, the realization of degenerate vacua occurs exclusively when v_S is on the order of $\mathcal{O}(0.1)$.

5.3 Electroweak phase transition

In this section, we discuss the feasibility of strong first-order EWPT in the CxSM. As noted in Sec. 3.2.1, strong first-order EWPT is required to explain the departure from thermal equilibrium in EWBG, which is expressed as $v_C/T_C \gtrsim 1$ (3.17). Our vacuum is such that H and S both have VEVs, i.e., $(\langle H\rangle,\ \langle S\rangle) = (v,\ v_S)$. We can also consider the case where only S takes a VEV $(\langle H\rangle,\ \langle S\rangle) = (0,\ v'_S)$. Note that since nonzero v_S is enforced by $a_1 \neq 0$, the vacuum $(v, 0)$ does not

appear in this model. Therefore, the symmetry in the S-direction is broken from the beginning, so this model follows the thermal history from $(0,\ v_S'(T))$ to $(v(T),\ v_S(T))$.

In general, first-order EWPT requires cubic terms of the scalar fields brought about by finite-temperature effects, but in the CxSM, the tree-level structure makes the most important contribution to first-order EWPT. We first confirm contribution of the tree-level structure using a simplified potential, called the High Temperature (HT) potential. This potential consists of a tree-level potential and thermal masses which are the quadratic terms of the field extracted from the finite temperature effective potential. Since the cubic terms of the field derived from the finite-temperature effects do not appear here, the tree-level effects can be evaluated qualitatively. Furthermore, by calculating T_C and v_C using the HT potential, we derive the conditions that strong first-order EWPT imposes on the parameters.

The full effective potential is used for quantitative discussions. We use several calculation schemes of the effective potential and mention their differences as well. In addition, we compare the observed and experimental data with the DM relic density and spin-independent DM-quark scattering cross section that the model predicts, and evaluate the parameter space that explains both EWPT and DM without contradiction.

5.3.1 Qualitative study

Here, we denote the classical background fields of the Higgs doublet and singlet as

$$\langle H\rangle = (0 \quad \varphi)^T/\sqrt{2}, \quad \langle S\rangle = \varphi_S/\sqrt{2}, \tag{5.58}$$

where we consider the Landau gauge $\xi = 0$ with ξ representing a gauge-fixing parameter. Because of the presence of the singlet field in the CxSM, the potential barrier is induced by the doublet-singlet mixing that exists in the tree-level[2]. To check this, we first examine EWPT using the HT potential given by

$$V^{\rm HT}(\varphi,\varphi_S;T) = V_0(\varphi,\varphi_S) + \frac{1}{2}\left(\Sigma_H\varphi^2 + \Sigma_S\varphi_S^2\right)T^2, \tag{5.59}$$

where

$$\Sigma_H = \frac{\lambda}{8} + \frac{\delta_2}{24} + \frac{3g_2^2+g_1^2}{16} + \frac{y_t^2}{4}, \quad \Sigma_S = \frac{\delta_2+d_2}{12}. \tag{5.60}$$

g_2, g_1 and y_t are $\mathrm{SU}(2)_L$, $\mathrm{U}(1)_Y$ and top Yukawa couplings, respectively. Note that $V^{\rm HT}$ is gauge dependence due to the gauge-invariant thermal masses as mentioned in Chapter. 5.

As can be seen from Eqs. (5.59),(5.60), although the HT potential does not include the cubic terms of the field, the potential barrier is induced by the tree-level structure. To confirm this

[2]for classification of first-order phase transitions, see, e.g., ref. [60]

origin, we first parametrize the two scalar fields using radial coordinates as

$$\varphi = z\cos\gamma, \quad \varphi_S = z\sin\gamma + v'_S, \tag{5.61}$$

where v'_S represents the minimum on the φ_S axis, which is always nonzero due to $a_1 \neq 0$ in this model. The HT potential can be rewritten as

$$V^{\rm HT}(z,\gamma;T) = c_0 + c_1 z + \left(c_2 + c'_2 T^2\right) z^2 - c_3 z^3 + c_4 z^4 \tag{5.62}$$

where

$$c_0 = \sqrt{2}a_1 v'_s(T) + \frac{1}{4}\left(b_1 + b_2 + 2\Sigma_S T^2\right)\left(v'_s(T)\right)^2 + \frac{1}{16}\left(v'_s(T)\right)^4, \tag{5.63}$$

$$c_1 = \left(\sqrt{2}a_1 + \frac{1}{2}\left(b_1 + b_2 + 2\Sigma_S T^2\right) v'_s(T) + \frac{1}{4}d_4\left(v'_s(T)\right)^3\right)\sin\gamma, \tag{5.64}$$

$$c_2 = \frac{1}{4}\left((b_1+b_2)\sin^2\gamma + m^2\cos^2\gamma\right) + \frac{1}{8}\left(3d_2\sin^2\gamma + \delta_2\cos^2\gamma\right)\left(v'_s(T)\right)^2, \tag{5.65}$$

$$c'_2 = \frac{1}{2}\left(\Sigma_H\cos^2\gamma + \Sigma_S\sin^2\gamma\right), \tag{5.66}$$

$$c_3 = -\frac{1}{4}\sin\gamma\left(d_2\sin^2\gamma + \delta_2\cos^2\gamma\right) v'_s(T), \tag{5.67}$$

$$c_4 = \frac{1}{16}\left(d_2\sin^4\gamma + 2\delta_2\sin^2\gamma\cos^2\gamma + \lambda\cos^4\gamma\right). \tag{5.68}$$

From Eq. (5.62), it can be seen that the negative cubic terms of the scalar fields appear. This is exactly the terms derived from the tree-level structure that contributes significantly to first-order EWPT. Looking at the coefficients of the cubic term (5.67), it consists of the quartic terms of the singlet scalar d_2 and the $\mathrm{SU}(2)_L$ doublet-singlet mixing δ_2.

When the 1st oreder EWPT occurs at $T = T_C$, the HT potential takes the from

$$V^{\rm HT}(z,\gamma;T_c) = c_4 z^2\left(z - \frac{c_3}{2c_4}\right)^2, \tag{5.69}$$

where the subscripts C indicate that the quantities are evaluated at T_C. Then, T_C and v_C are as follows;

$$T_C^2 = \frac{1}{2(\Sigma_H + \Sigma_S t_{\gamma_C}^2)}\Bigg[-m^2 - \frac{(v'_{SC})^2\delta_2}{2} - \left\{b_1 + b_2 + \left(\frac{3d_2}{2} - \frac{(\delta_2 + d_2 t_{\gamma_C}^2)^2}{\lambda + 2\delta_2 t_{\gamma_C}^2 + d_2 t_{\gamma_C}^4}\right)(v'_{SC})^2\right\} t_{\gamma_C}^2\Bigg], \tag{5.70}$$

$$v_C = \frac{-2t_{\gamma_C}(v'_{SC})^2(\delta_2 + d_2 t_{\gamma_C}^2)}{\lambda + 2\delta_2 t_{\gamma_C}^2 + d_2 t_{\gamma_C}^4}, \tag{5.71}$$

with

$$t_{\gamma_C} = \frac{\sin\gamma(T_C)}{\cos\gamma(T_C)} = \frac{v_{SC} - v'_{SC}}{v_C}, \quad v_C = \lim_{T\nearrow T_C} v(T), \quad v_{SC} = \lim_{T\nearrow T_C} v_S(T), \quad v'_{SC} = \lim_{T\searrow T_C} v_S(T), \tag{5.72}$$

where $T \nearrow T_C$ and $T \searrow T_C$ are defined such that T approaches T_C from below and above, respectively. For $t_{\gamma_C} \ll 1$, T_C and v_C can be approximated as [33]

$$T_C \simeq \sqrt{\frac{1}{2\Sigma_H}\left(-m^2 - \frac{(v'_{SC})^2}{2}\delta_2\right)}, \tag{5.73}$$

$$v_C \simeq \sqrt{\frac{2\delta_2 (v'_{SC})^2}{\lambda}\left(1 - \frac{v_{SC}}{v'_{SC}}\right)}. \tag{5.74}$$

From the expression of T_C (5.73) and v_C (5.74) and the sphaleron decoupling condition (3.17), we find the conditions for the parameters that favor a strong first-order EWPT. First, as seen from Eq. (5.73), T_C would get lowered if δ_2 is positive and sizable. Expressing δ_2 in terms of the Lagrangian parameters yields

$$\delta_2 = \frac{2}{v v_S}(m_{h_1}^2 - m_{h_2}^2)\sin\alpha\cos\alpha. \tag{5.75}$$

Since we are now considering the degenerate scalar scenario, a small v_S is needed to increase δ_2. Moreover, the maximal mixing $|\alpha| = \pi/4$ is also preferred.

Next, we turn our attention to v_C. From Eq. (5.74), v_C would also be enhanced with an amplification factor $(v'_{SC})^2(1 - v_{SC}/v'_{SC})$. v'_{SC} is determined by the cubic equation

$$(v'_{SC})^3 + \frac{2(b_1 + b_2 + 2\Sigma_S)}{d_2} v'_{SC} + \frac{4\sqrt{2}a_1}{d_2} = 0. \tag{5.76}$$

When this equation yields real solutions, it is found to be scaled by $1/\sqrt{d_2}$, which indicates that smaller d_2 is needed for larger v_C. By expressing the Lagrangian parameters in terms of the input parameters, one finds

$$d_2 = \frac{2}{v_S^2}\left[m_{h_1}^2 + (m_{h_2}^2 - m_{h_1}^2)\cos^2\alpha + \frac{\sqrt{2}a_1}{v_S}\right]. \tag{5.77}$$

Here, the degenerate scalar scenario is considered, d_2 can be rewritten as

$$d_2 \simeq \frac{2}{v_S^2}\left[m_{h_1}^2 + \frac{\sqrt{2}a_1}{v_S}\right]. \tag{5.78}$$

The size and sign of a_1 is important *i.e.*, $a_1 < 0$ is favored, to keep d_2 small because of the small v_S preferred for sizable δ_2.

To summarize the above discussion, to obtain strong first-order EWPT in the degenerate scalar scenario, we need

(i) large δ_2 with a positive sign, *i.e.*, $|\alpha| \simeq \pi/4$ and $v_S < 1$ GeV,

(ii) small d_2, *i.e.*, $a_1 < 0$ with its moderate absolute value.

Inputs	v [GeV]	m_{h_1} [GeV]	m_{h_2} [GeV]	α [rad]	a_1 [GeV^3]	v_S [GeV]	m_χ [GeV]
BP1	246.22	125	124	$\pi/4$	-6576.17	0.6	62.5
BP2	246.22	125	126	$-\pi/4$	-6682.25	0.6	62.5
Outputs	m^2 [GeV^2]	b_1 [GeV^2]	b_2 [GeV^2]	λ	a_1 [GeV^3]	d_2	δ_2
BP1	$-(124.5)^2$	$-(107.7)^2$	$-(178.0)^2$	0.511	-6576.17	1.77	1.69
BP2	$-(125.5)^2$	$-(108.8)^2$	$-(178.4)^2$	0.520	-6682.25	1.70	1.59

Table 5.1: Input and output parameters of the two benchmark points. These BPs satisfy all theoretical constraints.

Here, the HT potential was used to evaluate the parameters that are likely to cause a strong first-order EWPT. However, even though the HT potential is useful to discuss EWPT qualitatively, the full 1-loop contributions would not be negligible for quantitative study. In order to incorporate higher-order corrections, we employ two gauge-invariant calculation schemes on the scalar potential and two familiar resummation methods in evaluating 1-loop (gauge dependent) effective potential. The former two is the HT potential and the Patal-Ramsey-Musolf (PRM) scheme, and the latter two is the 1-loop effective potential with Parwani [35] and Arnold-Espinosa (AE) [36] schemes for the resummation. For each specific potential form, see Sec. 3.2.2 and Eq. (5.59). However, with respect to the PRM scheme in our work, T_C is determined to $\mathcal{O}(\hbar)$ using the following degeneracy condition [30]

$$V_0(0, v'_{S,\text{tree}}) + V_1(0, v'_{S,\text{tree}}; T) = V_0(v_{\text{tree}}, v_{S,\text{tree}}) + V_1(v_{\text{tree}}, v_{S,\text{tree}}; T), \tag{5.79}$$

where v_{tree}, $v_{S,\text{tree}}$, and $v'_{S,\text{tree}}$ are the tree-level VEVs at $T = 0$.

5.3.2 Numerical results

First, we show the DM relic density $\Omega_\chi h^2$ and the SI DM-nucleon scattering cross section σ_{SI} in parameter space that satisfies the condition of strong first-order EWPT discussed. For illustration, consider two benchmark points (BPs) in the table 5.1. For the moment, we treat m_χ as a varying parameter. In our study, we calculate $\Omega_\chi h^2$ and σ_{SI} using the public code `micrOMEGAs` [61]. The value of $\Omega_\chi h^2$ should not exceed the observed value [4]

$$\Omega_{\text{DM}} h^2 = 0.1200 \pm 0.0012. \tag{5.80}$$

On the other hand, σ_{SI} is constrained by DM direct detection experiments. If $\Omega_\chi < \Omega_{\text{DM}}$, we σ_{SI} is scaled as

$$\widetilde{\sigma}_{\text{SI}} = \left(\frac{\Omega_\chi}{\Omega_{\text{DM}}}\right) \sigma_{\text{SI}}, \tag{5.81}$$

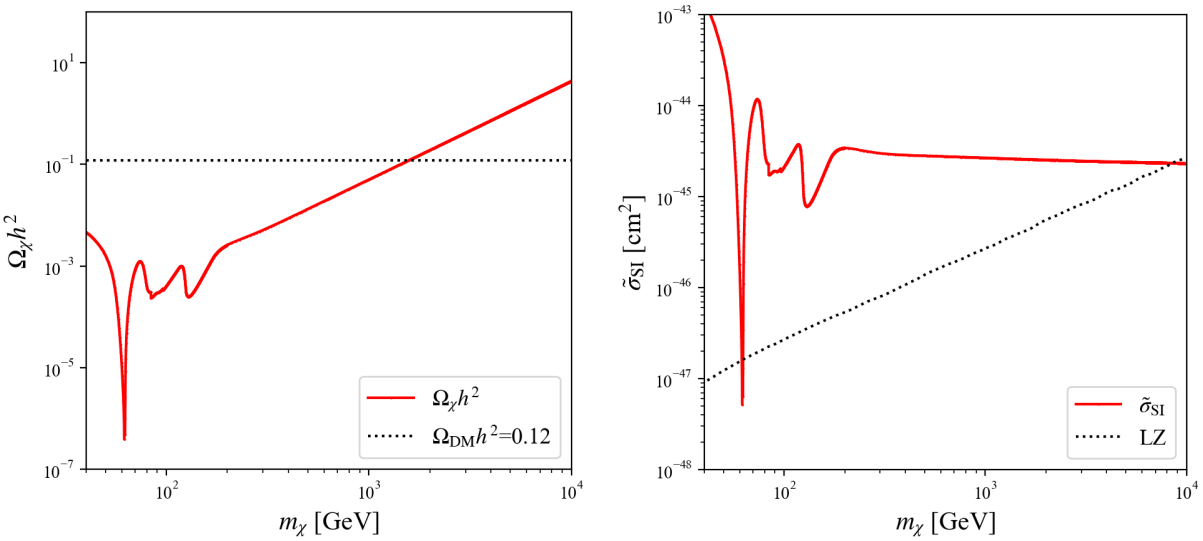

Figure 5.4: The DM relic density $\Omega_\chi h^2$ (left panel) and scaled SI scattering cross section with the nucleons $\widetilde{\sigma}_{\rm SI}$ (right panel) are plotted as a function of the DM mass m_χ. We take BP1 for illustration. The horizontal dotted lines in the left panel is the central value of the observed DM relic density, while the dotted curve in the right panel is the LZ experiment data.

which should satisfy the direct detection experimental bounds. In the following, only results for BP1 are presented, but almost the same results can be obtained using BP2.

$\Omega_\chi h^2$ is displayed as a function of m_χ in the left panel of Fig. 5.4. The horizontal dotted line is the value of the observed DM relic density (5.80). The results show that χ cannot constitute the total amount of DM until around the mass 2 TeV where $\Omega_\chi = \Omega_{\rm DM}$. The sharp dip around $m_\chi = m_{h_{1,2}}/2$ ($\simeq$ 62.5 GeV) reflects resonant enhancements of s-channel annihilation processes mediated by h_1 and h_2. In the right panel of Fig. 5.4, $\widetilde{\sigma}_{\rm SI}$ is displayed as a function of m_χ. The dotted curve represents the LZ experiment data. It can be seen that the $\widetilde{\sigma}_{\rm SI}$ around $m_\chi = 62.5$ GeV is suppressed enough to avoid the LZ bound, but this is due to the dip in $\Omega_\chi h^2$ mentioned above.

In summary, $\sigma_{\rm SI}$ is not generally suppressed by the mass degeneracy of h_1 and h_2. This is because large δ_2 and small v_S are chosen to realize strong first-order EWPT, which is contrary to the degenerate scalar scenario that requires suppression of δ_2 for reasonably sized v_S, as can be seen from Eq. (5.27). In the following, we analyze EWPT with $m_\chi = 62.5$ GeV.

In Figs. 5.5 and 5.6, we display the temperature evolutions of VEVs in BP1 and BP2. Since BP1 and BP2 give almost the same results, although there are some differences in their numerical values, we focus our comments here on BP1. In the left panel, the HT potential and the PRM scheme are used. $v(T)$ and $v_S(T)$ required by the HT potential are shown by red solid and blue dotted curves respectively, where magnified $v_S(T)$ is also plotted in the small window. In addition,

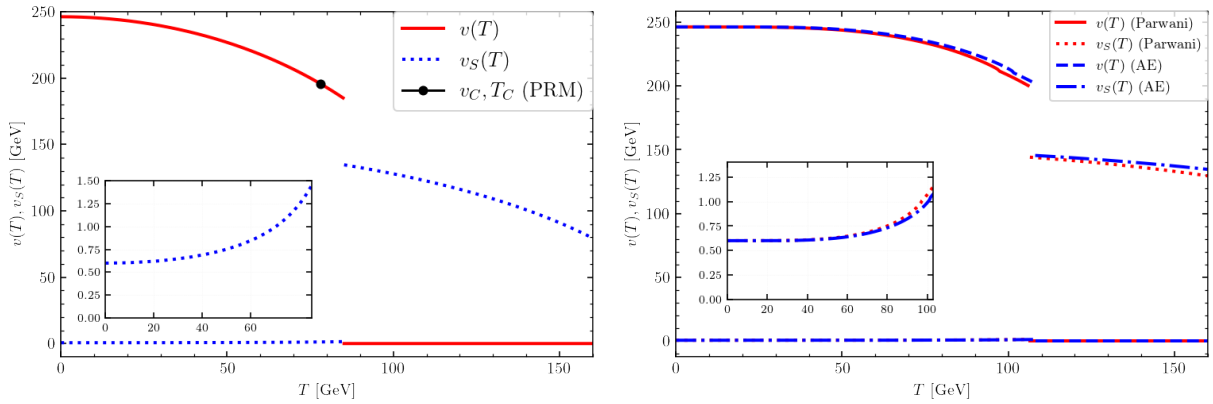

Figure 5.5: $v(T)$ and $v_S(T)$ are shown as functions of the temperature T in BP1. The HT potential and the PRM scheme are used in the left panel, while 1-loop effective potentials with the Parwani and AE resummation schemes are used in the right panel.

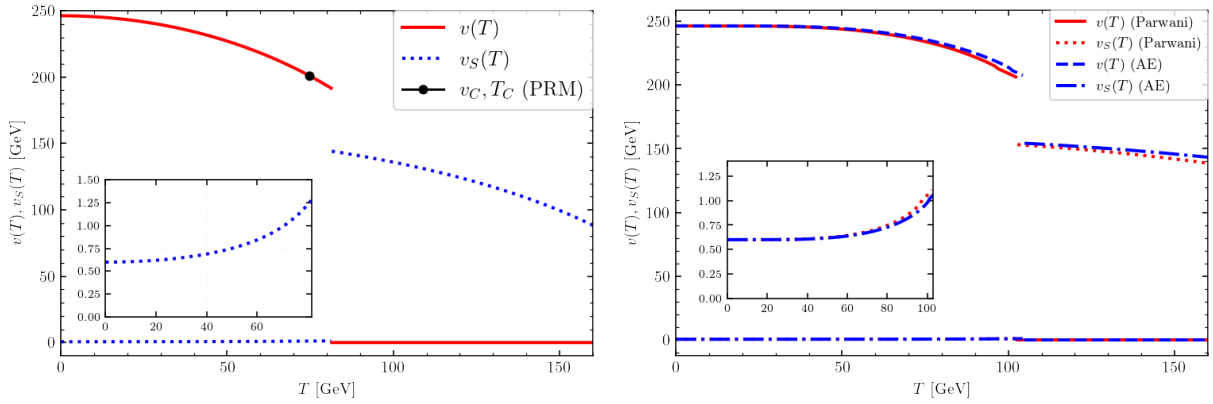

Figure 5.6: $v(T)$ and $v_S(T)$ are shown as functions of the temperature T in BP2.

	BP1			
Scheme	HT	PRM	Parwani	AE
v_C/T_C	$\frac{184.4}{85.3} = 2.2$	$\frac{195.6}{78.2} = 2.5$	$\frac{201.5}{106.8} = 1.9$	$\frac{202.7}{107.8} = 1.9$
v_{SC} [GeV]	1.5	1.2	1.2	1.2
$v_{SC}^{\rm sym}$ [GeV]	134.6	137.3	144.8	145.3
	BP2			
	HT	PRM	Parwani	AE
v_C/T_C	$\frac{191.3}{81.5} = 2.3$	$\frac{201.0}{74.8} = 2.7$	$\frac{206.3}{102.8} = 2.0$	$\frac{208.3}{104.4} = 2.0$
v_{SC} [GeV]	1.3	1.1	1.1	1.1
$v_{SC}^{\rm sym}$ [GeV]	144.2	146.6	153.2	154.1

Table 5.2: T_C and the corresponding Higgs VEVs in BP1 and BP2 using the four calculation schemes. 'HT' stands for the high-temperature scheme in which the potential (5.59) is used, 'PRM' denotes the gauge-invariant calculation scheme proposed by Patel and Ramsey-Musolf [30]. 'Parwani' refers to the ordinary 1-loop calculation with the thermal resummation adopted in the work of Parwani [35], while 'AE' defines the same 1-loop effective potential calculation with the thermal resummation dopted in the work of Arnold and Espinosa [36].

v_C and T_C with PRM scheme are given by black circle. As clearly seen, discontinuity exists in the temperature evolutions of VEVs.

In the right panel of Figs. 5.5 and 5.6, 1-loop effective potentials with the Parwani and AE resummation schemes are used to evaluate the temperature evolution of VEVs. The solid and dotted lines in red represent $v(T)$ and $v_S(T)$ in the Parwani scheme, while the dashed and dotted lines in blue denote ones in the AE scheme, respectively. The graph shows that there is little difference in the numerical values depending on the thermal resummation scheme, because EWPT of the CxSM is dominated by the tree-level potential.

The specific values are shown in Table 5.2. In both cases, v_C/T_C is about 10% lower with full 1-loop compared to HT potential, all schemes satisfy the sphaleron decoupling condition (3.17). In conclusion, strong first-order EWPT in the degenerate scalar scenario is possible both for $m_{h_1} > m_{h_2}$ and for $m_{h_1} < m_{h_2}$.

5.4 Summary of Chapter 5

In this chapter, we used CP-conserving CxSM to discuss EWPT, which is an integral part of EWBG. In addition, the tree-level MPP is applied and requirements for model parameters are discussed.

We have investigated the compatibility of the degenerate scalar scenarios and the strong first-order EWPT in the CxSM. The degenerate scalar scenario suppresses DM-quark scattering regardless of DM mass and interaction magnitude, giving a solution that satisfies the DM direct detection experiment [46]. For this degenerate scalar scenario to hold, suppression of δ_2 for moderate magnitude of v_S is essential, as can be seen from Eq. (5.27). On the other hand, the first-order EWPT of the CxSM is driven by the tree-level potential and $\mathrm{SU}(2)_L$ doublet-singlet mixing plays the most important role. Therefore, large δ_2 is preferred in the context of the strong first-order EWPT, and then small v_S and the maximum mixing angle $\alpha = \pi/4$ are required (See Eq. (5.75)).

We have considered two benchmark points, in which the additional Higgs mass is fixed at $m_{h_2} = 124$ GeV for BP1 and $m_{h_2} = 10$ GeV for BP2. Our numerical analysis showed only the DM mass $m_\chi \simeq 62.5$ GeV is consistent with the DM observations (Fig. 5.4). Only this region, which reflects the resonance enhancement of DM, was compatible with the degenerate scalar scenario and the strong first-order EWPT. Then the four calculation schemes used to analyze EWPT are the gauge-independent ways: HT and PRM and the gauge-dependent conventional effective potentials: Parwani and AE. The strong first-order EWPT was obtained using any of them (Fig. 5.5,5.6).

We have also considered the origin of the degenerate scalar scenario by using the scalar potential of the general CxSM and found that the mixing term of H and S is restricted besides the orthogonality of the matrix mixing CP-even scalar particles. Furthermore, we adopted the tree-level MPP as a possible guiding principle that predicts the degenerate Higgs. We found the parameter space where two vacua are degenerate with small v_S (Fig. 5.3).

In the next section, we consider the CP-violating CxSM for EWBG realization. In this case, χ is no longer DM candidate and the DM issue must be left to others. For studies of other DM candidate examples, see, for example, ref. [62].

Chapter 6

CP-violating CxSM

From Sakharov conditions, CP symmetry violation is essential for EWBG; since CP-conserving scalar potentials were used in Chapter 5, here we treat the CP-violating scalar potential by making the coefficients of the global U(1) symmetry breaking terms and VEV of S complex. However, since the stability of the imaginary part of S was guaranteed by CP symmetry, this time χ is not treated as DM but as an ordinary decaying particle.

First, we quantify the influence of CPV on first-order EWPT, with a specific focus on the degenerate scalar scenario—an area of continued interest due to its status as an experimental blind spot independent of DM considerations. To clarify differences from the CP-conserving (CPC) case [22], we qualitatively examine the EWPT using a tree-level potential with thermal masses, referred to as the high-temperature (HT) potential in this context. Conversely, a comprehensive numerical study employs a finite temperature 1-loop effective potential with the Parwani resummation method [35]. As a phenomenological consequence of the first-order EWPT, we also evaluate GWs generation [63, 64], resulting from the dynamics of bubbles and thermal plasma. These GWs may serve as a supplementary means to probe the experimental blind spot.

Then, we explore the feasibility of EWBG within the CxSM incorporating higher-dimensional operators. Specifically, we examine cases where the complex phase is present in the scalar potential, and this phase is communicated to the Standard Model (SM) fermion sector through dimension-5 Yukawa interactions, both with and without complex coefficients. Our investigation indicates that the inclusion of a complex phase in the scalar potential provides a suitable range of values for BAU without resorting the use of complex coefficients in higher-dimensional operators. Additionally, EDM of the electron (d_e) can be suppressed due to Higgs mass degeneracy and new electron Yukawa coupling, effectively avoiding the most recent constraints imposed by the JILA experiment.

6.1 The Model

As mentioned in Chapter 5, the CxSM is the extension of the SM by adding the complex $SU(2)_L$ gauge singlet scalar field S. The model was proposed in ref. [19] and shows that DM can exist if the scalar potential is invariant under CP transformation $S \to S^*$, and a VEV of S is real. Phenomenological studies of DM can be conducted in Refs. [20, 21]. Furthermore, one could obtain the strong first-order EWPT in this model [43, 65, 33, 66, 67, 68, 22].

The comprehensive CPC scalar potential, as outlined in [19], encompasses a total of 11 new parameters. Given that not all of these parameters pertain directly to DM and EWPT physics, we focus our attention on a minimal scalar potential denoted as

$$V_0(H,S) = \frac{m^2}{2}H^\dagger H + \frac{\lambda}{4}\left(H^\dagger H\right)^2 + \frac{\delta_2}{2}H^\dagger H|S|^2 + \frac{b_2}{2}|S|^2 + \frac{d_2}{4}|S|^4 + \left(a_1 S + \frac{b_1}{4}S^2 + \text{H.c.}\right). \tag{6.1}$$

where both a_1 and b_1 break a global U(1) symmetry, preventing an undesired massless particle. Additionally, the introduction of a_1 is essential to mitigate a potential domain wall issue that may arise during the spontaneous breaking of the Z_2 symmetry, where $V_0(H,S) \to V_0(H,-S)$.

If the Higgs sector maintains CP conservation, the real and imaginary components of S remain independent, allowing the latter to potentially serve as DM candidate. However, for Electroweak Baryogenesis (EWBG) to occur, new CPV is required. Furthermore, the condition of the strong first-order EWPT in this minimal CxSM results in the DM relic density being significantly lower than the observed value within the viable DM mass range of approximately 62.5 GeV [22]. This necessitates the introduction of an additional stable particle as a primary constituent of the DM abundance. Hence, it is more rational to consider the CxSM that incorporates CPV, leaving the DM-related challenges to be addressed in a more comprehensive theoretical framework[1].

We parametrize the scalar fields as

$$H(x) = \begin{pmatrix} G^+(x) \\ \frac{1}{\sqrt{2}}\left(v + h(x) + iG^0(x)\right) \end{pmatrix}, \tag{6.2}$$

$$\begin{aligned} S(x) &= \frac{1}{\sqrt{2}}\left(v_S^r + iv_S^i + s(x) + i\chi(x)\right) \\ &= \frac{1}{\sqrt{2}}\left(|v_S|e^{i\theta_S} + s(x) + i\chi(x)\right) \end{aligned} \tag{6.3}$$

where h is the SM-like Higgs field and $v(\simeq 246.22$ GeV) is its VEV, while G^0 and G^+ are Nambu-Goldsone (NG) fields. v_S^r and v_S^i are the VEVs of s and χ, respectively. For future reference, let us express $a_1 = a_1^r + ia_1^i$ and $b_1 = b_1^r + ib_1^i$.

[1] See ref. [62] for new DM implementation attempts.

Tadpole conditions with respect to h, s and χ are, respectively, given by

$$\left\langle \frac{\partial V_0}{\partial h} \right\rangle = v\left[\frac{m^2}{2} + \frac{\lambda}{4}v^2 + \frac{\delta_2}{4}|v_S|^2\right] = 0, \tag{6.4}$$

$$\left\langle \frac{\partial V_0}{\partial s} \right\rangle = v_S^r\left[\frac{b_2}{2} + \frac{\delta_2}{4}v^2 + \frac{d_2}{4}|v_S|^2 + \frac{b_1^r}{2}\right] + \sqrt{2}a_1^r - \frac{1}{2}b_1^i v_S^i = 0, \tag{6.5}$$

$$\left\langle \frac{\partial V_0}{\partial \chi} \right\rangle = v_S^i\left[\frac{b_2}{2} + \frac{\delta_2}{4}v^2 + \frac{d_2}{4}|v_S|^2 - \frac{b_1^r}{2}\right] - \sqrt{2}a_1^i - \frac{1}{2}b_1^i v_S^r = 0, \tag{6.6}$$

where $\langle\cdots\rangle$ signifies that all fluctuation fields become zero after the derivative. Here, v_S^r is non-zero if $a_1^r \neq 0$.

The tree-level masses of the scalars are obtained by

$$-\mathcal{L}_{\rm mass} = \frac{1}{2}\begin{pmatrix} h & s & \chi \end{pmatrix}\mathcal{M}_S^2\begin{pmatrix} h \\ s \\ \chi \end{pmatrix} = \frac{1}{2}\begin{pmatrix} h_1 & h_2 & h_3 \end{pmatrix}O^T\mathcal{M}_S^2 O\begin{pmatrix} h_1 \\ h_2 \\ h_3 \end{pmatrix} = \frac{1}{2}\sum_{i=1}^{3} m_{h_i}^2 h_i^2. \tag{6.7}$$

The mass matrix is specifically obtained with

$$\mathcal{M}_S^2 = \begin{pmatrix} \frac{\lambda}{2}v^2 & \frac{\delta_2}{2}vv_S^r & \frac{\delta_2}{2}vv_S^i \\ \frac{\delta_2}{2}vv_S^r & \frac{d_2}{2}v_S^{r2} - \frac{\sqrt{2}a_1^r}{v_S^r} + \frac{b_1^i}{2}\frac{v_S^i}{v_S^r} & -\frac{b_1^i}{2} + \frac{d_2}{2}v_S^r v_S^i \\ \frac{\delta_2}{2}vv_S^i & -\frac{b_1^i}{2} + \frac{d_2}{2}v_S^r v_S^i & \frac{d_2}{2}v_S^{i2} + \frac{\sqrt{2}a_1^i}{v_S^i} + \frac{b_1^i}{2}\frac{v_S^r}{v_S^i} \end{pmatrix}, \tag{6.8}$$

which is diagonalize by the mixing matrix O is parametrized as

$$O(\alpha_i) = \begin{pmatrix} 1 & 0 & 0 \\ 0 & c_3 & -s_3 \\ 0 & s_3 & c_3 \end{pmatrix}\begin{pmatrix} c_2 & 0 & -s_2 \\ 0 & 1 & 0 \\ s_2 & 0 & c_2 \end{pmatrix}\begin{pmatrix} c_1 & -s_1 & 0 \\ s_1 & c_1 & 0 \\ 0 & 0 & 1 \end{pmatrix}, \tag{6.9}$$

with $s_i = \sin\alpha_i$ and $c_i = \cos\alpha_i$ $(i = 1, 2, 3)$. In addition, from Eq. (6.7), the following relational equation is obtained:

$$\left(\mathcal{M}_S^2\right)_{ij} = \sum_k O_{ik}O_{jk}m_{h_k}^2. \tag{6.10}$$

For later convenience, we mention the relationship between input and output parameters. There are nine parameters in the scalar potential, $\{m^2, \lambda, \delta_2, b_2, d_2, a_1^r, a_1^i, b_1^r, b_1^i\}$. In this work, we take $m_{h_1} = 125$ GeV and $b_1^i = 0$ without loss of generality. Among the Lagrangian parameters, m^2, b_2 and b_1^r are eliminated from the tadpole conditions (6.4),(6.5) and (6.6),

$$m^2 = -\frac{\lambda}{2}v^2 - \frac{\delta_2}{2}|v_S|^2, \tag{6.11}$$

$$b_2 = -\frac{\delta_2}{2}v^2 - \frac{d_2}{2}|v_S|^2 - \sqrt{2}\left(\frac{a_1^r}{v_S^r} - \frac{a_1^i}{v_S^i}\right), \tag{6.12}$$

$$b_1^r = -\sqrt{2}\left(\frac{a_1^r}{v_S^r} + \frac{a_1^i}{v_S^i}\right). \tag{6.13}$$

The remaining five parameters are given as

$$\lambda = \frac{2}{v^2}\sum_i O_{1i}^2 m_{h_i}^2, \tag{6.14}$$

$$\delta_2 = \frac{2}{v v_S^r}\sum_i O_{1i}O_{2i}m_{h_i}^2 = \frac{2}{v v_S^i}\sum_i O_{1i}O_{3i}m_{h_i}^2, \tag{6.15}$$

$$d_2 = \frac{2}{v_S^{r2}}\left[\frac{\sqrt{2}a_1^r}{v_S^r} + \sum_i O_{2i}^2 m_{h_i}^2\right] = \frac{2}{v_S^{i2}}\left[-\frac{\sqrt{2}a_1^i}{v_S^i} + \sum_i O_{3i}^2 m_{h_i}^2\right] = \frac{2}{v_S^r v_S^i}\left[\sum_i O_{2i}O_{3i}m_{h_i}^2\right], \tag{6.16}$$

$$a_1^r = -\frac{v_S^r}{\sqrt{2}}\left[\sum_i O_{2i}\left(O_{2i} - O_{3i}\frac{v_S^r}{v_S^i}\right)m_{h_i}^2\right], \tag{6.17}$$

$$a_1^i = \frac{v_S^i}{\sqrt{2}}\left[\sum_i O_{3i}\left(O_{3i} - O_{2i}\frac{v_S^i}{v_S^r}\right)m_{h_i}^2\right], \tag{6.18}$$

Note that α_3 is not an independent parameter and determined by the second equality in Eq. (6.15)

$$\sum_i O_{1i}\left[\frac{O_{2i}}{v_S^r} - \frac{O_{3i}}{v_S^i}\right]m_{h_i}^2 = \frac{(\mathcal{M}_S^2)_{12}}{v_S^r} - \frac{(\mathcal{M}_S^2)_{13}}{v_S^i} = 0. \tag{6.19}$$

Furthermore, we can find that $a_1^i = 0$ if $v_S^i = 0$ from Eq. (6.18), i.e., the explicit CPV must be associated with the spontaneous CPV, but not vice versa.

In this model and χ no longer behaves as a DM. As with the CPC CxSM, the degenerate scalar scenario is useful to obtain SM-like limits. Interactions between Higgs couplings to fermions (f) and gauge bosons ($V = W^\pm, Z$) are, respectively, given by

$$\mathcal{L}_{h_i\bar{f}f} = -\frac{m_f}{v}h\bar{f}f = -\frac{m_f}{v}\sum_{i=1-3}\kappa_{if}h_i\bar{f}f, \tag{6.20}$$

$$\mathcal{L}_{h_iVV} = \frac{1}{v}h\left(m_Z^2 Z_\mu Z^\mu + 2m_W^2 W_\mu^+ W^{-\mu}\right) = \frac{1}{v}\sum_{i=1-3}\kappa_{iV}h_i\left(m_Z^2 Z_\mu Z^\mu + 2m_W^2 W_\mu^+ W^{-\mu}\right), \tag{6.21}$$

where m_f and m_V are the same as those in the SM and Higgs coupling modifiers are

$$\kappa_{if} = O_{1i}, \quad \kappa_{iV} = O_{1i}. \tag{6.22}$$

Decay rates from h_i to the SM particle X is

$$\Gamma_{h_i\to XX} = O_{1i}^2\,\Gamma_{h_i\to XX}^{\rm SM}(m_{h_i}), \tag{6.23}$$

The sum of all processes by h_i is to be observed, i.e.,

$$\sum_{i=1-3}\Gamma_{h_i\to XX} \simeq \Gamma_{h\to XX}^{\rm SM}(m_h), \tag{6.24}$$

where the orthogonality of the mixing matrix (6.10) is used. Thus, the SM-like limit is achieved in the degenerate scalar scenario also in the CPV CxSM.

6.2 CPV effects on electroweak phase transition and gravitational waves

6.2.1 CPV effects on electroweak phase transition

EWPT pattern in the CPV CxSM is $\left(0, \tilde{v}_S^r(T), \tilde{v}_S^i(T)\right) \to \left(v(T), v_S^r(T), v_S^i(T)\right)$. To discuss the strong first-order EWPT qualitatively, as in Chapter. 5, we use the HT potential consisting of the tree-level potential and thermal masses which are $\mathcal{O}(T^2)$ term extracted from the finite temperature effective potential.

$$\begin{aligned} V^{\mathrm{HT}}\left(\varphi, \varphi_S^r, \varphi_S^i; T\right) =& V_0(\varphi, \varphi_S^r, \varphi_S^i) + \frac{T^2}{2}\left[\Sigma_H \varphi^2 + \Sigma_S \varphi_S^{r2} + \Sigma_S \varphi_S^{i2}\right] \\ =& \frac{m^2}{4}\varphi^2 + \frac{\lambda}{16}\varphi^4 + \frac{\delta_2}{8}\varphi^2\left(\varphi_S^{r2} + \varphi_S^{i2}\right) + \frac{d_2}{16}\left(\varphi_S^{r2} + \varphi_S^{i2}\right)^2 \\ &+ \sqrt{2}\left(a_1^r \varphi_S^r - a_1^i \varphi_S^i\right) + \frac{1}{4} b_1^r \left(\varphi_S^{r2} - \varphi_S^{i2}\right) + \frac{b_2}{4}\left(\varphi_S^{r2} + \varphi_S^{i2}\right) \\ &+ \frac{T^2}{2}\left[\Sigma_H \varphi^2 + \Sigma_S \varphi_S^{r2} + \Sigma_S \varphi_S^{i2}\right], \end{aligned} \tag{6.25}$$

where

$$\Sigma_H = \frac{\lambda}{8} + \frac{\delta_2}{24} + \frac{3}{16} g_2^2 + \frac{1}{16} g_1^2 + \frac{y_t^2}{4} + \frac{y_b^2}{4}, \tag{6.26}$$

$$\Sigma_S = \left(\delta_2 + d_2\right) \frac{1}{12}, \tag{6.27}$$

As indicated in the previous chapter, in the presence of an additional singlet field, the doublet-singlet mixing in the tree-level potential can contribute significantly to the first-order EWPT. In this context, we extend the analysis to the CPV CxSM case to investigate the extent to which CPV can influence the vigor of the first-order EWPT.

The three scalar fields are reexpressed in terms of the radial coordinates as

$$\varphi = z\cos\gamma, \quad \varphi_S^r = z\sin\gamma\cos\theta + \tilde{v}_S^r, \quad \varphi_S^i = z\sin\gamma\sin\theta + \tilde{v}_S^i, \tag{6.28}$$

where the limit of $z = 0$ describes to the symmetric phase. With those, the HT potential (6.25) takes the form

$$V(z, \gamma, \theta; T) = c_0 + c_1 z + \left(c_2 + c_2' T^2\right) z^2 - c_3 z^3 + c_4 z^4, \tag{6.29}$$

where

$$c_0 = \frac{b_2}{4}(\tilde{v}_S^{r2} + \tilde{v}_S^{i2}) + \frac{d_2}{16}(\tilde{v}_S^{r2} + \tilde{v}_S^{i2})^2 + \sqrt{2}(a_1^r \tilde{v}_S^r - a_1^i \tilde{v}_S^i) + \frac{b_1^r}{4}(\tilde{v}_S^{r2} - \tilde{v}_S^{i2}) + \frac{1}{2}\Sigma_S(\tilde{v}_S^{r2} + \tilde{v}_S^{i2})T^2 \quad (6.30)$$

$$c_1 = \left[\frac{b_2}{2}(\tilde{v}_S^r c_\theta + \tilde{v}_S^i s_\theta) + \frac{d_2}{4}(\tilde{v}_S^{r2} + \tilde{v}_S^{i2})(\tilde{v}_S^r c_\theta + \tilde{v}_S^i s_\theta)\right.$$
$$\left. + \sqrt{2}(a_1^r c_\theta - a_1^i s_\theta) + \frac{b_1^r}{2}(\tilde{v}_S^r c_\theta - \tilde{v}_S^i s_\theta) + \Sigma_S(\tilde{v}_S^r c_\theta + \tilde{v}_S^i s_\theta)T^2\right] s_\gamma \quad (6.31)$$

$$c_2 = \frac{m^2}{4}c_\gamma^2 + \frac{\delta_2}{8}(\tilde{v}_S^{r2} + \tilde{v}_S^{i2})c_\gamma^2 + \frac{b_2}{4}s_\gamma^2 + \frac{d_2}{8}\{2(\tilde{v}_S^r c_\theta + \tilde{v}_S^i s_\theta)^2 + (\tilde{v}_S^{r2} + \tilde{v}_S^{i2})\}s_\gamma^2 + \frac{b_1^r}{4}(c_\theta^2 - s_\theta^2)s_\gamma^2 \quad (6.32)$$

$$c_2' = \frac{1}{2}\Sigma_H c_\gamma^2 + \frac{1}{2}\Sigma_S s_\gamma^2 \quad (6.33)$$

$$c_3 = -\frac{s_\gamma}{4}(\tilde{v}_S^r c_\theta + \tilde{v}_S^i s_\theta)(\delta_2 c_\gamma^2 + d_2 s_\gamma^2) \quad (6.34)$$

$$c_4 = \frac{1}{16}(\lambda c_\gamma^4 + 2\delta_2 c_\gamma^2 s_\gamma^2 + d_2 s_\gamma^4) \quad (6.35)$$

At T_C, $V(z, \gamma, \theta; T_C)$ takes the form

$$V(z, \gamma, \theta; T_C) = c_4 z^2 (z - z_C)^2, \quad z_C = \frac{c_3}{2c_4}, \quad (6.36)$$

where the subscripts C indicate that the quantities are evaluated at T_C with $s_{\theta_C} = \sin\theta_C$, $c_{\theta_C} = \cos\theta_C$ and

$$t_{\gamma_C} = \frac{v_{SC}^r - \tilde{v}_{SC}^r}{v_C c_{\theta_C}} = \frac{v_{SC}^i - \tilde{v}_{SC}^i}{v_C s_{\theta_C}}. \quad (6.37)$$

For $t_{\gamma C} \ll 1$,T_C and v_C can be approximated as

$$v_C \simeq \sqrt{\frac{2\delta_2}{\lambda}\left(|\tilde{v}_{SC}|^2 - \tilde{v}_{SC}^i(\tilde{v}_{SC}^i - t_{\theta_C}\tilde{v}_{SC}^r)\right)\left(1 - \frac{v_{SC}^r}{\tilde{v}_{SC}^r}\right)}, \quad (6.38)$$

$$T_C \simeq \sqrt{\frac{1}{2\Sigma_H}\left[-m^2 - \frac{\delta_2}{2}|\tilde{v}_{SC}|^2\right]}, \quad (6.39)$$

where the first equality in Eq. (6.37) is used to obtain v_C. The second equality in Eq. (6.37) gives an equivalent expression of v_C, which is obtained by exchanging the indices r and i in Eq. (6.38).

A large δ_2 is required to satisfy the condition of the strong first-order EWPT $v_C/T_C \gtrsim 1$, as in the CPC case. From the first equality in Eq. (6.15), one obtains

$$\delta_2 = \frac{2}{vv_S^r}\sum_i O_{1i}O_{2i}m_{h_i}^2 = \frac{2c_2}{vv_S^r}\left[(m_{h_1}^2 - m_{h_2}^2)s_1 c_1 c_3 + s_2 s_3(m_{h_3}^2 - m_{h_1}^2 c_1^2 - m_{h_2}^2 s_1^2)\right]. \quad (6.40)$$

We have to take $v_S^{r,i}/v \lesssim 1$ GeV while maintaining $\delta_2 = \mathcal{O}(1)$ due to the orthogonality of the rotation matrix O, $\sum_i O_{1i}O_{2i} = 0$. As shown below, $v_S^r \lesssim 1$ GeV and $v_S^i \lesssim 1$ GeV are the typical sizes.

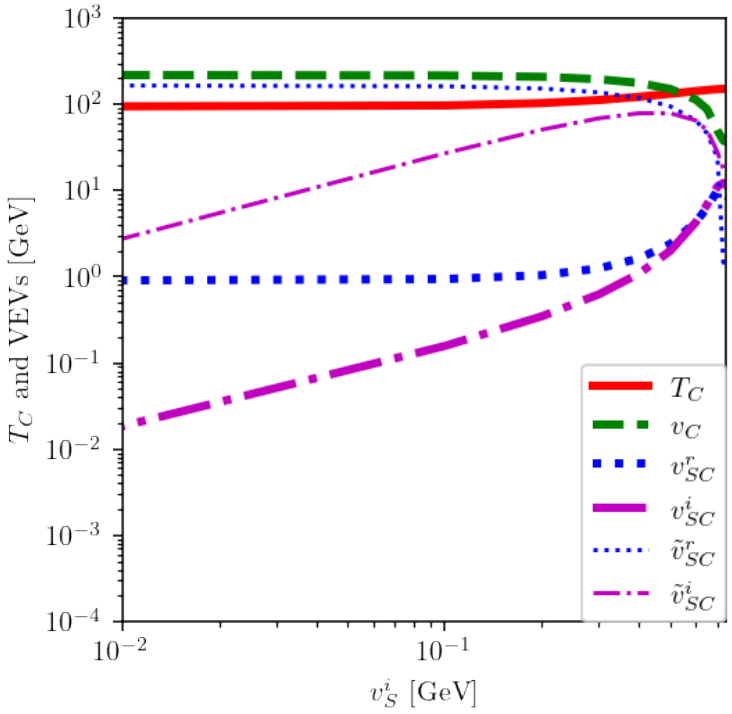

Figure 6.1: T_C and all VEVs in the symmetric and broken phases at T_C as functions of v_S^i. Shown here are T_C (solid, red), v_C (dashed, green), v_{SC}^r (thick-dotted, blue), $\tilde{v}_{SC}^r$ (thin-dotted, blue), v_{SC}^i (thick-dot-dashed, magenta), and $\tilde{v}_{SC}^i$ (thin-dot-dashed, magenta). The other input parameters other than v_S^i are listed in Table 6.1.

We now present our numerical findings, focusing on the strong first-order EWPT driven primarily by the tree-level structure. For the sake of illustration, we consider the Parwani scheme as outlined in [35].To analyze EWPT, we use a public code `CosmoTransitions` [69]. To evaluate the impact of CPV on the EWPT and make a comparison with the previously studied CPC case, we adopt parameter choices closely aligned with those in the aforementioned reference. Specifically, we set $v_S^r = 0.6$ GeV, $m_{h_2} = 124.0$ GeV, and $\alpha_1 = \pi/4$. In addition, we choose $m_{h_3} = 124.5$ GeV and $\alpha_2 = 0.0$ radians for illustration.

Fig. 6.1 shows all VEVs in the symmetric and broken phases at T_C as functions of v_S^i, where line and color schemes represent T_C (solid, red), v_C (dashed, green), v_{SC}^r (thick-dotted, blue), $\tilde{v}_{SC}^r$ (thin-dotted, blue), v_{SC}^i (thick-dot-dashed, magenta), and $\tilde{v}_{SC}^i$ (thin-dot-dashed, magenta), respectively. Although v_{SC}^i and $\tilde{v}_{SC}^i$ are monotonically increasing with respect to v_S^i, the relationship between them are reversed around $v_S^i \simeq 0.5$. This result implies that sizable CPV at T_C requires the sizable CPV at $T = 0$ GeV. In other words, the so-called *transitional CPV* [70, 71, 72, 73, 74], where CPV is large for T_C but is suppressed or zero for $T = 0$ GeV, does not occur in the present case.

We set Benchmark points so that the strong first-order EWPT occurs with reference to Fig. 6.1, which are summarized in Table 6.1. As can be seen from Fig. 6.2, the value of v/T becomes larger

Inputs	v [GeV]	v_S^r [GeV]	v_S^i [GeV]	m_{h_1} [GeV]	m_{h_2} [GeV]	m_{h_3} [GeV]	α_1 [rad]	α_2 [rad]
BP1	246.22	0.6	0.3	125.0	124.0	124.5	$\pi/4$	0.0
BP2	246.22	0.6	0.4	125.0	124.0	124.5	$\pi/4$	0.0
BP3	246.22	0.6	0.5	125.0	124.0	124.5	$\pi/4$	0.0
Outputs	m^2	b_2 [GeV^2]	b_1^r [GeV^2]	λ	δ_2	d_2	a_1^r [GeV^3]	a_1^i [GeV^3]
BP1	$-(124.5)^2$	$-(121.2)^2$	-7.717×10^{-12}	0.511	1.51	1.111	$-(18.735)^3$	$(14.870)^3$
BP2	$-(124.5)^2$	$-(107.3)^2$	5.145×10^{-12}	0.511	1.40	0.962	$-(18.735)^3$	$(16.367)^3$
BP3	$-(124.5)^2$	$-(90.82)^2$	0.0000	0.511	1.29	0.820	$-(18.735)^3$	$(17.630)^3$

Table 6.1: Input and output parameters in the three BPs. $\alpha_3 = 0.464, 0.588, 0.695$ radians in BP1, BP2, and BP3, respectively.

	CPV			CPC
	$v_S^i = 0.3$ GeV	$v_S^i = 0.4$ GeV	$v_S^i = 0.5$ GeV	$m_\chi = 62.5$ GeV
v_C/T_C	$\frac{196.1}{112.3} = 1.7$	$\frac{177.2}{122.5} = 1.4$	$\frac{150.9}{132.8} = 1.1$	$\frac{200.1}{106.1} = 1.9$
v_{SC}^r [GeV]	1.249	1.634	2.403	1.250
v_{SC}^i [GeV]	0.624	1.089	2.003	—
$\tilde{v}_{SC}^r$ [GeV]	137.9	118.5	94.82	144.2
$\tilde{v}_{SC}^i$ [GeV]	68.97	79.01	79.01	—

Table 6.2: VEVs at critical temperature T_C in the three BPs and the CPC case.

as v_S^i decreases, leading to $v_C/T_C < 1$ for $v_S^i \gtrsim 0.5$. When the CPC CxSM is used, the EWPT is much stronger[2]. The reduction of v_C/T_C is the consequence of the diminution of $\delta_2 \propto 1/v_S^i$, which can be understood by the analytic formulas Eqs.(6.38) and (6.39). On the other hand, T_N and the corresponding VEVs in the three BPs and CPC cases are summarized in Table 6.3. T_N is derived based on Eqs. (3.18) and (3.19) and here we employ the condition $S_3(T_N)/T_N = 140$. The stronger first-order EWPT leads to the larger supercooling, which may be characterized by the quantity $\Delta = (T_C - T_N)/T_C$. Too strong first-order EWPT, otherwise known as too large supercooling, prevents the bubble nucleation. In fact, v_S^i must be greater than 0.3 for bubble nucleation (See Fig. 6.3). Thus, v_S^i must be between 0.3 and 0.5 while keeping other parameter fixed.

6.2.2 CPV effects on gravitational waves

As a phenomenological consequence, gravitational waves (GWs) from the first-order EWPT can be evaluated. The amplitudes and frequencies of GWs would be modulated according to the amount of latent heat and/or duration of the phase transition. Those quantities may be quantified by the

[2]In the CPC case, only $m_\chi \simeq 62.5$ GeV is an allowed region, as discussed in Sec. 5

	CPV			CPC
	$v_S^i = 0.3$ GeV	$v_S^i = 0.4$ GeV	$v_S^i = 0.5$ GeV	$m_\chi = 62.5$ GeV
v_N/T_N	$\frac{239.0}{66.85} = 3.6$	$\frac{211.7}{102.0} = 2.1$	$\frac{177.2}{123.1} = 1.4$	$\frac{241.8}{57.20} = 4.2$
v_{SN}^r [GeV]	0.657	0.921	1.446	0.636
v_{SN}^i [GeV]	0.328	0.614	1.205	—
$\tilde{v}_{SN}^r$ [GeV]	143.7	122.3	97.26	150.1
$\tilde{v}_{SN}^i$ [GeV]	71.83	81.55	81.05	—
Δ	40.5%	16.7%	7.3%	46.0%

Table 6.3: VEVs at nucleation temperature T_N in the three BPs and the CPC case. $\Delta = (T_C - T_N)/T_C$, which characterizes the degrees of supercooling.

so-called α and β parameters [75, 76].

$$\alpha \equiv \frac{\epsilon\left(T_*\right)}{\rho_{\text{rad}}\ \left(T_*\right)}, \quad \beta \equiv H_* T_* \frac{d}{dT}\left(\frac{S_3(T)}{T}\right)\Big|_{T=T_*}, \tag{6.41}$$

with

$$\epsilon(T) = \Delta V_{\text{eff}} - T\frac{\partial \Delta V_{\text{eff}}}{\partial T}, \quad \rho_{\text{rad}}(T) = \frac{\pi^2}{30} g_*(T) T^4, \tag{6.42}$$

where $\Delta V_{\text{eff}} = V_{\text{eff}}\left(0, \tilde{v}_S^r(T), \tilde{v}_S^i(T); T\right) - V_{\text{eff}}\left(v(T), v_S^r(T), v_S^i(T); T\right)$ and $H_* = H\left(T_*\right)$. T_* is the temperature at which GWs are produced. In this study, we set $T_* = T_N$.

Sources of GWs arise from bubble collisions [77, 78, 79, 80, 81, 82], sound waves [83, 84, 85, 86] and turbulence induced by percolation [87, 88, 89, 90, 91, 92]. The GW spectrum we observe is the sum of them, i.e.,

$$\Omega_{\text{GW}}(f)h^2 = \Omega_{\text{col}}(f)h^2 + \Omega_{\text{sw}}(f)h^2 + \Omega_{\text{turb}}(f)h^2, \tag{6.43}$$

where f is the frequency of GW. We estimate Ω_{GW} using the following equations [75, 76]

$$\Omega_{\text{col}}h^2 = 1.67 \times 10^{-5}\left(\frac{\beta}{H_*}\right)^{-2}\left(\frac{\kappa_{\text{col}}\alpha}{1+\alpha}\right)^2\left(\frac{100}{g_*}\right)^{1/3}\left(\frac{0.11 v_w^3}{0.42 + v_w^2}\right)\frac{3.8\left(f/f_{\text{col}}\right)^{2.8}}{1 + 2.8\left(f/f_{\text{col}}\right)^{3.8}}, \tag{6.44}$$

$$\Omega_{\text{sw}}h^2 = 2.65 \times 10^{-6}\left(\frac{\beta}{H_*}\right)^{-1}\left(\frac{\kappa_v\alpha}{1+\alpha}\right)^2\left(\frac{100}{g_*}\right)^{1/3} v_w\left(\frac{f}{f_{\text{sw}}}\right)^3\left(\frac{7}{4 + 3\left(f/f_{\text{sw}}\right)^2}\right)^{7/2}, \tag{6.45}$$

$$\Omega_{\text{turb}}h^2 = 3.35 \times 10^{-4}\left(\frac{\beta}{H_*}\right)^{-1}\left(\frac{\kappa_{\text{turb}}\alpha}{1+\alpha}\right)^{\frac{3}{2}}\left(\frac{100}{g_*}\right)^{1/3} v_w \frac{\left(f/f_{\text{turb}}\right)^3}{\left[1 + \left(f/f_{\text{turb}}\right)\right]^{\frac{11}{3}}\left(1 + 8\pi f/h_*\right)}, \tag{6.46}$$

where v_w denotes the bubble wall velocity and h_* is

$$h_* = 1.65 \times 10^{-5}\left(\frac{T_*}{100\ \text{GeV}}\right)\left(\frac{g_*}{100}\right)^{1/6}\ \text{Hz}. \tag{6.47}$$

For $v_w \simeq 1$, one gets

$$\kappa_{\rm col} \simeq \frac{1}{1+0.715\alpha}\left(0.715\alpha + \frac{4}{27}\sqrt{\frac{3\alpha}{2}}\right), \tag{6.48}$$

$$\kappa_v \simeq \frac{\alpha}{0.73+0.083\sqrt{\alpha}+\alpha}, \tag{6.49}$$

$$\kappa_{\rm turb} \simeq (0.05-0.1)\kappa_v. \tag{6.50}$$

The peak frequencies of the three sources are, respectively, given by

$$f_{\rm col} = 16.5\times10^{-6}\left(\frac{\beta}{H_*}\right)\left(\frac{0.62}{1.8-0.1v_w+v_w^2}\right)\left(\frac{T_*}{100\ {\rm GeV}}\right)\left(\frac{g_*}{100}\right)^{1/6}\ {\rm Hz}, \tag{6.51}$$

$$f_{\rm sw} = 1.9\times10^{-5}\frac{1}{v_w}\left(\frac{\beta}{H_*}\right)\left(\frac{T_*}{100\ {\rm GeV}}\right)\left(\frac{g_*}{100}\right)^{1/6}\ {\rm Hz}, \tag{6.52}$$

$$f_{\rm turb} = 2.7\times10^{-5}v_w^{-1}\left(\frac{\beta}{H_*}\right)\left(\frac{T_*}{100\ {\rm GeV}}\right)\left(\frac{g_*}{100}\right)^{1/6}\ {\rm Hz}. \tag{6.53}$$

In our numerical analysis, we take $v_w = 0.95$ and $\kappa_{\rm turb} = 0.1\kappa_v$ for illustration. As can be seen from Eqs. (6.44), (6.45), and (6.46), $\Omega_{\rm GW}h^2$ becomes more enhanced as α increases and/or β decreases. Since the larger supercooling or the stronger first-order EWPT corresponds to the larger α, we can expect that $\Omega_{\rm GW}$ in BP1 or CPC cases becomes higher than in other cases. As numerically shown below, the sound wave contribution is dominant near the peak frequency. On the other hand, the other two contributions act at higher frequencies since $\Omega_{\rm sw} \propto f^{-4}$ while $\Omega_{\rm col} \propto f^{-1}$ and $\Omega_{\rm turb} \propto f^{-5/3}$ [76]. Thus, we include all the contributions in our calculation.

In Fig. 6.2, $\Omega_{\rm GW}h^2$ in the three BPs and CPC cases are shown. The line and color schemes are as follows: BP1 (thick-solid, red), BP2 (thick-dashed, blue), BP3 (thick-dotted, green) and CPC with $m_\chi = 62.5$ GeV (thin-solid, black). We also overlay the sensitivity curves of the future GW experiments such as TianQin [93, 94], Taiji [95, 96], LISA [76, 97, 98], DECIGO [99, 100], and BBO [101]. For BP1 and CPC, $\Omega_{\rm GW}h^2$ becomes as large as 10^{-11} near the peak frequency due to large supercooling, which can be probed by Taiji, LISA, DECIGO and BBO. On the other hand, at each peak frequency, we find that $\Omega_{\rm GW}h^2 \simeq 10^{-14}$ in BP2, which can be probed by only BBO and $\Omega_{\rm GW}h^2 \simeq 10^{-16}$ in BP3, which is still beyond the reach of the proposed experiments.

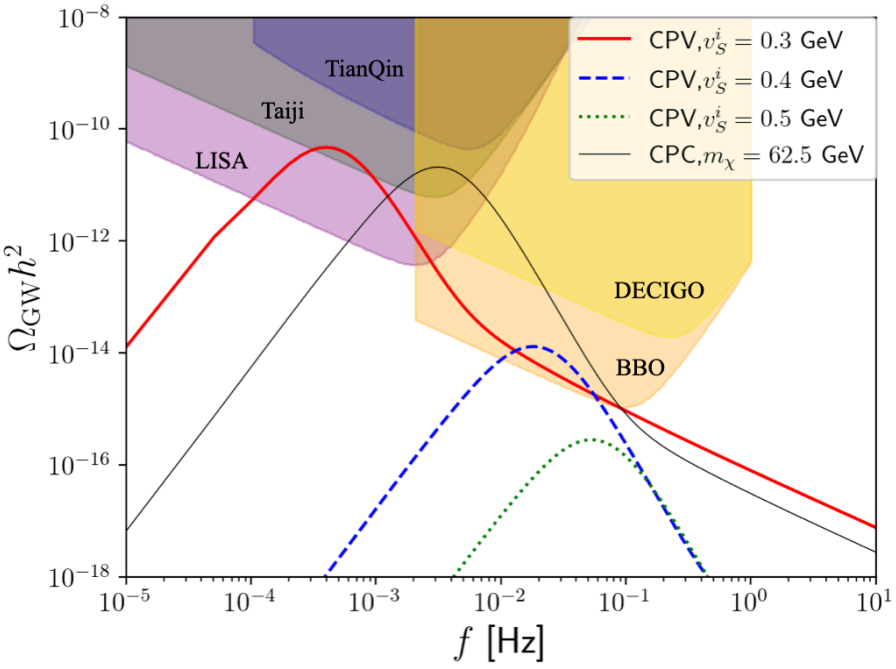

Figure 6.2: $\Omega_{\rm GW}h^2$ in the three BPs and CPC case are plotted as functions of f. The line and color schemes are as follows: BP1 (thick-solid, red), BP2 (thick-dashed, blue), BP3 (thick-dotted, green), CPC with $m_\chi = 62.5$ GeV (thin-solid, black). The sensitivity curves of the future GW experiments TianQin, Taiji, LISA, DECIGO, and BBO are also plotted.

6.3 Electron electric dipole moment and electroweak baryogenesis

6.3.1 Extension of CxSM with higher dimensional operators

The classical background fields are parameterized as

$$\langle H(x)\rangle = \frac{1}{\sqrt{2}}\begin{pmatrix} 0 \\ \rho(x) \end{pmatrix}, \quad \langle S(x)\rangle = \frac{1}{\sqrt{2}}\left(\rho_S^r(x) + i\rho_S^i(x)\right). \tag{6.54}$$

Since a spherically symmetric configuration is expected to give the least energy, the scalar fields depend only on the radial coordinate of the bubble $r = \sqrt{x^2+y^2+z^2}$. Then, we obtain the critical bubble using the following energy functional

$$S_3(T) = \int d^3x \left[(\partial_i H)^\dagger \partial_i H + \partial_i S^* \partial_i S + V_{\rm eff}(H, S; T)\right]. \tag{6.55}$$

In this case, the energy functional (6.55) takes the simplified form

$$S_3(T) = 4\pi \int_0^\infty dr\, r^2 \left[\frac{1}{2}\left(\frac{d\rho}{dr}\right)^2 + \frac{1}{2}\left(\frac{d\rho_S^r}{dr}\right)^2 + \frac{1}{2}\left(\frac{d\rho_S^i}{dr}\right)^2 + \bar{V}_{\rm eff}\left(\rho, \rho_S^r, \rho_S^i; T\right)\right], \tag{6.56}$$

where we normalize the potential as

$$\bar{V}_{\rm eff}\left(\rho,\rho_S^r,\rho_S^i;T\right)=V_{\rm eff}\left(\rho,\rho_S^r,\rho_S^i;T\right)-V_{\rm eff}\left(0,\tilde{v}_S^r,\tilde{v}_S^i;T\right). \tag{6.57}$$

From the energy functional (6.56), one finds the equations of motion (EOMs) of the scalar fields as

$$\frac{d^2\rho}{dr^2}+\frac{2}{r}\frac{d\rho}{dr}-\frac{\partial\bar{V}}{\partial\rho}=0, \tag{6.58}$$

$$\frac{d^2\rho_S^r}{dr^2}+\frac{2}{r}\frac{d\rho_S^r}{dr}-\frac{\partial\bar{V}}{\partial\rho_S^r}=0, \tag{6.59}$$

$$\frac{d^2\rho_S^i}{dr^2}+\frac{2}{r}\frac{d\rho_S^i}{dr}-\frac{\partial\bar{V}}{\partial\rho_S^i}=0. \tag{6.60}$$

For the critical bubble, the boundary conditions are

$$\lim_{r\to\infty}\rho(r)=0,\quad \lim_{r\to\infty}\rho_S^r(r)=\tilde{v}_S^r,\quad \lim_{r\to\infty}\rho_S^i(r)=\tilde{v}_S^i, \tag{6.61}$$

$$\left.\frac{d\rho(r)}{dr}\right|_{r=0}=0,\quad \left.\frac{d\rho_S^r(r)}{dr}\right|_{r=0}=0,\quad \left.\frac{d\rho_S^i(r)}{dr}\right|_{r=0}=0, \tag{6.62}$$

where the first boundary conditions (6.61) correspond to the symmetric phase ($r\to\infty$) and the second boundary conditions (6.62) are needed to avoid the singularities of EOMs at the broken phase ($r=0$).

T_N and bubble wall profile are the most important key parameters in generating BAU. Fig. 6.3 shows $\rho(r)$ (solid, red), $\rho_S^r(r)$ (dashed, blue), and $\rho_S^i(r)$ (dotted, green) in BP1 (left panel), BP2 (middle panel), and BP3 (right panel), respectively. The left endpoints correspond to the VEVs in the broken phase, while the right endpoints approach those in the symmetric phase. All the profiles have hyperbolic tangent shapes, but each BP has a different thicknesses of the walls (L_w) which gets smaller as the first-order EWPT becomes stronger. In Fig. 6.4, we also show the r dependence on the phase of the singlet scalar. Since ρ_S^i/ρ_S^r in all the BPs are constant, θ_S is not dynamical in our model at this time and the model must be extended to generate BAU.

The above numerical results for the phase are also explained qualitatively. Since S couples to fermions and gauge bosons only through the mixing angles α_i, a pseudoscalar coupling $h_i\bar{f}\gamma_5 f$ does not arise in this model. In other words, even though the complex phases exist in the scalar potential and the singlet scalar VEV, they do not induce CPV in the matter sector in the SM. Therefore, further extensions are needed to achieve EWBG and one possible extension is the addition of new fermions coupling to S. After integrating out the fermions, we consider the new Yukawa interactions by using higher dimensional operators contributing to the top quark and

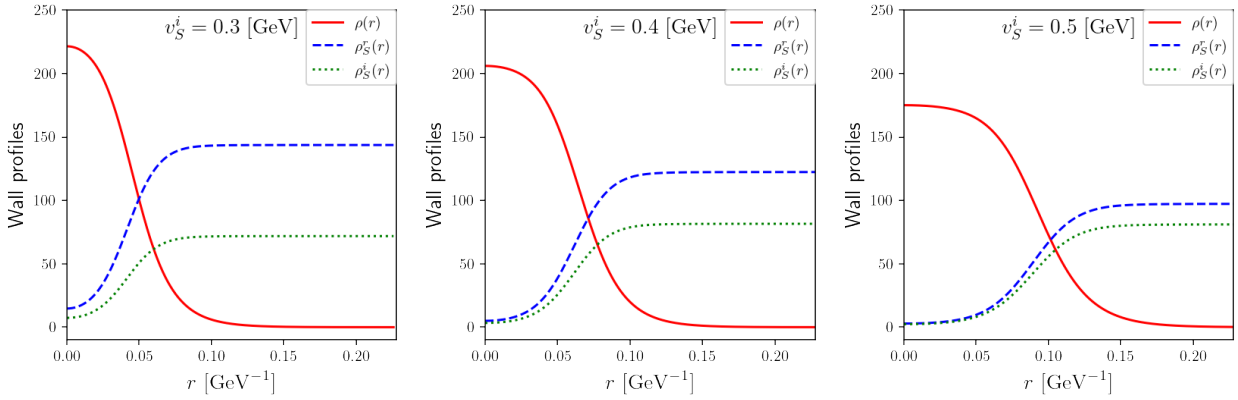

Figure 6.3: $\rho(r)$ (solid, red), $\rho_S^r(r)$ (dashed, blue), and $\rho_S^i(r)$ (dotted, green) in BP1 (left), BP2 (middle), BP3 (right).

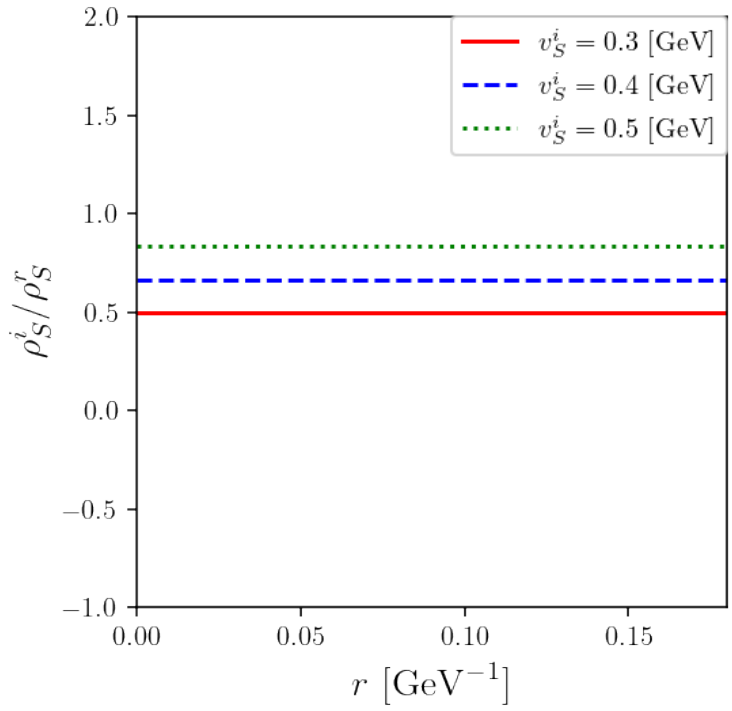

Figure 6.4: ρ_S^i/ρ_S^r as a function of r in BP1 (solid, red), BP2 (dashed, blue), and PB3 (dotted, green).

electron Yukawa coupling:

$$\begin{aligned}-\mathcal{L}_{h_i\bar{f}f} = \bar{q}_L\tilde{H}\left(y_t + \frac{c_{t,1}}{\Lambda}S + \frac{c_{t,2}}{\Lambda^2}|S|^2 + \frac{c_{t,3}}{\Lambda^2}S^2 + \cdots\right)t_R \\ + \bar{\ell}_L H\left(y_e + \frac{c_{e,1}}{\Lambda}S + \frac{c_{e,2}}{\Lambda^2}|S|^2 + \frac{c_{e,3}}{\Lambda^2}S^2 + \cdots\right)e_R \\ + \text{H.c},\end{aligned} \tag{6.63}$$

where q_L denotes the up-type left-handed quark doublet of the third generation, while ℓ_L is the down-type left-handed lepton doublet of the first generation. t_R and e_R are the right-handed top and electron, respectively. Λ is the scale of the integrated fermion i.e., a cutoff scale and $\tilde{H} = i\tau^2 H^*$ with τ^2 representing the second Pauli matrix. y_t and y_e are the top and electron Yukawa couplings in the SM, respectively, while $c_{t,i}$ and $c_{e,i}$ (i=1-3) are arbitrary complex parameters. Note that only the top phase is relevant here for EWBG. The imaginary parts of $c_{t,1}S$, $c_{t,2}$, and $c_{t,3}S^2$ contribute to the pseudoscalar coupling, potentially driving EWBG. The possibilities for EWBG using $\text{Im}(c_{t,1})$ or $\text{Im}(c_{t,2})$ in extensions of the SM with singlet scalar has been explored in studies such as refs. [102, 103, 65, 104]. On the other hand, the electron phase plays an important role in suppressing the electron EDM.

After this, we consider the dimension 5 operator in Eq. (6.63):

$$\begin{aligned}-\mathcal{L}^{\text{dim.5}}_{h_i\bar{f}f} \ni \bar{q}_L\tilde{H}\left(y_t + \frac{c_{t,1}}{\Lambda}S\right)t_R + \bar{\ell}_L H\left(y_e + \frac{c_{e,1}}{\Lambda}S\right)e_R \\ + \text{H.c.},\end{aligned} \tag{6.64}$$

Henceforth, $c_{t,1} = c_t$ and $c_{e,1} = c_e$. For later use, we parametrize $c_f = |c_f|e^{i\phi_f} = c_f^r + ic_f^i$, $f = t, e$. The top mass during EWPT is given by

$$m_t(r) = \frac{\rho(r)}{\sqrt{2}}\left(y_t + \frac{c_t}{\sqrt{2}\Lambda}\left(\rho_S^r(r) + i\rho_S^i(r)\right)\right) \equiv |m_t(r)|e^{i\theta_t(r)}, \tag{6.65}$$

where the phase $\theta_t(r)$ is expressed as

$$\theta_t(r) = \tan^{-1}\left(\frac{\rho_S^i(r)}{\sqrt{2}\Lambda y_t/c_{t,1} + \rho_S^r(r)}\right). \tag{6.66}$$

The CPV source term for BAU can arise from the derivatives of $\theta_t(r)$ with respect to r. Actually, in Fig. 6.5, we show the r dependence on the phase (6.66), where $|c_t| = y_t$ and $\Lambda = 1$ TeV. The graph shows that the phase, which was constant in Fig. 6.4, now varies with respect to r due to the introduction of the dimension 5 operator. Our primary interest is the case where the complex phase in the scalar potential is the only source for the CP violation that drives EWBG. Secondarily, to what extent complex c_t and c_e can change the former result. In what follows, we consider the 2 cases[3]:

[3]See App. E for specific physical CPV phases.

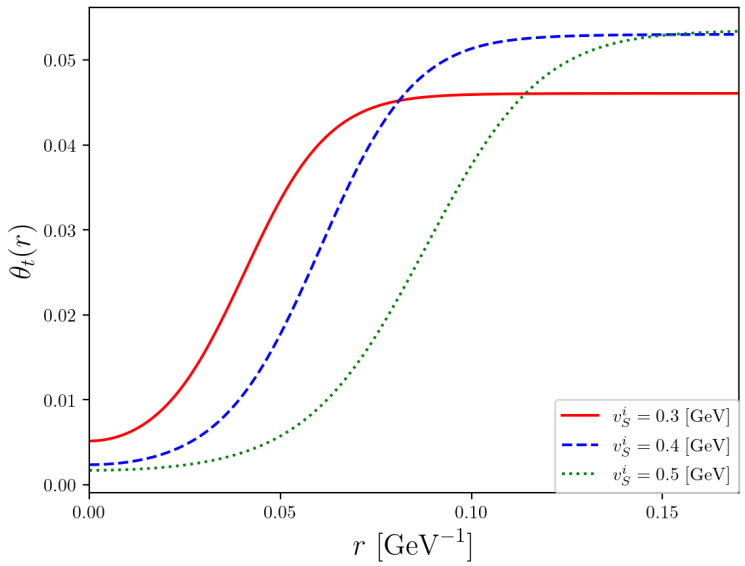

Figure 6.5: The phase (6.66) as a function of r in BP1 (solid, red), BP2 (dashed, blue), and PB3 (dotted, green). We set $|c_t| = y_t$ and $\Lambda = 1$ TeV as an example.

1. Both c_t and c_e are real

2. Both c_t and c_e are complex

6.3.2 Electron electric dipole moment

The electron EDM severely restrict the magnitude of CPV. The latest upper bounds on $|d_e|$ from the ACME and JILA experiments are, respectively, given by [105, 106]

$$|d_e^{\rm ACME}| < 1.1 \times 10^{-29}\ e\ \text{cm}\ (90\%\ \text{C.L.}), \tag{6.67}$$

$$|d_e^{\rm JILA}| < 4.1 \times 10^{-30}\ e\ \text{cm}\ (90\%\ \text{C.L.}). \tag{6.68}$$

In our model, dominant corrections to d_e come from the so-called Barr-Zee diagrams [107]. We decompose them into two parts

$$d_e = d_e^t + d_e^W, \tag{6.69}$$

where $d_e^t = (d_e^{h\gamma})_t + (d_e^{hZ})_t$ and $d_e^W = (d_e^{h\gamma})_W + (d_e^{hZ})_W$. The subscripts of the parentheses represent the particle running in the upper loop in the Barr-Zee diagrams, as showed in Fig. 6.6.

The top-loop contributions to $d_e^{h\gamma}$ in the degenerate mass limit becomes

$$\frac{(d_e^{h\gamma})_t}{e} \simeq \frac{\alpha_{\rm em}|c_t||c_e|\sin(\phi_e - \phi_t)v^2}{24\pi^3 m_t \Lambda^2}\Big[f(\tau_{th}) - g(\tau_{th})\Big], \tag{6.70}$$

where $\tau_{th} = m_t^2/m_h^2$ with $m_h \equiv m_{h_1} = m_{h_2} = m_{h_3}$, and $c_{t,e} = |c_{t,e}|e^{i\phi_{t,e}}$. $f(\tau_{th})$ and $g(\tau_{th})$, are the loop functions defined in Refs. [107].

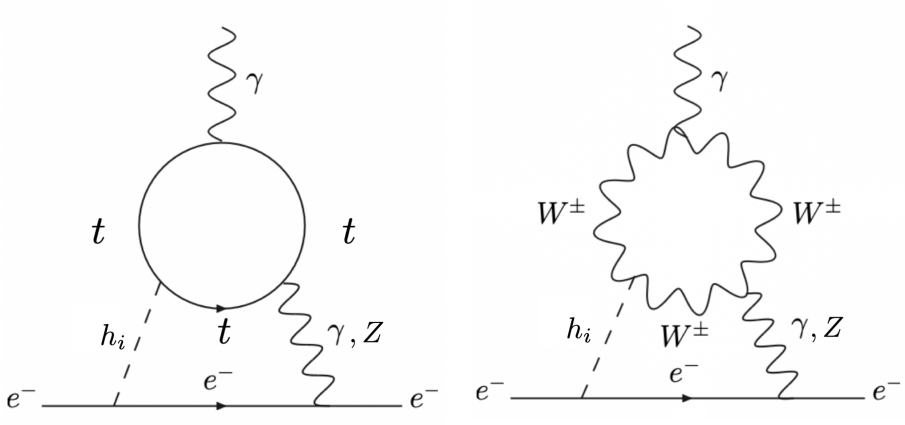

Figure 6.6: Dominant two-loop contributions to d_e in which electron phase enters. The left diagrams are denoted as $(d_e^{h\gamma})_t$ and $(d_e^{hZ})_t$, while the right ones as $(d_e^{h\gamma})_W$ and $(d_e^{hZ})_W$.

	d_e^t	d_e^W
Real c_t and c_e	$m_{h_i} = m_{h_j}$	$m_{h_i} = m_{h_j}$
Complex c_t and c_e	$m_{h_i} = m_{h_j}$ and $\phi_t = \phi_e \pm n\pi$	$m_{h_i} = m_{h_j}$

Table 6.4: Conditions for the vanishing electron EDM d_e.

The W-loop contributions to $d_e^{h\gamma}$ in the degenerate mass limit becomes

$$\frac{(d_e^{h\gamma})_W}{e} = -\sum_{i=1}^{3} \frac{\alpha_{\rm em}^2 v C_W^{h_i\gamma}}{32\pi^2 s_W^2 m_W^2} \mathcal{J}_W^{\gamma}(m_{h_i}), \tag{6.71}$$

where $\mathcal{J}_W^{\gamma}(m_{h_i})$ are the loop functions defined in [108], and it has the form

$$\begin{aligned} &\sum_{i=1}^{3} C_W^{h_i\gamma} \mathcal{J}_W^{\gamma}(m_{h_i}) \\ &= \frac{v c_e}{2\Lambda} \left(O_{12} O_{32} \Delta^{(21)} \mathcal{J}_W^{\gamma} + O_{13} O_{33} \Delta^{(31)} \mathcal{J}_W^{\gamma} \right), \end{aligned} \tag{6.72}$$

where $\Delta^{(ij)} \mathcal{J}_W^{\gamma} = \mathcal{J}_W^{\gamma}(m_{h_i}) - \mathcal{J}_W^{\gamma}(m_{h_j})$.

Therefore, As for the top-loop, from Eq. (6.70), we see that if c_t and c_e are real, $(d_e^{h\gamma})_t$ vanishes due to the Higgs mass degeneracy, while if c_t and c_e are complex, further phase alignment $\phi_t = \phi_e + n\pi$ is needed to suppress $(d_e^{h\gamma})_t$. On the other hand, as for the W-loop, regardless of c_e, $(d_e^{h\gamma})_W$ vanishes when $m_{h_1} = m_{h_2} = m_{h_3}$. Similarly, we can obtain the same vanishing conditions for $(d_e^{hZ})_t$ and $(d_e^{hZ})_W$. The conditions for the vanishing d_e^t and d_e^W are summarized in Table 6.4.

Inputs	v [GeV]	v_S^r [GeV]	v_S^i [GeV]	m_{h_1} [GeV]	m_{h_2} [GeV]	m_{h_3} [GeV]	α_1 [rad]	α_2 [rad]
	246.22	0.6	-0.3	125.0	124.0	124.5	$\pi/4$	0.0
Outputs	m^2	b_2 [GeV^2]	b_1 [GeV^2]	λ	δ_2	d_2	a_1^r [GeV^3]	a_1^i [GeV^3]
	$-(124.5)^2$	$-(121.2)^2$	-7.717×10^{-12}	0.511	1.51	1.111	$-(18.735)^3$	$-(14.870)^3$

Table 6.5: Inputs and outputs in our benchmark. In this case, $\alpha_3 = 0.464$ radians, and the Higgs coupling modifiers are $\kappa_1 = 0.711$, $\kappa_2 = -0.711$, and $\kappa_3 = 0.0$.

6.3.3 Numerical results

With respect to the generated baryon number, we follow the work of refs. [40, 41, 42] which derives the semiclassical force in the presence of the CP violation. The specific calculation method is as described in Sec. 3.2.3. In our case, the top mass during EWPT and its phase are given by Eqs. (6.65) and (6.66).

After solving transport equations, one can find the baryon-to-photon ratio (η_B) as [42]

$$\eta_B = \frac{405\Gamma_{\rm sph}^{\rm sym}}{4\pi^2\gamma_w v_w g_*(T)T}\int_0^\infty dz\ \mu_{B_L}\exp\left(-\frac{45\Gamma_{\rm sph}^{\rm sym}z}{4\gamma_w v_w}\right), \tag{6.73}$$

where μ_{B_L} represents a chemical potential for the left-handed baryon number, $g_*(T)(=108.75)$ is the degrees of freedom of the relativistic particles in the thermal bath, $\Gamma_{\rm sph}^{\rm sym}(=1.0\times10^{-6}T$ [42]) is the sphaleron rate in the symmetric phase, $v_w(=0.1)$ is the wall velocity, and $\gamma_w = 1/\sqrt{1-v_w^2}$. We set T to a nucleation temperature T_N. Using Eq. (6.73), we estimate η_B and compare with the observed values, $\eta_B^{\rm BBN} = (5.8-6.5)\times10^{-10}$ at 95% CL from bigbang nucleosynthesis and $\eta_B^{\rm CMB} = (6.105\pm0.055)\times10^{-10}$ at 95% CL from comic microwave background [109].

To see the behavior of the suppression numerically, a typical example is given here. The input and output parameters are summarized in Table 6.5. As studied in Sec. 6.2.1, $0.3 \lesssim v_S^i \lesssim 0.5$ is the range where the first-order EWPT is strong enough and bubble nucleates. We take a parameter set BP1 in Table. 5.1 for illustrative purposes but with the sign of v_S^i being flipped. Regarding c_f $(f = t, e)$, we set $|c_f| = y_f$ and take ϕ_f as the free parameters.

Fig. 6.7 shows $|d_e|$ (green solid line) and its details $|d_e^t|$ (blue dotted line) and $|d_e^W|$ (orange dashed line) as a function of m_{h_2} with $|c_t| = y_t$, $|c_e| = y_e$, $\phi_t = \phi_e = 0$, and $\Lambda = 1.0$ TeV. The upper dotted horizontal line represents the experimental bound of ACME, while the lower one represents the JILA bound, above which regions are excluded. As can be seen from this graph, when m_{h_2} approaches 125 GeV$(= m_{h_1})$ the large dip is provided, evading ACME and JILA constraints. This clearly shows that the degenerate scalar scenario provides an exquisite parameter space that simultaneously fits LHC and electronic EDM data.

As shown in Fig. 6.6, the top-loop and the W-loop contributions have opposite signs, so these cancellations suppress electron EDM to some extent. In adition, in the case of $\phi_t = \phi_e = 0$, CP violation solely comes from the scalar potential. With this CP violation, we calculate the BAU

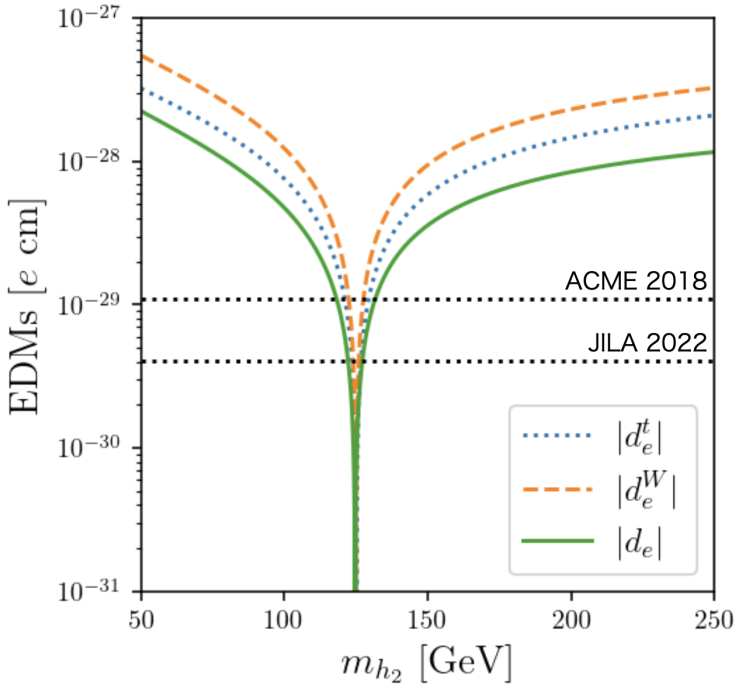

Figure 6.7: The electron EDM as a function of m_{h_2} in the case that $|c_t| = y_t$, $|c_e| = y_e$, $\phi_t = \phi_e = 0$, and $\Lambda = 1.0$ TeV. We take the parameter set given in Table 6.5 while m_{h_2} is the free parameter. Here, d_e^t and d_e^W are the two-loop and the W-loop contributions to the electron EDM, depicted as the left and right diagrams in Fig. 6.6, respectively.

in the cases of $\Lambda = 1.0$, 1.5, and 2.0 TeV, respectively. The results are summarized in Table 6.6. One can see that the $\Lambda = 1.0$ TeV case provides $\eta_B = \mathcal{O}(10^{-10})$, while the other two cases provide the smaller η_B to some extent. Thus, the case in which CP violation arises only from the scalar potential seems to give the sufficient baryon asymmetry.

Next, we discuss the case of complex c_t and c_e. In this case, v_S^i and c_t gives the CP-violation responsible for EWBG. Fig. 6.8 shows η_B and $|d_e|$ in the (ϕ_t, ϕ_e) plane. The red line represents the JILA's bound. Small spaces between close red lines are allowed. This graph insists that in addition to mass degeneracy of the Higgs boson, top and electron phases must coincide. The vertical dotted lines denotes $\eta_B = 2.62 \times 10^{-10}$, 2.59×10^{-10}, 2.01×10^{-10}, 1.83×10^{-11}, -8.19×10^{-11}, and -2.42×10^{-10} for $\phi_t = -\pi/2$, $-\pi/4$, $-\pi/8$, $\pi/8$, $\pi/4$, and $\pi/2$, from left to right, respectively. In this benchmark point, $\phi_t = -\pi/2$ gives the largest BAU with the correct sign. This demonstration reveals that the parameter space for successful EWBG is still wide open in light of the JILA data.

	$\eta_B/10^{-10}$	$\lvert d_e\rvert/10^{-30}$	$d_e^t/10^{-30}$	$d_e^W/10^{-30}$
$\Lambda = 1.0$ [TeV]	1.16	1.15	3.14	-4.29
$\Lambda = 1.5$ [TeV]	0.797	0.77	2.09	-2.86
$\Lambda = 2.0$ [TeV]	0.606	0.57	1.57	-2.15

Table 6.6: η_B and $|d_e|$ in the case of $|c_t| = y_t$, $|c_e| = y_e$, and $\phi_t = \phi_e = 0$. The electron EDM is given in units of e cm.

6.4 Summary of Chapter 6

FIrst, we have investigated the possibility of a strong first-order EWPT taking CPV into account in the CxSM with degenerate scalars. To qualitatively understand the impact of CP violation on the first-order EWPT, we derived analytical expressions for v_C and T_C using simplified effective potentials. As is the CPC case, v_C/T_C can be enhanced by the doublet-singlet Higgs mixing coupling δ_2, which is realized by small v_S^r, v_S^i. This behavior was confirmed through numerical analysis employing the 1-loop effective potential with the Parwani resummation scheme (Fig. 6.1).

The critical temperature and bubble wall profiles were also evaluated, and these results were used to estimate the gravitational waves. Since GWs are modulated by the strength of the first-order EWPT, the GWs spectrum cannot be detected if the CPV of the singlet scalar is large. However, we can conclude that it is observable by future experiments in BP1 and BP2. Thus, even though the GWs are not the CPV observable, we may get some useful information about CPV in the CxSM. Besides the GWs probes, degenerate scalars may be distinguished by a recoil mass technique at future lepton colliders [46].

Next, we also have studied the possibility of EWBG in the CxSM. Since the singlet scalar couples to the SM fermions only through the mixing angles α, a pseudoscalar coupling does not arise in this model at current stage. Therefore, even though the complex phases exist in the singlet scalar VEV, we do not induce CPV in the matter sector in the SM. We have considered the new Yukawa interactions by using the following dimension-5 operators contributing to the top quark and electron Yukawa coupling. Two cases are addressed: one is the case in which CP violation arises only from the scalar potential, and the other is the case where the coefficient of the dimension-5 Yukawa interaction additionally yields CP violation. It is found that sufficient baryon asymmetry was found to be generated even when the CPV phase is derived only from the imaginary part of the singlet scalar. The EWPT and BAU perturbation calculations used here include theoretical uncertainties, so a more detailed analysis is left for future research.

We have also studied the electron EDM in the above two cases. In the real c_t and c_e cases, the Higgs mass degeneracy suppresses the electron EDM and avoids the ACME and JILA constraints. On the other hand, in the case of complex c_t and c_e, an additional phase alignment $\phi_t = \phi_e + n\pi$

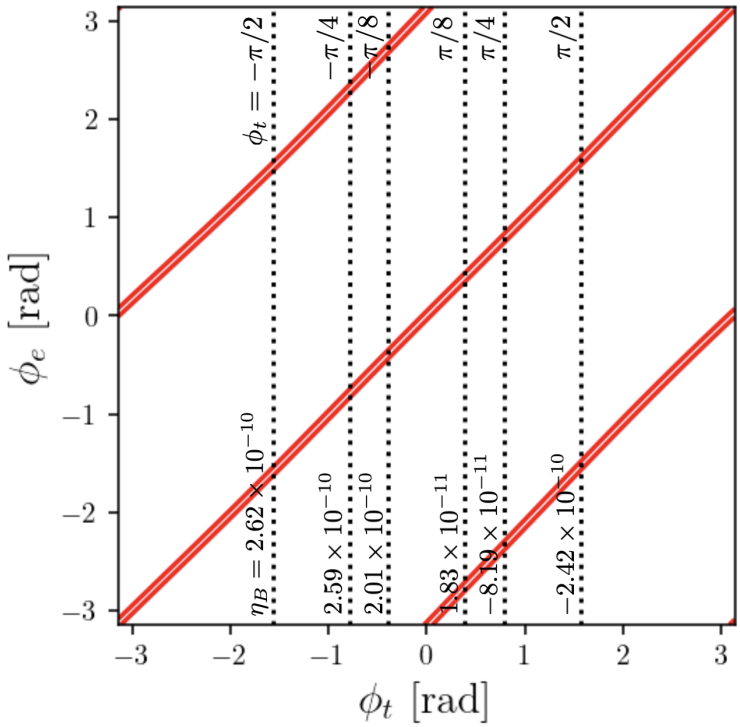

Figure 6.8: η_B and $|d_e|$ are shown, where $\Lambda = 1.0$ TeV, $|c_t| = y_t$, and $|c_e| = y_e$ are taken. The red line represents the JILA's bound and small spaces between close red lines are allowed.

is required to be consistent with the experimental bounds. In conclusion, the parameter space of EWBG in our scenario is still wide open after the recent EDM update.

Chapter 7

Grand Summary

This chapter summarize the entire thesis. Chapter 2 have provided an overview of the SM. Starting with the elementary particles that make up the SM, I have described the Higgs mechanism, which is closely related to EWBG, and the associated mass gain process of gauge bosons and fermions. I have also mentioned the CKM matrix that gives CPV phase in the SM.

In Chapter 3, I have discussed one of the outstanding issues, BAU. The baryon-to-photon ratio η_B has been measured by some cosmological observations, and the correct explanation of this value is baryogenesis. There are various baryogenesis scenario, but here we focus on the most testable scenario, EWBG, and described sphaleron process and strong first-order EWPT with bubble nucleation that is necessary to satisfy the Sakharov's conditions. In addition, several calculation schemes for effective potentials, which are essential for the evaluation of EWPT, were presented. In order to derive the generated baryon number, the WKB method for top transport scenario is introduced here. In Chapter 4, I have discussed DM, specifically WIMP. Expressions for DM relic density and DM-nucleon scattering cross section were derived for comparison with observations/experiments.

From Chapter 5, I have described the details of our study. First, I have focused on the CP-conserving CxSM. There are two Higgs bosons and one scalar DM in this model, and the DM and quark scattering can be suppressed due to the degenerate scalar scenario. It must be emphasized here that the core of the cancellation mechanism in the degenerate scalar scenario is the suppression of δ_2 owing to the Higgs mass degeneracy with moderate values of v_S. In the CxSM, the structure of the tree-level potential, especially the $\mathrm{SU}(2)_L$ doublet-singlet mixing δ_2, makes an important contribution to first-order EWPT. Therefore, the conditions for strong first-order EWPT is incompatible with the suppression mechanism of the degenerate scalar scenario, but the allowed region still exists at $m_\chi = 62.5$ GeV. In the area there, the above two were found to be compatible. We also have examined the constraints that the degenerate scalar scenario imposes on the tree-level potential, and the possibility that the MPP predicts a degenerate Higgs. As

a result, the degenerate scalar scenario does not hold for the most general potential because it constrains the $SU(2)_L$ doublet-singlet mixing. Furthermore, although the MPP does not force the degenerate scalars, it implies a small region where both the degenerate scalar scenario and EWPT are possible.

The next CP-violating CxSM study is presented in Chapter 6. In this case, there are three Higgs bosons, and the imaginary part of S is an ordinary decaying particle. The CPV phase is sensitive to the strength of the EWPT; the larger CPV derives the weaker first-order EWPT. On the other hand, too strong first-order EWPT prevents bubble nucleation. As a result, $0.3 \lesssim v_S^i \lesssim 0.5$ is preferred. We also have estimated GW generated by EWPT. The amplitude of the predicted GW becomes larger as first-order EWPT is stronger, i.e., smaller v_S^i produces more observable GWs. Finally, new Yukawa interactions of top quark and electron involving higher dimensional operators was introduced to convey the CPV phase of the singlet to the SM sector. In this study, we focus on the dimension-5 operators. The electron EDM is currently the most sensitive to CPV, and mass degeneracy of the Higgs bosons is most important to suppress the contribution to the electron EDM. It was also found that even when CPV involved in EWBG comes only from the singlet phase, the generated baryon numbers are consistent with the observed values.

Appendix A

Derivation of effective potential

In this chapter, effective potential at zero and finite temperature is derived according to ref. [110].

A.1 Effective potential at zero temperature

A.1.1 Generating functional

The relation between the action function $S[\phi]$ and the Lagrangian density $\mathcal{L}\{\phi(x)\}$ with respect to the field ϕ is defined as

$$S[\phi] = \int d^4x \mathcal{L}\{\phi(x)\}. \tag{A.1}$$

The generating functional is given by the path-integral representation as follows:

$$Z[J] = \langle 0_{\text{out}} \mid 0_{\text{in}} \rangle \simeq \int \mathcal{D}\phi \exp[i(S + J\phi)], \tag{A.2}$$

$$J\phi \equiv \int d^4x J(x)\phi(x). \tag{A.3}$$

The nth derivative of $Z[J]$ with respect to J is the nth-order Green ' s function $G^{(n)}$

$$G^{(n)} \equiv \frac{\delta^{(n)} Z[J]}{\delta J^{(n)}}. \tag{A.4}$$

However, the Green's functions obtained in this way are disconnected and contain components that do not contribute to the physical process. We introduce the connected generating functional $W[J]$ as a prescription for dropping the disconnected components and extracting only the connected parts such that

$$Z[J] = e^{iW[J]}. \tag{A.5}$$

The effective action $\Gamma[\phi]$ is defined as the Legendre transform of (A.5)

$$\Gamma[\bar{\phi}] = W[J] - \int d^4x J(x)\bar{\phi}(x), \tag{A.6}$$

where

$$\bar{\phi}(x) \equiv \frac{\delta W(J)}{\delta J(x)}. \tag{A.7}$$

From (A.6) and (A.7), we can obtain

$$\begin{aligned}
\frac{\delta\Gamma[\bar{\phi}]}{\delta\bar{\phi}(x)} &= \frac{\delta}{\delta\bar{\phi}(x)}\left[W[J] - \int d^4y J(y)\bar{\phi}(y)\right] \\
&= \int d^4z \frac{\delta W[J]}{\delta J(z)}\frac{\delta J(z)}{\delta\bar{\phi}(x)} - \frac{\delta}{\delta\bar{\phi}(x)}\int d^4y J(y)\bar{\phi}(y) \\
&= \int d^4z \frac{\delta W[J]}{\delta J(z)}\frac{\delta J(z)}{\delta\bar{\phi}(x)} - \int d^4y \left\{\frac{\delta\bar{\phi}(y)}{\delta\bar{\phi}(x)}J(y) + \bar{\phi}(y)\frac{\delta J(y)}{\delta\bar{\phi}(x)}\right\} \\
&= \int d^4z \frac{\delta W[J]}{\delta J(z)}\frac{\delta J(z)}{\delta\bar{\phi}(x)} - \int d^4y \left\{\frac{\delta\bar{\phi}(y)}{\delta\bar{\phi}(x)}J(y) + \frac{\delta W[J]}{\delta J(y)}\frac{\delta J(y)}{\delta\bar{\phi}(x)}\right\} \\
&= \int d^4z \frac{\delta W[J]}{\delta J(z)}\frac{\delta J(z)}{\delta\bar{\phi}(x)} - \int d^4y \left\{\delta(y-x)J(y) + \frac{\delta W[J]}{\delta J(y)}\frac{\delta J(y)}{\delta\bar{\phi}(x)}\right\} \\
&= -J(x).
\end{aligned} \tag{A.8}$$

Here, from (A.8)

$$\left.\frac{\delta\Gamma[\bar{\phi}]}{\delta\bar{\phi}(x)}\right|_{j=0} = 0, \tag{A.9}$$

is given and this defines the vacuum state of the theory in the absence of an external source. As mentioned earlier, the Green's function is given as the derivative of the generating functional with respect to source. Therefore, suppose that $Z[J]$ and $W[J]$ can be expanded at source J as follows:

$$Z[J] = \sum_n \frac{i^n}{n!}\int d^4x_1 \cdots d^4x_n J(x_1)\cdots J(x_n)\, G^{(n)}(x_1\cdots x_n), \tag{A.10}$$

$$iW[J] = \sum_n \frac{i^n}{n!}\int d^4x_1 \cdots d^4x_n J(x_1)\cdots J(x_n)\, G_c^{(n)}(x_1\cdots x_n). \tag{A.11}$$

Since the effective action is a functional of $\bar{\phi}$, it is expressed as

$$\Gamma[\bar{\phi}] = \sum_n \frac{i^n}{n!}\int d^4x_1 \cdots d^4x_n \bar{\phi}(x_1)\cdots\bar{\phi}(x_n)\,\Gamma^{(n)}(x_1\cdots x_n), \tag{A.12}$$

where $\Gamma^{(n)}(x_1\cdots x_n)$ is defined as the one-particle irreducible (1PI) Green functions. 1PI means that one propagation function cannot be disconnected and separated into two or more. Since the interaction vertex is given by the momentum space representation of the remainder of the Lagrangian minus the field, the effective vertex is also considered to be given by the momentum space representation of $\Gamma^{(n)}(x_1\cdots x_n)$, which is the remainder of the effective action minus the field.

A.1.2 Definition of effective potential

The relationship between the effective potential and the effective action is given by using the constant field ϕ_c as follows:

$$\Gamma\left[\phi_c\right] = -\int d^4x V_{\text{eff}}\left(\phi_c\right), \tag{A.13}$$

and justify this relationship below. In one dimension, the Fourier transformation of the function $f(x)$ in coordinate space into momentum space is

$$\tilde{f}(p) = \int dx e^{-ipx} f(x), \tag{A.14}$$

$$f(x) = \int \frac{dp}{2\pi} e^{ipx} \tilde{f}(p). \tag{A.15}$$

The Fourier transformations of the 1PI Green's functions $\Gamma^{(n)}(x)$ and $\bar{\phi}$ are given by

$$\Gamma^{(n)}\left(x_1, \cdots, x_n\right) = \int \prod_i \frac{d^4p_i}{(2\pi)^4} e^{ip_i x_i} (2\pi)^4 \delta^{(4)}\left(p_1 + \cdots + p_n\right) \Gamma^{(n)}\left(p_1, \cdots, p_n\right), \tag{A.16}$$

$$\bar{\phi}(p) = \int d^4x e^{-ipx} \bar{\phi}(x). \tag{A.17}$$

By using the effective action of the momentum space $\Gamma^{(n)}(p)$, Eq. (A.12) can be expressed as

$$\begin{aligned}
\Gamma[\bar{\phi}] =& \sum_n \frac{1}{n!} \int d^4x_1 \cdots d^4x_n \bar{\phi}\left(x_1\right) \cdots \bar{\phi}\left(x_n\right) \Gamma^{(n)}\left(x_1, \cdots, x_n\right) \\
=& \sum_n \frac{1}{n!} \int d^4x_1 \cdots d^4x_n \bar{\phi}\left(x_1\right) \cdots \bar{\phi}\left(x_n\right) \\
& \times \int \prod_i \left[\frac{d^4p_i}{(2\pi)^4} e^{ip_i x_i}\right] (2\pi)^4 \delta^{(4)}\left(p_1 + \cdots + p_n\right) \Gamma^{(n)}\left(p_1, \cdots, p_n\right) \\
=& \sum_n \frac{1}{n!} \int d^4x_1 \cdots d^4x_n e^{-i(-p_1)x_1} \cdots e^{-i(-p_n)x_n} \bar{\phi}\left(x_1\right) \cdots \bar{\phi}\left(x_n\right) \\
=& \times \int \frac{d^4p_1}{(2\pi)^4} \cdots \frac{d^4p_n}{(2\pi)^4} (2\pi)^4 \delta^{(4)}\left(p_1 + \cdots + p_n\right) \Gamma^{(n)}\left(p_1, \cdots, p_n\right) \\
=& \sum_n \frac{1}{n!} \int \frac{d^4p_1}{(2\pi)^4} \cdots \frac{d^4p_n}{(2\pi)^4} \tilde{\phi}\left(-p_1\right) \cdots \phi\left(-p_n\right) \\
& \times (2\pi)^4 \delta^{(4)}\left(p_1 + \cdots + p_n\right) \Gamma^{(n)}\left(p_1, \cdots, p_n\right),
\end{aligned} \tag{A.18}$$

where

$$\delta^{(4)}(p) = \int \frac{d^4x}{(2\pi)^4} e^{-ipx}. \tag{A.19}$$

On the other hand, by using the following relationship

$$\bar{\phi}(p) = \int d^4x e^{-ipx} \phi_c = (2\pi)^4 \delta^{(4)}(p) \phi_c, \tag{A.20}$$

we can obtain

$$\begin{aligned}
\Gamma(\phi_c) =& \sum_n \frac{1}{n!} \int \frac{d^4p_1}{(2\pi)^4} \cdots \frac{d^4p_n}{(2\pi)^4} \bar{\phi}(-p_1) \cdots \bar{\phi}(-p_n) \\
& \times (2\pi)^4 \delta^{(4)}(p_1 + \cdots + p_n) \Gamma^{(n)}(p_1, \cdots, p_n) \\
=& \sum_n \frac{1}{n!} \int \frac{d^4p_1}{(2\pi)^4} \cdots \frac{d^4p_n}{(2\pi)^4} (2\pi)^4 \delta^{(4)}(-p_1) \phi_c \cdots (2\pi)^4 \delta^{(4)}(-p_n) \phi_c \\
& \times (2\pi)^4 \delta^{(4)}(p_1 + \cdots + p_n) \Gamma^{(n)}(p_1, \cdots, p_n) \\
=& \sum_n \frac{1}{n!} \phi_c^n (2\pi)^4 \delta^{(4)}(0) \Gamma^{(n)}(p_i = 0) \\
=& \sum_n \frac{1}{n!} \phi_c^n \int d^4x e^{-i\cdot 0 \cdot x} \Gamma^{(n)}(p_i = 0) \\
=& \sum_n \frac{1}{n!} \phi_c^n \int d^4x \Gamma^{(n)}(p_i = 0) .
\end{aligned} \tag{A.21}$$

Comparing (A.13) and (A.21), one finds

$$V_{\text{eff}} = -\sum_n \frac{1}{n!} \phi_c^n \Gamma^{(n)}(p_i = 0) . \tag{A.22}$$

In other words, the effective potential is the 1PI Green's function in momentum space with the momentum of the external line set to zero multiplied by an n constant field ϕ_c.

Another method of evaluating the effective potential will also be presented. Substituting (A.2) and (A.5) for (A.6), one gets

$$\Gamma[\bar{\phi}] = -i\hbar \ln \int \mathcal{D}\phi \exp \frac{i}{\hbar} [S + J(\phi - \bar{\phi})]. \tag{A.23}$$

Changing the integrating variable ϕ to $\phi + \bar{\phi}$ and substituting (A.8) yields

$$\Gamma[\bar{\phi}] = -i\hbar \ln \int \mathcal{D}\phi \exp \frac{i}{\hbar} \int d^4x \left[\mathcal{L}(\phi + \bar{\phi}) - \frac{\delta \Gamma[\bar{\phi}]}{\delta \bar{\phi}} \phi \right] . \tag{A.24}$$

Expand $\mathcal{L}(\phi + \bar{\phi})$ around the constant field $\bar{\phi}$ for $\phi_i(x)$:

$$\mathcal{L}(\phi + \bar{\phi}) = \mathcal{L}(\bar{\phi}) + \frac{\partial \mathcal{L}(\bar{\phi})}{\partial \bar{\phi}_i} \phi_i + \frac{1}{2} \phi_i i \left[D_F^{-1}(\bar{\phi}) \right]^{ij} \phi_j + \cdots , \tag{A.25}$$

where

$$i \left[D_F^{-1}(\bar{\phi}) \right]^{ij} = \left. \frac{\partial^2 \mathcal{L}(\phi + \bar{\phi})}{\partial \phi_i \partial \phi_j} \right|_{\phi = 0} = \frac{\partial^2 \mathcal{L}(\bar{\phi})}{\partial \bar{\phi}_i \partial \bar{\phi}_j}, \tag{A.26}$$

is the inverse of the propagator in a vacuum such that the expectation value of the field is $\bar{\phi}$. Substituting (A.25) for (A.24), we get

$$\Gamma[\bar{\phi}] = \int d^4x \mathcal{L}(\bar{\phi}) + \tilde{\Gamma}[\bar{\phi}], \tag{A.27}$$

where

$$\tilde{\Gamma}[\bar{\phi}] = -i\hbar \ln \int \mathcal{D}\phi \exp \frac{i}{\hbar} \int d^4x \left[\frac{1}{2}\phi i D_F^{-1}(\bar{\phi})\phi + \cdots - \frac{\delta \tilde{\Gamma}[\bar{\phi}]}{\delta \bar{\phi}}\phi \right]. \tag{A.28}$$

The first term in (A.27) is the classical action integral and the second term is the contribution of the 1PI loop graph. Then using the Gaussian integral formula

$$\int \mathcal{D}\phi \exp \left[-i \int d^4x d^4y \frac{1}{2}\phi(x) A(x,y) \phi(y) \right] \propto \mathrm{Det}^{\frac{1}{2}} A, \tag{A.29}$$

we can obtain

$$\Gamma[\bar{\phi}] = \int d^4x \mathcal{L}(\bar{\phi}) + \frac{i}{2} \ln \mathrm{Det} \left[i D_F^{-1}(\bar{\phi}) \right] + \cdots . \tag{A.30}$$

Det in the second term is the determinant for the space-time coordinates and all other field indices. The second term represents the contribution of the 1-loop graph; the contribution of graphs above 2-loops is not explicitly mentioned here. From this, the effective potential $V(\bar{\phi})$ is

$$V(\bar{\phi}) = V_0(\bar{\phi}) + \frac{1}{2}\hbar \int \frac{d^4k}{i(2\pi)^4} \ln \det \left[i D_F^{-1}(k; \bar{\phi}) \right] + \cdots , \tag{A.31}$$

where det in the second term is the determinant for the subscripts of the field. Below I note the 1-loop effective potentials at zero temperature of scalar, fermion, and gauge boson fields.

Scalar field

The Lagrangian of a scalar field is defined as follows

$$\mathcal{L} = \frac{1}{2}\partial^\mu \phi \partial_\mu \phi - V_0(\phi) \tag{A.32}$$

$$V_0 = \frac{1}{2}m^2\phi^2 + \frac{\lambda}{4!}\phi^4. \tag{A.33}$$

From (A.31), the 1-loop effective potential at zero temperature of scalar fields is

$$V_1^{\mathrm{s}}(\phi_c) = \frac{1}{2} \int \frac{d^4p}{(2\pi)^4} \ln \left[p^2 + m^2(\phi_c) \right], \tag{A.34}$$

where ϕ_c is a constant background field.

Fermion field

The Lagrangian of a fermion field is defined as follows

$$\mathcal{L} = i\bar{\psi}_a \gamma \cdot \partial \psi^a - \bar{\psi}_a (M_f)^a_b \psi^b. \tag{A.35}$$

From (A.31), the 1-loop effective potential at zero temperature of fermion fields is

$$V_1^{\mathrm{f}}(\phi_c) = -2\lambda \frac{1}{2} \mathrm{Tr} \int \frac{d^4p}{(2\pi)^4} \ln \left[p^2 + M_f^2(\phi_c) \right], \tag{A.36}$$

where 2λ denotes the degrees of freedom of fermions, where $\lambda = 1(2)$ corresponds to Weil (Dirac) fermions.

Gauge boson field

The Lagrangian of a Gauge boson fields is defined as follows

$$\mathcal{L} = -\frac{1}{4}\,\mathrm{Tr}\left(F_{\mu\nu}F^{\mu\nu}\right) + \frac{1}{2}\,\mathrm{Tr}\left(D_\mu\phi_a\right)^\dagger D^\mu\phi^a + \cdots . \tag{A.37}$$

From (A.31), the 1-loop effective potential at zero temperature of fermion field is

$$V_1^{\mathrm{gb}}\left(\phi_c\right) = \mathrm{Tr}(\Delta)\frac{1}{2}\,\mathrm{Tr}\int\frac{d^4p}{(2\pi)^4}\log\left[p^2 + \left(M_{gb}\right)^2\left(\phi_c\right)\right], \tag{A.38}$$

where $\mathrm{Tr}(\Delta)$ denotes the degrees of freedom of massive gauge bosons, with $\mathrm{Tr}(\Delta) = 3$.

A.1.3 Dimensional regularization

Here, we perform renormalization using dimensional regularization. Extending the scalar effective potential (A.34) to n dimensions, one gets

$$V_1^{\mathrm{s}}\left(\phi_c\right) = \frac{1}{2}\left(\mu^2\right)^{2-\frac{n}{2}}\int\frac{d^np}{(2\pi)^n}\log\left[p^2 + m^2\left(\phi_c\right)\right], \tag{A.39}$$

where μ is the renormalization scale with mass dimension. Differentiating $V_1^{\mathrm{s}}\left(\phi_c\right)$ by $m^2\left(\phi_c\right)$, we obtain

$$V_1^{\mathrm{s}\,\prime}\left(\phi_c\right) = \frac{1}{2}\left(\mu^2\right)^{2-\frac{n}{2}}\int\frac{d^np}{(2\pi)^n}\frac{1}{p^2 + m^2\left(\phi_c\right)}. \tag{A.40}$$

Integrating above equation by $m^2\left(\phi_c\right)$ using the relationship

$$\int d^np\frac{\left(p^2\right)^\alpha}{\left(p^2 + M^2\right)^\beta} = \pi^{\frac{n}{2}}\left(M^2\right)^{\frac{n}{2}+\alpha-\beta}\frac{\Gamma\left(\alpha+\frac{n}{2}\right)\Gamma\left(\beta-\alpha-\frac{n}{2}\right)}{\Gamma\left(\frac{n}{2}\right)\Gamma(\beta)}, \tag{A.41}$$

then yields

$$V_1^{\mathrm{s}}\left(\phi_c\right) = -\frac{1}{32\pi^2}\frac{1}{\frac{n}{2}\left(\frac{n}{2}-1\right)}\left(\frac{m^2\left(\phi_c\right)}{4\pi\mu^2}\right)^{\frac{n}{2}-2}\Gamma\left(2-\frac{n}{2}\right)m^4\left(\phi_c\right). \tag{A.42}$$

Eq. (A.42) can be re-expressed as

$$V_1^{\mathrm{s}}\left(\phi_c\right) = \frac{m^4\left(\phi_c\right)}{64\pi^2}\left\{-\left[\frac{1}{2-\frac{n}{2}} - \gamma_E + \log 4\pi\right] + \log\frac{m^2\left(\phi_c\right)}{\mu^2} - \frac{3}{2} + \mathcal{O}\left(\frac{n}{2}-2\right)\right\}, \tag{A.43}$$

by using

$$\Gamma(z) = \frac{1}{z} - \gamma_E + \mathcal{O}(z), \tag{A.44}$$

with the Euler constant $\gamma_E \approx 0.5772$.

From here, the so-called $\overline{\text{MS}}$ scheme is used to address diverging terms, i.e., the terms proportional to

$$-\frac{m^4(\phi_c)}{64\pi^2}\left\{\frac{1}{2-\frac{n}{2}}-\gamma_E+\log 4\pi\right\}, \tag{A.45}$$

are absorbed by the counter terms. Finally, the 1-loop effective potential at zero temperature of scalar fields casts into form

$$V_1^{\text{s}}(\phi_c)=\frac{1}{64\pi^2}m^4(\phi_c)\left\{\log\frac{m^2(\phi_c)}{\mu^2}-\frac{3}{2}\right\}. \tag{A.46}$$

Similarly, the 1-loop effective potential at zero temperature of scalar fields

$$V_1^{\text{f}}(\phi_c)=-\lambda\frac{1}{32\pi^2}M_f^4(\phi_c)\left\{\log\frac{M_f^2(\phi_c)}{\mu^2}-\frac{3}{2}\right\}, \tag{A.47}$$

$$V_1^{\text{gb}}(\phi_c)=3\frac{1}{64\pi^2}M_{gb}^4(\phi_c)\left\{\log\frac{M_{gb}^2(\phi_c)}{\mu^2}-\frac{5}{6}\right\}. \tag{A.48}$$

As an example, we consider the SM. The $\text{SU}(2)_L$ doublet in the SM is defined as

$$\Phi=\begin{pmatrix}\chi_1+i\chi_2\\ \frac{\phi_c+h+i\chi_3}{\sqrt{2}}\end{pmatrix}, \tag{A.49}$$

where h is the Higgs field and χ_i $(i=1,2,3)$ are Nambu-Goldstone bosons. The tree-level potential with respect to ϕ_c is

$$V_0(\phi_c)=-\frac{m^2}{4}\phi_c^2+\frac{\lambda}{16}\phi_c^4. \tag{A.50}$$

Using the $\overline{\text{MS}}$, the 1-loop effective potential at zero temperature of the SM casts into form

$$V(\phi_c)=V_0(\phi_c)+\frac{1}{64\pi^2}\sum_{i=W,Z,h,t,b}n_i m_i^4(\phi_c)\left[\log\frac{m_i^2(\phi_c)}{\mu^2}-C_i\right] \tag{A.51}$$

$$C_W=C_Z=\frac{5}{6} \tag{A.52}$$

$$C_h=C_t=C_b=\frac{3}{2} \tag{A.53}$$

$$n_W=6, n_Z=3, n_h=1, n_t=n_b=-12. \tag{A.54}$$

Here we consider the contributions of the Higgs boson, the W and Z boson, and the top and bottom quarks which are relatively heavy fermions. The degrees of freedom of each particle are as in Eq. (A.54). On the other hand, using renormalization with cut-off regularization, we finds

$$V(\phi_c)=V_0(\phi_c)+\frac{1}{64\pi^2}\sum_i\left\{m_i^4(\phi_c)\left(\log\frac{m_i^2(\phi_c)}{m_i^2(v)}-\frac{3}{2}\right)+2m_i^2(v)m_i^2(\phi_c)\right\}. \tag{A.55}$$

A.2 Effective potential at finite temperature

A.2.1 Generating functional

To define the effective potential at finite temperature, we start with a grand canonical population. A grand canonical population is a system that can exchange energy and particles with the external world. In a system characterized by a Hamiltonian H, a conserved charge Q_A, the equilibrium state of a stationary system with a large volume V is described by grand canonical density operators:

$$\rho = \exp(-\Phi) \exp\left\{ -\sum_A \alpha_A Q_A - \beta H \right\}, \tag{A.56}$$

$$\Phi = \log \mathrm{Tr} \exp\left\{ -\sum_A \alpha_A Q_A - \beta H \right\}, \tag{A.57}$$

where α_A and β are Lagrange multipliers, which can be expressed as $\alpha_A = -\beta\mu_A, \beta = T^{-1}$ using temperature T and chemical potential μ_A. Also, the grand canonical average of a physical quantity $\mathcal{O}$ can be expressed as

$$\langle \mathcal{O} \rangle \equiv \mathrm{Tr}(\mathcal{O}\rho) \tag{A.58}$$

and satisfies $\langle \mathbf{1} \rangle = 1$.

Consider the case of a real scalar field $\phi(x)$. The chemical potential μ_A is assumed to be zero. The real scalar field $\phi(x)$ can be expressed as

$$\phi(x) = e^{itH} \phi(0, \vec{x}) e^{-itH}, \tag{A.59}$$

and $x_0 = t$ is considered to follow the complex plane. The thermal Green's function is defined as the grand canonical average of the ordinal product of n field operators:

$$G^{(C)}(x_1, \ldots, x_n) \equiv \langle T_C \phi(x_1), \ldots, \phi(x_n) \rangle . \tag{A.60}$$

The T_C ordinal product is reordered along path C on the complex t-plane. That is

$$T_C \phi(x)\phi(y) = \theta_C\left(x^0 - y^0\right) \phi(x)\phi(y) + \theta_C\left(y^0 - x^0\right) \phi(y)\phi(x). \tag{A.61}$$

If we parameterize C as $t = z(\tau)$, then the T_C ordinal product implies the usual ordinal product along the real parameter τ . Thus, the step and delta functions are

$$\theta_C(t) = \theta(\tau), \quad \delta_C(t) = (\partial z/\partial\tau)^{-1} \delta(\tau). \tag{A.62}$$

As in the zero temperature case, the generating functional for the full Green's function is expressed as

$$Z^\beta[j] = \sum_{n=0}^{\infty} \frac{i^n}{n!} \int_C d^4x_1 \ldots d^4x_n j(x_1) \ldots j(x_n) G^{(C)}(x_1, \ldots, x_n), \tag{A.63}$$

and can also be written as

$$Z^{\beta}[j] = \left\langle T_C \exp\left\{ i \int_C d^4x j(x)\dot{\phi}(x) \right\} \right\rangle, \tag{A.64}$$

where $Z^{\beta}[0] = \langle 1 \rangle = 1$ and the integral along t follows the path C in the complex plane. Furthermore, the generating functional of the connected Green's function $W^{\beta}[j]$ is defined by $Z^{\beta}[j] \equiv \exp\left\{iW^{\beta}[j]\right\}$. Using the Legendre transform, the generating functional for 1PI Green functions is given by

$$\Gamma^{\beta}[\bar{\phi}] = W^{\beta}[j] - \int_C d^4x \frac{\delta W^{\beta}[j]}{\delta j(x)} j(x). \tag{A.65}$$

Here the classical field $\bar{\phi}(x)$ can be expressed as $\bar{\phi}(x) = \delta W^{\beta}[j]/\delta j(x)$, which makes $\delta\Gamma^{\beta}[\bar{\phi}]/\delta\bar{\phi}(x) = -j(x)$. $\bar{\phi}(x) = \langle\phi(x)\rangle$ is the grand canonical average of $\phi(x)$. Here we can define the effective potential at finite temperature by removing the overall factor of space-time volume appearing in each term of $\Gamma^{\beta}\left[\bar{\phi}\right]$ as follows:

$$\Gamma^{\beta}\left[\phi_c\right] = -\int d^4x V_{\text{eff}}^{\beta}\left(\phi_c\right). \tag{A.66}$$

Also, symmetry breaking occurs when

$$\frac{\partial V_{\text{eff}}^{\beta}\left(\phi_c\right)}{\partial \phi_c} = 0. \tag{A.67}$$

Scalar field

Using Eq. (A.61), the two-point Green function is

$$G^{(C)}(x-y) = \theta_C\left(x^0 - y^0\right) G_+(x-y) + \theta_C\left(y^0 - x^0\right) G_-(x-y), \tag{A.68}$$

where

$$G_+(x-y) = \langle\phi(x)\phi(y)\rangle, \quad G_-(x-y) = G_+(y-x). \tag{A.69}$$

After some calculations, Eq. (A.68) takes the form

$$G^{(C)}(x-y) = \int \frac{d^4p}{(2\pi)^4} 2\pi \left[\theta\left(p^0\right) - \theta\left(-p^0\right)\right] \delta\left(p^2 - m^2\right) e^{-ip(x-y)} \left[\theta_C\left(x^0 - y^0\right) + n_B\left(p^0\right)\right], \tag{A.70}$$

where $n_B\left(\omega\right)$ represents the Bose distribution function

$$n_B(\omega) = \frac{1}{e^{\beta\omega} - 1}. \tag{A.71}$$

The periodicity relation affecting the Green function, called the Kubo-Martin-Schwinger relation, is derived as

$$G_+(t - i\beta, \vec{x}) = G_-(t, \vec{x}). \tag{A.72}$$

Fermion field

The two-point Green function in the fermion case can be expressed as

$$S_{\alpha\beta}^{(C)}(x-y) \equiv \left\langle T_C \psi_\alpha(x) \bar{\psi}_\beta(y) \right\rangle = \theta_C \left(x^0 - y^0\right) S_{\alpha\beta}^{+} - \theta_C \left(y^0 - x^0\right) S_{\alpha\beta}^{-}, \tag{A.73}$$

where

$$S_{\alpha\beta}^{+}(x-y) = \left\langle \psi_\alpha(x) \bar{\psi}_\beta(y) \right\rangle. \tag{A.74}$$

After some calculations, Eq. (A.73) takes the form

$$S^{(C)}(x-y) = \int \frac{d^4p}{(2\pi)^4} 2\pi \left[\theta\left(p^0\right) - \theta\left(-p^0\right)\right] \delta\left(p^2 - m^2\right) e^{-ip(x-y)} \left[\theta_C\left(x^0 - y^0\right) - n_F\left(p^0\right)\right], \tag{A.75}$$

where $n_F(\omega)$ represents the Bose distribution function

$$n_F(\omega) = \frac{1}{e^{\beta\omega} + 1}. \tag{A.76}$$

The reduced Green function $S^{(C)}(x-y)$ satisfies the Kubo-Martin-Schwinger relation

$$S_{\alpha\beta}^{+}(t - i\beta, \vec{x}) = -S_{\alpha\beta}^{-}(t, \vec{x}). \tag{A.77}$$

A.2.2 1-loop effective potential at finite temperature

The calculation of the propagator depends on the choice of path C from initial time t to $t - i\beta$. The simplest path is a straight line along the imaginary axis $t = -i\tau$, called the Matsubara contour. The two-point Green functions can be expressed as

$$G(\tau, \vec{x}) = \int \frac{d^4p}{(2\pi)^4} 2\pi \left[\theta\left(p^0\right) - \theta\left(-p^0\right)\right] \delta\left(p^2 - m^2\right) e^{i\vec{p}\vec{x}} e^{-\tau p^0} \left[\theta(\tau) + \eta n_{B,F}\left(p^0\right)\right], \tag{A.78}$$

where $\eta = 1$ for bosons and $\eta = -1$ for fermions. The Green function can be decomposed as

$$G(\tau, \vec{x}) = G_+(\tau, \vec{x})\theta(\tau) + G_-(\tau, \vec{x})\theta(-\tau), \tag{A.79}$$

where $G(\tau + \beta) = \eta G(\tau)$ for $-\beta \leq \tau \leq 0$, $G(\tau - \beta) = \eta G(\tau)$ for $0 \leq \tau \leq \beta$. The Fourier transform of Eq. (A.78) is

$$\widetilde{G}\left(\omega_n, \vec{p}\right) = \int_{\alpha-\beta}^{\alpha} d\tau \int d^3x e^{i\omega_n \tau - i\vec{x}\vec{p}} G(\tau, \vec{x}), \tag{A.80}$$

where $\omega_n = 2n\pi\beta^{-1}$ for bosons and $\omega_n = (2n+1)\pi\beta^{-1}$ for fermions. From Eqs. (A.78) (A.80), one finds

$$\widetilde{G}\left(\omega_n, \vec{p}\right) = \frac{1}{\vec{p}^2 + m^2 + \omega_n^2}. \tag{A.81}$$

Inverse Fourier transform of Eq. (A.81) yields the euclidean propagator:

$$\Delta(x) = \frac{1}{\beta}\sum_{n=-\infty}^{\infty}\int \frac{d^3p}{(2\pi)^3} e^{-i\omega_n\tau + i\vec{p}\vec{x}} \frac{-i}{\vec{p}^2 + m^2 + \omega_n^2}, \tag{A.82}$$

where $G(\tau,\vec{x}) = i\Delta(-i\tau,\vec{x})$. As can be seen Eq. (A.82), the Feynman rule for finite temperature is given as follows:

$$\begin{aligned}
\text{Loop integral} &: \frac{i}{\beta}\sum_{n=-\infty}^{\infty}\int\frac{d^3p}{(2\pi)^3} \\
\text{Vertex function} &: -i\beta(2\pi)^3\delta\sum_{\omega_i}\delta^{(3)}\left(\sum_i \vec{p}_i\right) \\
\text{Boson propagator} &: \frac{i}{p^2 - m^2} \qquad (A.83) \\
&\quad p^\mu = \left[2ni\pi\beta^{-1}, \vec{p}\right] \\
\text{Fermion propagator} &: \frac{i}{\gamma\cdot p - m} \qquad (A.84) \\
&\quad p^\mu = \left[(2n+1)i\pi\beta^{-1}, \vec{p}\right]. \qquad (A.85)
\end{aligned}$$

Scalar field

The tree-level potential of scalar fields is given by Eqs. (A.32) and (A.33). Using the Feynman rule (A.85), Eq. (A.34) can be rewritten as

$$V_1^\beta(\phi_c) = \frac{1}{2\beta}\sum_{n=-\infty}^{\infty}\int\frac{d^3p}{(2\pi)^3}\log\left(\omega_n^2 + \omega^2\right), \tag{A.86}$$

where ω_n is the Matsubara frequency in bosons, and $\omega^2 = \vec{p}^2 + m^2(\phi_c)$. To compute Eq. (A.86) we consider

$$\frac{\partial a(\omega)}{\partial\omega} = \sum_{n=-\infty}^{\infty}\frac{2\omega}{\omega_n^2 + \omega^2}, \tag{A.87}$$

where $a(\omega) \equiv \sum_{n=-\infty}^{\infty}\log\left(\omega_n^2 + \omega^2\right)$. Using the identity

$$\begin{aligned}
f(y) = \sum_{n=1}^{\infty}\frac{y}{y^2+n^2} &= -\frac{1}{2y} + \frac{1}{2}\pi\coth\pi y \\
&= -\frac{1}{2y} + \frac{\pi}{2} + \pi\frac{e^{-2\pi y}}{1 - e^{-2\pi y}},
\end{aligned} \tag{A.88}$$

one finds

$$\frac{\partial a(\omega)}{\partial\omega} = 2\beta\left[\frac{1}{2} + \frac{e^{-\beta\omega}}{1 - e^{-\beta\omega}}\right]. \tag{A.89}$$

Integrating this yields

$$a(\omega) = 2\beta\left[\frac{w}{2} + \frac{1}{\beta}\log\left(1 - e^{-\beta\omega}\right)\right]. \tag{A.90}$$

Substituting this into Eq. (A.86), one gets

$$V_1^{\beta}\left(\phi_c\right) = \int \frac{d^3p}{(2\pi)^3}\left[\frac{\omega}{2} + \frac{1}{\beta}\log\left(1 - e^{-\beta\omega}\right)\right]. \tag{A.91}$$

The first term in Eq. (A.91) represents the zero temperature 1-loop effective potential in equation (A.34) itself. The second term in Eq. (A.91) is converted to

$$\frac{1}{\beta}\int \frac{d^3p}{(2\pi)^3}\log\left(1 - e^{-\beta\omega}\right) = \frac{1}{2\pi^2\beta^4} I_B\left[m^2\left(\phi_c\right)\beta^2\right], \tag{A.92}$$

$$I_B\left[m^2\beta^2\right] = \int_0^{\infty} dx x^2 \log\left[1 - e^{-\sqrt{x^2+\beta^2m^2}}\right]. \tag{A.93}$$

When Eq. (A.93) is expanded to high temperature, one obtains

$$I_B\left(m^2/T^2\right) \simeq -\frac{\pi^4}{45} + \frac{\pi^2}{12}\frac{m^2}{T^2} - \frac{\pi}{6}\left(\frac{m^2}{T^2}\right)^{3/2} - \frac{1}{32}\frac{m^4}{T^4}\log\frac{m^2}{a_bT^2}. \tag{A.94}$$

Fermion field

The tree-level potential of fermion fields is given by Eqs. (A.35). Using the Feynman rule (A.85), Eq. (A.36) can be rewritten as

$$V_1^{\beta}\left(\phi_c\right) = -\frac{2\lambda}{2\beta}\sum_{n=-\infty}^{\infty}\int \frac{d^3p}{(2\pi)^3}\log\left(\omega_n^2 + \omega^2\right), \tag{A.95}$$

where ω_n is the Matsubara frequency in fermions, and $\omega^2 = \vec{p}^2 + M_f^2\left(\phi_c\right)$. Calculating as in the case of a scalar field, we obtain

$$\frac{\partial a}{\partial \omega} = \frac{4\beta}{\pi}\sum_{1,3,\ldots}\frac{y}{y^2+n^2} = 2\beta\left[\frac{1}{2} - \frac{1}{1+e^{\beta\omega}}\right]. \tag{A.96}$$

Integrating this yields

$$a(\omega) = 2\beta\left[\frac{w}{2} + \frac{1}{\beta}\log\left(1 + e^{-\beta\omega}\right)\right]. \tag{A.97}$$

Substituting this into Eq. (A.95), one gets

$$V_1^{\beta}\left(\phi_c\right) = -2\lambda\int \frac{d^3p}{(2\pi)^3}\left[\frac{\omega}{2} + \frac{1}{\beta}\log\left(1 + e^{-\beta\omega}\right)\right],. \tag{A.98}$$

The first term in Eq. (A.98) represents the zero temperature 1-loop effective potential in equation (A.36) itself. The second term in Eq. (A.98) is converted to

$$-2\lambda\frac{1}{\beta}\int \frac{d^3p}{(2\pi)^3}\log\left(1 + e^{-\beta\omega}\right) = -2\lambda\frac{1}{2\pi^2\beta^4} I_F\left[M_f^2\left(\phi_c\right)\beta^2\right] \tag{A.99}$$

$$I_F\left[m^2\beta^2\right] = \int_0^{\infty} dx x^2 \log\left[1 + e^{-\sqrt{x^2+\beta^2m^2}}\right]. \tag{A.100}$$

When Eq. (A.100) is expanded to high temperature, one obtains

$$I_F\left(m^2/T^2\right) \simeq \frac{7\pi^4}{360} - \frac{\pi^2}{24}\frac{m^2}{T^2} - \frac{1}{32}\frac{m^4}{T^4}\log\frac{m^2}{a_f T^2}. \tag{A.101}$$

Gauge boson field

The tree-level potential of gauge boson fields is given by Eqs. (A.37). Using the Feynman rule (A.85), Eq. (A.38) can be rewritten as

$$V_1^\beta\left(\phi_c\right) = \mathrm{Tr}(\Delta)\frac{1}{2\beta}\sum_{n=-\infty}^{\infty}\int\frac{d^3p}{(2\pi)^3}\log\left(\omega_n^2+\omega^2\right), \tag{A.102}$$

where ω_n is the Matsubara frequency in bosons, and $\omega^2 = \vec{p}^2 + M_{gb}^2\left(\phi_c\right)$. Calculating this as before leads to the zero temperature effective potential and the finite temperature effective potential as in

$$V_1^\beta\left(\phi_c\right) = \mathrm{Tr}(\Delta)\left\{\frac{1}{2}\int\frac{d^4p}{(2\pi)^4}\log\left[p^2+M_{gb}^2\left(\phi_c\right)\right] + \frac{1}{2\pi^2\beta^4}I_B\left[M_{gb}^2\left(\phi_c\right)\beta^2\right]\right\}. \tag{A.103}$$

I_B in the second term of Eq. (A.103) refers to Eq. (A.93).

Appendix B

Field dependent mass

B.1 CPC CxSM

We enumerate the field dependent masses and derive the thermal mass of the scalars. First, we focus on the CPC CxSM. The scalar mass matrix takes the form 2-by-2:

$$\frac{1}{2}\begin{pmatrix}\varphi & \varphi_S\end{pmatrix}\bar{\mathcal{M}}_S^2\begin{pmatrix}\varphi\\ \varphi_S\end{pmatrix}, \tag{B.1}$$

where

$$\bar{\mathcal{M}}_S^2(\varphi,\varphi_S) = \begin{pmatrix} \frac{m^2}{2}+\frac{3\lambda}{4}\varphi^2+\frac{\delta_2}{4}\varphi_S^2 & \frac{\delta_2}{2}\varphi\varphi_S \\ \frac{\delta_2}{2}\varphi\varphi_S & \frac{b_2}{2}+\frac{b_1}{2}+\frac{\delta_2}{4}\varphi^2+\frac{3d_2}{4}\varphi_S^2 \end{pmatrix} \tag{B.2}$$

$$\equiv \begin{pmatrix} \bar{m}_h^2(\varphi,\varphi_S) & \frac{\delta_2}{2}\varphi\varphi_S \\ \frac{\delta_2}{2}\varphi\varphi_S & \bar{m}_{h_S}^2(\varphi,\varphi_S) \end{pmatrix}. \tag{B.3}$$

The field dependent masses of the NG bosons, gauge bosons and top/bottom are, respectively, given by

$$\bar{m}_{G^0}^2 = \bar{m}_{G^\pm}^2 = \frac{m^2}{2}+\frac{\lambda}{4}\varphi^2+\frac{\delta_2}{4}\varphi_S^2, \tag{B.4}$$

$$\bar{m}_W^2 = \frac{g_2^2}{4}\varphi^2, \quad \bar{m}_Z^2 = \frac{g_2^2+g_1^2}{4}\varphi^2, \tag{B.5}$$

$$\bar{m}_t^2 = \frac{y_t^2}{2}\varphi^2, \quad \bar{m}_b^2 = \frac{y_b^2}{2}\varphi^2. \tag{B.6}$$

The eigenvalues of CP-even scalars are

$$\bar{m}_{h_{1,2}}^2(\varphi,\varphi_S) = \frac{1}{2}\left[\bar{m}_h^2+\bar{m}_{h_S}^2 \mp \sqrt{\left(\bar{m}_h^2-\bar{m}_{h_S}^2\right)^2+\delta_2^2\varphi^2\varphi_S^2}\right]. \tag{B.7}$$

The thermal mass of the Higgs field φ appearing in the HT potential (5.59) is calculated as follows:

$$\begin{aligned}\Sigma_H T^2 &= \frac{\partial^2 V_1|_{T>0}}{\partial\varphi^2} = \sum_i n_i \left[\frac{T^2}{2\pi^2}\frac{\partial I_{B,F}(a_i^2)}{\partial a_i^2}\frac{\partial^2\bar{m}_i^2}{\partial\varphi^2} + \frac{1}{2\pi^2}\frac{\partial^2 I_{B,F}(a_i^2)}{\partial(a_i^2)^2}\left(\frac{\partial\bar{m}_i^2}{\partial\varphi}\right)^2\right] \\ &\simeq \frac{T^2}{24}\sum_{i=\text{bosons}} n_i\frac{\partial^2\bar{m}_i^2}{\partial\varphi^2} - \frac{T^2}{48}\sum_{i=\text{fermions}} n_i\frac{\partial^2\bar{m}_i^2}{\partial\varphi^2} \\ &= \left[\frac{\lambda}{8} + \frac{\delta_2}{24} + \frac{1}{16}(3g_2^2 + g_1^2) + \frac{1}{4}(y_t^2 + y_b^2)\right]T^2, \end{aligned} \tag{B.8}$$

where $\sum_{i=1,2}\bar{m}_i^2 = \sum_{i=1,2}(\bar{\mathcal{M}}_S^2)_{ii}$ is used for the scalars. Similarly, the thermal mass of the singlet field φ_S is represented by

$$\Sigma_S T^2 = \frac{\partial^2 V_1|_{T>0}}{\partial\varphi_S^{r2}} = \frac{\partial^2 V_1|_{T>0}}{\partial\varphi_S^{i2}} = \frac{\delta_2 + d_2}{12}T^2. \tag{B.9}$$

B.2 CPV CxSM

In the presence of CP violation, the mass matrix of the scalars takes the 3-by-3 form

$$\frac{1}{2}\begin{pmatrix}\varphi & \varphi_S^r & \varphi_S^i\end{pmatrix}\bar{\mathcal{M}}_S^2\begin{pmatrix}\varphi \\ \varphi_S^r \\ \varphi_S^i\end{pmatrix}, \tag{B.10}$$

where

$$(\bar{\mathcal{M}}_S^2)_{11} = \frac{m^2}{2} + \frac{3\lambda}{4}\varphi^2 + \frac{\delta_2}{4}|\varphi_S|^2, \tag{B.11}$$

$$(\bar{\mathcal{M}}_S^2)_{22} = \frac{b_2}{2} + \frac{b_1^r}{2} + \frac{d_2}{4}(3\varphi_S^{r2} + \varphi_S^{i2}) + \frac{\delta_2}{4}\varphi^2, \tag{B.12}$$

$$(\bar{\mathcal{M}}_S^2)_{33} = \frac{b_2}{2} - \frac{b_1^r}{2} + \frac{d_2}{4}(\varphi_S^{r2} + 3\varphi_S^{i2}) + \frac{\delta_2}{4}\varphi^2, \tag{B.13}$$

$$(\bar{\mathcal{M}}_S^2)_{12} = \frac{\delta_2}{2}\varphi\varphi_S^r, \tag{B.14}$$

$$(\bar{\mathcal{M}}_S^2)_{13} = \frac{\delta_2}{2}\varphi\varphi_S^i, \tag{B.15}$$

$$(\bar{\mathcal{M}}_S^2)_{23} = -\frac{b_1^i}{2} + \frac{d_2}{2}\varphi_S^r\varphi_S^i, \tag{B.16}$$

with $|\varphi_S|^2 = \varphi_S^{r2} + \varphi_S^{i2}$. The thermal masses of φ is same as Eq. (B.8) and those of φ_S^r, φ_S^i are same as Eq. (B.9).

Appendix C

Theoretical constraints on parameters

A requirement on the scalar potential that is bounded from below is given by

$$\lambda > 0, d_2 > 0. \tag{C.1}$$

When the scalar fields take on large values, the scalar potential is dominated by the quartic terms of fields. Thus, we consider the condition that the quartic terms of scalar fields is positive:

$$\frac{\lambda}{4}|H|^4 + \frac{\delta_2}{2}|H|^2|S|^2 + \frac{d_2}{4}|S|^4 > 0. \tag{C.2}$$

If $\delta_2 > 0$, then Eq. (C.2) holds. When $\delta_2 < 0$, we finds

$$\lambda\left(|H|^2 + \frac{\delta_2}{\lambda}|S|^2\right)^2 + \left(d_2 - \frac{\delta_2^2}{\lambda}\right)|S|^4 > 0. \tag{C.3}$$

The first term of Eq. (C.3) is always positive, which leads to

$$\lambda d_2 > \delta_2^2. \tag{C.4}$$

Furthermore, we consider constraints from perturbation theory. The S matrix is an operator that gives the relationship between initial and final states, and can be expressed as

$$\langle f|S|i\rangle = (2\pi)^4\delta^{(4)}\left(p_f - p_i\right) i\mathcal{M}, \tag{C.5}$$

where $\mathcal{M}$ is a scattering amplitude and $p_i(p_f)$ is an initial (final) momentum. Using the amplitude of the partial wave a_j with angular momentum j, the scattering amplitude $\mathcal{M}$ is

$$\mathcal{M}(\theta) = 16\pi\sum_{j=0}^{\infty} a_j(2j+1)P_j(\cos\theta), \tag{C.6}$$

where $P_j(x)$ is the Legendre polynomial, which is expressed as

$$P_j(x) = \frac{1}{2^j j!}\frac{\mathrm{d}^j}{\mathrm{d}x^j}\left(x^2-1\right)^j. \tag{C.7}$$

The S matrix is a unitary matrix, i.e., $S^\dagger S = 1$, which gives the following constraints on a_0 with angular momentum $j = 0$:

$$|a_0| \leqq 1, \quad \mathrm{Re}\,[a_0] \leqq \frac{1}{2}. \tag{C.8}$$

When $j = 0$, one gets

$$\mathcal{M}_{(j=0)} = 16\pi \cdot a_0, \tag{C.9}$$

and conditional equation

$$|\mathcal{M}| \leqq 8\pi, \tag{C.10}$$

is derived by using the second equation of (C.8).

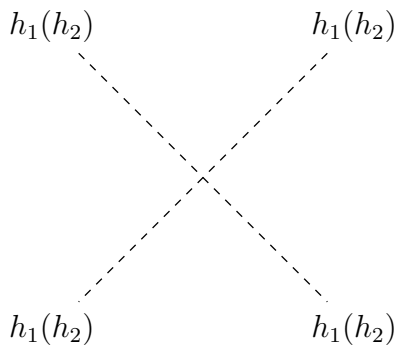

Figure C.1: Diagram of 4-point interaction of $h_1(h_2)$

Now, we consider 4-point interaction of $h_1(h_2)$ expressed in Fig. C.1. From the Feynman Rules, one can derive

$$i\mathcal{M} = i \cdot \frac{\lambda}{16} \cdot 4!, \quad i\mathcal{M} = i \cdot \frac{d_2}{16} \cdot 4!. \tag{C.11}$$

From Eq. (C.10), conditions from the perturbative unitarity is expressed as

$$\lambda, d_2 \leqq \frac{16\pi}{3}. \tag{C.12}$$

Finally, to guarantee the vacuum stability , one should request that the eigenvalues of the mass matrix (5.10) are positive, which leads to

$$\lambda \left(d_2 - \frac{2\sqrt{2}a_1}{v_S^3} \right) > \delta_2^2. \tag{C.13}$$

In this study, the mass eigenvalues are treated as input parameters and take positive values, so it is inevitable that the above condition is satisfied.

Appendix D

Sum rules of 1-loop scattering of DM and quarks

We study the 1-loop contributions to the DM-quark scattering in the degenerate scalar scenario. Here, we use the minimal tree-level scalar potential (5.1) which is known to satisfy the condition of the cancellation mechanism. The H-S mixing δ_2 is given by

$$\delta_2 = \frac{2}{vv_S}\left(m_{h_1}^2 - m_{h_2}^2\right)\sin\alpha\cos\alpha. \tag{D.1}$$

δ_2 becomes zero in the degenerate scalar limit. We classify the 1-loop diagrams for the DM-quark scattering into five groups as summarized in Figs. D.1-D.5. The amplitudes of the diagrams for each group are shown in the non-relativistic limit of the momentum transfer $t \to 0$ and the degenerate scalar limit $m_{h_1} = m_{h_2} \equiv m$.

D.1 Group-1

The diagrams belonging to Group-1 (Fig. D.1) contain the tree-level diagram ($\chi\chi \to (h_i) \to qq$) as a subdiagram. Consequently, each diagram in this group vanishes for the same reason as the tree-level diagram. Specifically, regarding Fig. D.1 (a), particle A denotes all Standard Model (SM) particles excluding the Higgs, all of which solely couple with the SM Higgs h. Therefore, these contributions cancel out through the same mechanism observed in the DM-quark scattering at the tree-level.

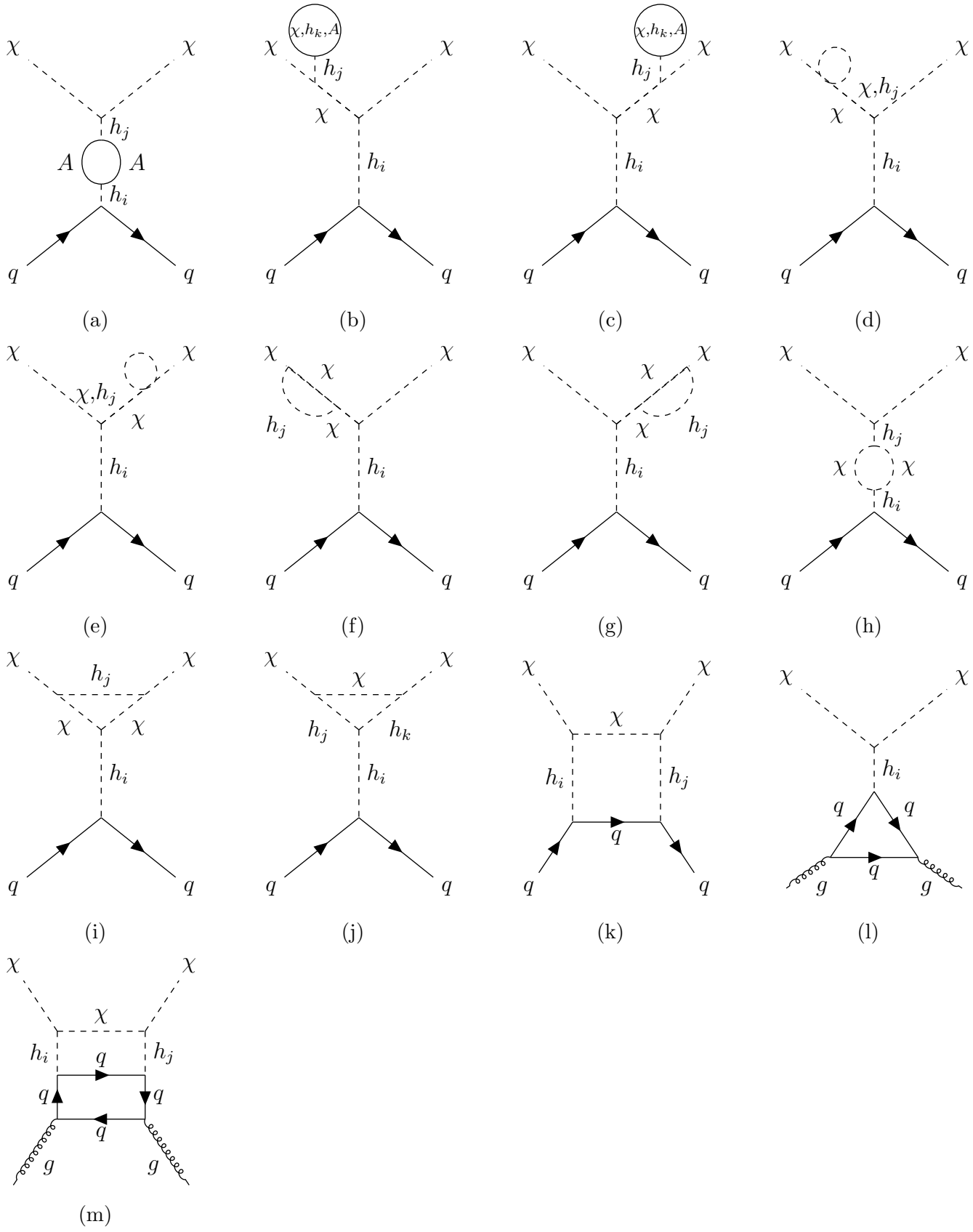

Figure D.1: Group-1: 1-loop diagrams including the tree-level structure as a subdiagram.

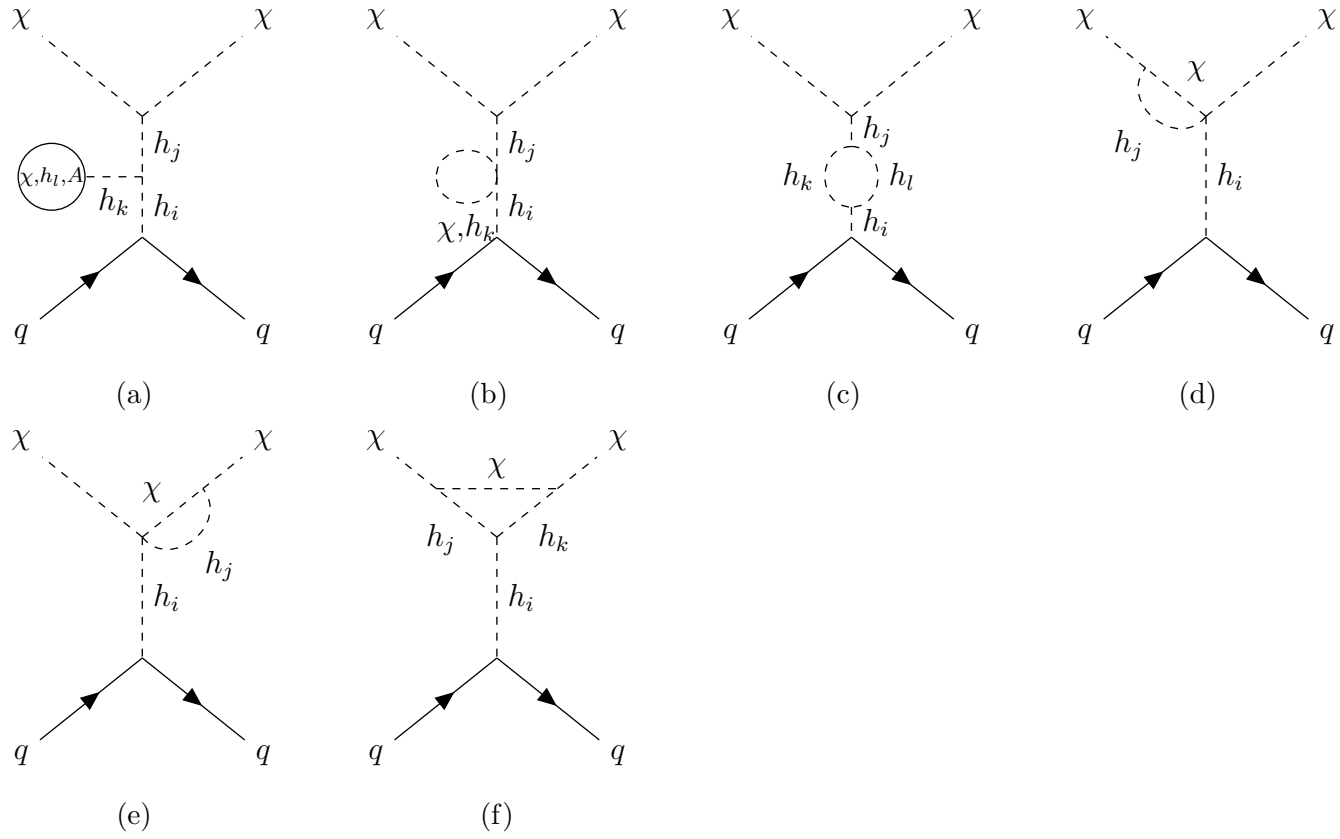

Figure D.2: Group-2: 1-loop diagrams including one Yukawa coupling $C_{ff h_i}$ and scalar trilinear coupling $C_{\chi\chi h_j}$.

D.2 Group-2

The scattering amplitudes described by the diagrams in Fig. D.2 (α), where $\alpha = \mathrm{a} \sim \mathrm{f}$, can be represented as follows[1]:

$$i\mathcal{M}^\alpha = i\left(\sum_{A=1,2} C_{\chi\chi h_i} C_{qqh_A} F^\alpha_{Ai}\right) f(m^2)\bar{u}(p_3)u(p_1), \tag{D.2}$$

where the scalar h_A is defined as the Higgs that couples to the external quark lines, while h_i is defined as the Higgs that interacts with the χ pair. The factor F^α_{Ai} constains all the couplings and $f(m^2)$ contains propagators. Only exception is Fig. D.2 (a), where F^α_{Ai} contains only $C_{h_ih_jh_k}$ and tadpole couplings are included in $f(m^2)$.

The condition to suppress the scattering amplitude ($\mathcal{M}^\alpha = 0$) is given as follows:

$$\begin{aligned}\sum_{A=1,2} C_{\chi\chi h_i} C_{qqh_A} F^\alpha_{Ai} &= C_{\chi\chi s}\left\{(F^\alpha_{11} - F^\alpha_{22})\cos\alpha\sin\alpha + F^\alpha_{12}\cos^2\alpha - F^\alpha_{21}\sin^2\alpha\right\} \\ &= 0.\end{aligned} \tag{D.3}$$

[1]The symmetry factor according to the identical particles at the vertex is suppressed.

Since $C_{\chi\chi h}$ is given by δ_2 as can be seen from (5.41), we have dropped $C_{\chi\chi h}$ because δ_2 becomes zero for $m_{h_1} = m_{h_2}$ (D.1). In general, the parameter F^α_{Ai} is represented by the scalar trilinear and/or quartic couplings, which are given by δ_2, λ and d_2, whose specific expressions are given in Sec. D.6. Thus, in the degenerate mass limit, F^α_{Ai} can be expanded as

$$F^\alpha_{1i} = a^\alpha_{1i}\lambda + b^\alpha_{1i} d_2, \quad F^\alpha_{2i} = a^\alpha_{2i}\lambda + b^\alpha_{2i} d_2. \tag{D.4}$$

Thus, the condition (D.3) is replaced by the following two conditions, which should be satisfied simultaneously

$$(a^\alpha_{11} - a^\alpha_{22})\cos\alpha\sin\alpha + a^\alpha_{12}\cos^2\alpha - a^\alpha_{21}\sin^2\alpha = 0, \tag{D.5}$$

$$(b^\alpha_{11} - b^\alpha_{22})\cos\alpha\sin\alpha + b^\alpha_{12}\cos^2\alpha - b^\alpha_{21}\sin^2\alpha = 0. \tag{D.6}$$

For illustration, we examine the amplitude given by Fig. D.2 (a):

$$i\mathcal{M}^{\rm a} = \frac{-1}{m^6}\bar{u}(p_3)u(p_1)\left(\sum_{l=\chi,h_1,h_2,A} C_{llh_k}\frac{i}{16\pi^2}A(m_l)\right) \times \left(C_{qqh_1}C_{\chi\chi h_j}C_{h_1h_jh_k} + C_{qqh_2}C_{\chi\chi h_j}C_{h_2h_jh_k}\right), \tag{D.7}$$

where $j,k = 1,2$, and $A(m)$ is the A-function proposed by Passarino and Veltman [111]. Comparing (D.7) with (D.2), the parameter F^α_{Ai} is given by the trilinear couplings as

$$F^{\rm a}_{1j} = C_{h_1h_jh_k}, \quad F^{\rm a}_{2j} = C_{h_2h_jh_k}. \tag{D.8}$$

Taking account of the symmetry factors, $F^{\rm a}_{Ai}$ for $k = 1$ are given as

$$F^{\rm a}_{11} = 6C_{111} = \frac{3}{2}\left(\lambda v\cos^3\alpha + d_2 v_s\sin^3\alpha\right), \tag{D.9}$$

$$F^{\rm a}_{12} = 2C_{112} = \frac{3}{2}\left(-\lambda v\sin\alpha\cos^2\alpha + d_2 v_s\sin^2\alpha\cos\alpha\right), \tag{D.10}$$

$$F^{\rm a}_{21} = 2C_{112} = \frac{3}{2}\left(-\lambda v\sin\alpha\cos^2\alpha + d_2 v_s\sin^2\alpha\cos\alpha\right), \tag{D.11}$$

$$F^{\rm a}_{22} = 2C_{122} = \frac{3}{2}\left(\lambda v\sin^2\alpha\cos\alpha + d_2 v_s\sin\alpha\cos^2\alpha\right). \tag{D.12}$$

It is easy to confirm that Eqs. (D.9)-(D.12), and those for $k = 2$ satisfy the conditions (D.5) and (D.6), so the amplitude given by Fig. D.2 (a) vanishes in the degenerate scalar limit. Other diagrams in Fig. D.2 will disappear as well.

D.3 Group-3

The diagrams in Group-3 have the Yukawa couplings C_{qqh_i} and the scalar quartic coupling $C_{h_ih_j\chi\chi}$ as shown in Figs. D.3. The amplitude of Fig. D.3 (a) is given as

$$i\mathcal{M}^{\rm a} = \frac{1}{m^2}\frac{i}{16\pi^2}B_0(m,m)\bar{u}(p_3)u(p_1)\left(C_{qqh_1}C_{h_1h_jh_k} + C_{qqh_2}C_{h_2h_jh_k}\right)C_{\chi\chi h_jh_k}, \tag{D.13}$$

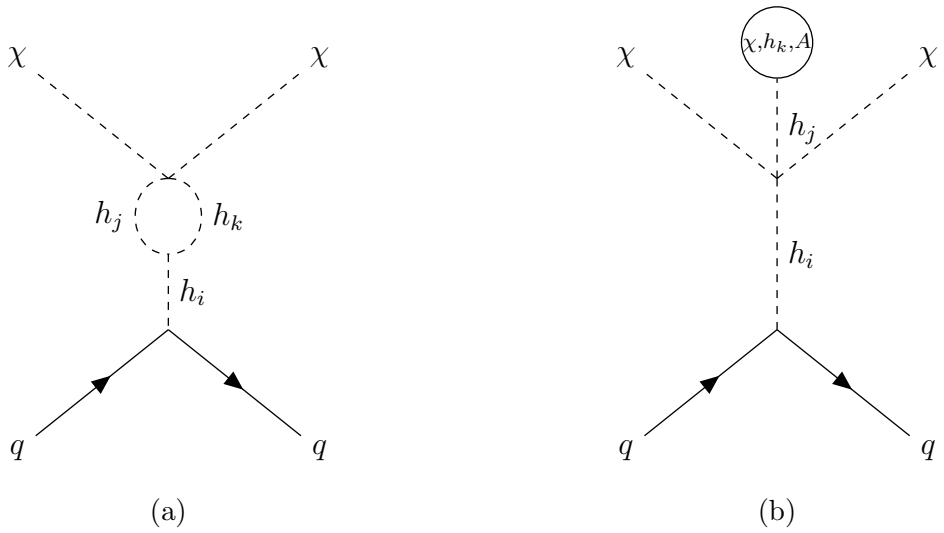

Figure D.3: Group-3: 1-loop diagrams including one Yukawa coupling $C_{ff h_i}$ and scalar quartic coupling $C_{\chi\chi h_j h_k}$.

where $B_0(m,m)$ is the B-function proposed in [111]. The condition to vanish the amplitude is given as follows:

$$\big(C_{h_1 h_j h_k}\cos\alpha - C_{h_2 h_j h_k}\sin\alpha\big)C_{\chi\chi h_j h_k} = 0, \tag{D.14}$$

where (5.23) is used. Summing up (D.14) for j and k, and substituting trilinear and quartic couplings, one can find that (D.14) is satisfied.

Similarly, we consider Fig. D.3 (b). The scattering amplitude is given by

$$i\mathcal{M}^{\rm b} = \frac{-1}{m^4}\bar{u}(p_3)u(p_1)\left(\sum_{l=\chi,h_1,h_2,A} C_{llA}\frac{i}{16\pi^2}A(m_l)\right)\big(C_{qqh_1}C_{\chi\chi h_j h_1} + C_{qqh_2}C_{\chi\chi h_j h_2}\big). \tag{D.15}$$

The sum rule for $\mathcal{M}^{\rm b} = 0$ is

$$C_{\chi\chi h_j h_1}\cos\alpha - C_{\chi\chi h_j h_2}\sin\alpha = 0. \tag{D.16}$$

One can also find that (D.16) is satisfied.

D.4 Group-4

The Feynman diagram of Group-4 given in Fig. (D.4) has two Yukawa couplings. The scattering amplitude is given by

$$\begin{aligned} i\mathcal{M} = \frac{-1}{m^2}\bar{u}(p_3)u(p_1)&\left(\frac{i}{16\pi^2}C^{\mu}(m_q,m,m)\right) \\ &\times \big(C_{\chi\chi h_1}C_{h_1 h_j h_k} + C_{\chi\chi h_2}C_{h_2 h_j h_k}\big)C_{qqh_j}C_{qqh_k}, \end{aligned} \tag{D.17}$$

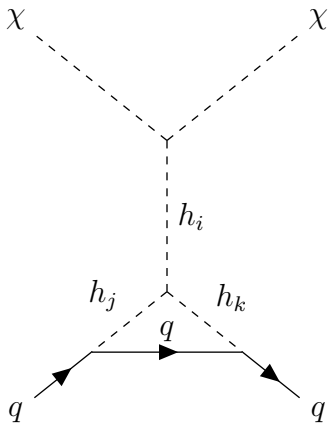

Figure D.4: Group-4: 1-loop diagram including two Yukawa coupling C_{ffh_i} and scalar trilinear coupling $C_{\chi\chi h_j}$.

where the rank-1 C-function C^μ is proposed in [111]. The sum rule for $\mathcal{M} = 0$ is

$$\left(C_{\chi\chi h_1}C_{h_1h_jh_k} + C_{\chi\chi h_2}C_{h_2h_jh_k}\right)C_{qqh_j}C_{qqh_k} = 0. \tag{D.18}$$

D.5 Group-5

The Feynman diagram of Group-5 is given in Fig. D.5, which has the scalar quartic coupling and two Yukawa couplings. Up to the quark-gluon scattering part, the amplitudes of Fig. D.5 is given by

$$i\mathcal{M} = \left(\frac{i}{16\pi^2}C^\mu(m_q, m, m)\right)\bar{u}(p_3)u(p_1)C_{\chi\chi h_ih_j}C_{qqh_i}C_{qqh_j}. \tag{D.19}$$

The sum rule for $\mathcal{M} = 0$ is

$$C_{\chi\chi h_ih_j}C_{qqh_i}C_{qqh_j} = 0. \tag{D.20}$$

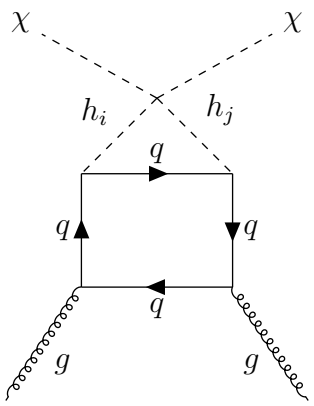

Figure D.5: Group-5: 1-loop diagram including two Yukawa coupling C_{ffh_i} and scalar quartic coupling $C_{\chi\chi h_j h_k}$.

D.6 Trilinear and quartic couplings in the minimal scalar potential

In the mass eigenstates of scalars h_1, h_2 and the DM χ, the trilinear and quartic terms of the scalar potential are given by

$$\begin{aligned} V =& C_{111}h_1^3 + C_{112}h_1^2 h_2 + C_{122}h_1 h_2^2 + C_{222}h_2^3 + C_{\chi\chi 1}h_1\chi^2 + C_{\chi\chi 2}h_2\chi^2 \\ &+ C_{1111}h_1^4 + C_{1112}h_1^3 h_2 + C_{1122}h_1^2 h_2^2 + C_{1222}h_1 h_2^3 + C_{2222}h_2^4 \\ &+ C_{\chi\chi 11}h_1^2\chi^2 + C_{\chi\chi 12}h_1 h_2\chi^2 + C_{\chi\chi 22}h_2^2\chi^2 + C_{\chi\chi\chi\chi}\chi^4. \end{aligned} \tag{D.21}$$

The explicit forms of the couplings are summarized as follows:

$$C_{111} = \frac{\lambda}{4}v\cos^3\alpha + \frac{\delta_2}{4}v\sin^2\alpha\cos\alpha + \frac{\delta_2}{4}v_S\sin\alpha\cos^2\alpha + \frac{d_2}{4}v_s\sin^3\alpha, \tag{D.22}$$

$$\begin{aligned} C_{112} =& -\frac{3\lambda}{4}v\sin\alpha\cos^2\alpha + \frac{\delta_2}{4}v(2\sin\alpha\cos^2\alpha - \sin^3\alpha), \\ &+ \frac{\delta_2}{4}v_S(\cos^3\alpha - 2\sin^2\alpha\cos\alpha) + \frac{3d_2}{4}v_s\sin^2\alpha\cos\alpha, \end{aligned} \tag{D.23}$$

$$\begin{aligned} C_{122} =& \frac{3\lambda}{4}v\sin^2\alpha\cos\alpha + \frac{\delta_2}{4}v(\cos^3\alpha - 2\sin^2\alpha\cos\alpha) \\ &- \frac{\delta_2}{4}v_S(2\sin\alpha\cos^2\alpha - \sin^3\alpha) + \frac{3d_2}{4}v_s\sin\alpha\cos^2\alpha, \end{aligned} \tag{D.24}$$

$$C_{222} = -\frac{\lambda}{4}v\sin^3\alpha - \frac{\delta_2}{4}v\sin\alpha\cos^2\alpha + \frac{\delta_2}{4}v_S\sin^2\alpha\cos\alpha + \frac{d_2}{4}v_s\cos^3\alpha, \tag{D.25}$$

$$C_{\chi\chi 1} = \frac{\delta_2}{4} v \cos\alpha + \frac{d_2}{4} v_S \sin\alpha, \tag{D.26}$$

$$C_{\chi\chi 2} = -\frac{\delta_2}{4} v \sin\alpha + \frac{d_2}{4} v_S \cos\alpha, \tag{D.27}$$

$$C_{1111} = \frac{\lambda}{16}\cos^4\alpha + \frac{\delta_2}{8}\sin^2\alpha\cos^2\alpha + \frac{d_2}{16}\sin^4\alpha, \tag{D.28}$$

$$C_{1112} = -\frac{\lambda}{4}\sin\alpha\cos\alpha^3 + \frac{\delta_2}{4}(\sin\alpha\cos\alpha^3 - \sin\alpha^3\cos\alpha) + \frac{d_2}{4}\sin^3\alpha\cos\alpha, \tag{D.29}$$

$$C_{1122} = \frac{3\lambda}{8}\sin^2\alpha\cos^2\alpha + \frac{\delta_2}{8}(\sin^4\alpha + \cos^4\alpha - 4\sin^2\alpha\cos^2\alpha) + \frac{3d_2}{8}\sin^2\alpha\cos^2\alpha, \tag{D.30}$$

$$C_{1222} = -\frac{\lambda}{4}\sin^3\alpha\cos\alpha + \frac{\delta_2}{4}(-\sin\alpha\cos^3\alpha + \sin^3\alpha\cos\alpha) + \frac{d_2}{4}\sin\alpha\cos^3\alpha, \tag{D.31}$$

$$C_{2222} = \frac{\lambda}{16}\sin^4\alpha + \frac{\delta_2}{8}\sin^2\alpha\cos^2\alpha + \frac{d_2}{16}\cos^4\alpha, \tag{D.32}$$

$$C_{\chi\chi 11} = \frac{\delta_2}{8}\cos^2\alpha + \frac{d_2}{8}\sin^2\alpha, \tag{D.33}$$

$$C_{\chi\chi 12} = -\frac{\delta_2}{4}\sin\alpha\cos\alpha + \frac{d_2}{4}\sin\alpha\cos\alpha, \tag{D.34}$$

$$C_{\chi\chi 22} = \frac{\delta_2}{8}\sin^2\alpha + \frac{d_2}{8}\cos^2\alpha, \tag{D.35}$$

$$C_{\chi\chi\chi\chi} = \frac{d_2}{16}. \tag{D.36}$$

Appendix E

Rephasing invariant CPV phases

In general CPV CxSM, the CPV arises from

$$-\mathcal{L}_Y^{\rm CPV} = \bar{q}_L \tilde{H} \left(Y^u + \frac{c_1^u}{\Lambda} S \right) u_R + \bar{q}_L H \left(Y^d + \frac{c_1^d}{\Lambda} S \right) d_R + \bar{\ell}_L H \left(Y^e + \frac{c_1^e}{\Lambda} S \right) e_R + a_1 S + \frac{b_1}{4} S^2 + \text{ H.c.}, \tag{E.1}$$

where all the couplings can be complex and denoted as $X = |X| e^{i\theta_X}$. However, these phases are not physical, so we obtain relative phases by rotating the fields as follows[1]:

$$q_L \to q'_L = e^{-i\theta_{q_L}} q_L, \quad u_R \to u'_R = e^{-i\theta_{u_R}} u_R, \quad d_R \to d'_R = e^{-i\theta_{d_R}} d_R \tag{E.2}$$

$$\ell_L \to \ell'_L = e^{-i\theta_{\ell_L}} \ell_L, \quad e_R \to e'_R = e^{-i\theta_{e_R}} e_R \tag{E.3}$$

$$H \to H' = e^{-i\theta_H} H, \quad S \to S' = e^{-i\theta_S} S. \tag{E.4}$$

Under the rotations, each phase transforms as

$$\theta_{Y^u} \to \theta'_{Y^u} = \theta_{Y_u} + \theta_{q_L} + \theta_H - \theta_{u_R}, \tag{E.5}$$

$$\theta_{Y^d} \to \theta'_{Y^d} = \theta_{Y_d} + \theta_{q_L} - \theta_H - \theta_{d_R}, \tag{E.6}$$

$$\theta_{Y^e} \to \theta'_{Y^e} = \theta_{Y^e} + \theta_{\ell_L} - \theta_H - \theta_{e_R}, \tag{E.7}$$

$$\theta_{c_1^u} \to \theta'_{c_1^u} = \theta_{c_1^u} + \theta_{q_L} + \theta_H - \theta_{u_R} - \theta_S, \tag{E.8}$$

$$\theta_{c_1^d} \to \theta'_{c_1^d} = \theta_{c_1^d} + \theta_{q_L} - \theta_H - \theta_{d_R} - \theta_S, \tag{E.9}$$

$$\theta_{c_1^e} \to \theta'_{c_1^e} = \theta_{c_1^e} + \theta_{\ell_L} - \theta_H - \theta_{e_R} - \theta_S, \tag{E.10}$$

$$\theta_{a_1} \to \theta'_{a_1} = \theta_{a_1} - \theta_S, \tag{E.11}$$

$$\theta_{b_1} \to \theta'_{b_1} = \theta_{b_1} - 2\theta_S. \tag{E.12}$$

[1]For simplicity, we consider one generation case.

Using Eqs. (E.5)-(E.12), one can find the rephasing invariant combination.

$$\theta_1 \equiv 2\theta_{a_1} - \theta_{b_1} \to 2\theta'_{a_1} - \theta'_{b_1} = 2\theta_{a_1} - \theta_{b_1}, \tag{E.13}$$

$$\theta_2 \equiv \theta_{Y^u} - \theta_{c_1^u} + \theta_{a_1} \to \theta'_{Y^u} - \theta'_{c_1^u} + \theta'_{a_1} = \theta_{Y^u} - \theta_{c_1^u} + \theta_{a_1}. \tag{E.14}$$

$$\theta_3 \equiv \theta_{Y^d} - \theta_{c_1^d} + \theta_{a_1} \to \theta'_{Y^d} - \theta'_{c_1^d} + \theta'_{a_1} = \theta_{Y^d} - \theta_{c_1^d} + \theta_{a_1}, \tag{E.15}$$

$$\theta_4 \equiv \theta_{Y^e} - \theta_{c_1^e} + \theta_{a_1} \to \theta'_{Y^e} - \theta'_{c_1^e} + \theta'_{a_1} = \theta_{Y^e} - \theta_{c_1^e} + \theta_{a_1}. \tag{E.16}$$

Thus, there are only four rephasing invariant phases.

Bibliography

[1] ATLAS collaboration, G. Aad et al., *Observation of a new particle in the search for the Standard Model Higgs boson with the ATLAS detector at the LHC*, *Phys. Lett. B* **716** (2012) 1–29, [1207.7214].

[2] CMS collaboration, S. Chatrchyan et al., *Observation of a New Boson at a Mass of 125 GeV with the CMS Experiment at the LHC*, *Phys. Lett. B* **716** (2012) 30–61, [1207.7235].

[3] B. D. Fields, K. A. Olive, T.-H. Yeh and C. Young, *Big-Bang Nucleosynthesis after Planck*, *JCAP* **03** (2020) 010, [1912.01132].

[4] Planck collaboration, N. Aghanim et al., *Planck 2018 results. VI. Cosmological parameters*, *Astron. Astrophys.* **641** (2020) A6, [1807.06209].

[5] A. D. Sakharov, *Violation of CP Invariance, C asymmetry, and baryon asymmetry of the universe*, *Pisma Zh. Eksp. Teor. Fiz.* **5** (1967) 32–35.

[6] M. Yoshimura, *Unified Gauge Theories and the Baryon Number of the Universe*, *Phys. Rev. Lett.* **41** (1978) 281–284.

[7] S. Weinberg, *Cosmological Production of Baryons*, *Phys. Rev. Lett.* **42** (1979) 850–853.

[8] V. A. Kuzmin, V. A. Rubakov and M. E. Shaposhnikov, *On the Anomalous Electroweak Baryon Number Nonconservation in the Early Universe*, *Phys. Lett.* **155B** (1985) 36.

[9] M. Fukugita and T. Yanagida, *Baryogenesis Without Grand Unification*, *Phys. Lett. B* **174** (1986) 45–47.

[10] M. B. Gavela, P. Hernandez, J. Orloff and O. Pene, *Standard model CP violation and baryon asymmetry*, *Mod. Phys. Lett. A* **9** (1994) 795–810, [hep-ph/9312215].

[11] M. B. Gavela, P. Hernandez, J. Orloff, O. Pene and C. Quimbay, *Standard model CP violation and baryon asymmetry. Part 2: Finite temperature*, *Nucl. Phys. B* **430** (1994) 382–426, [hep-ph/9406289].

[12] P. Huet and E. Sather, *Electroweak baryogenesis and standard model CP violation*, *Phys. Rev. D* **51** (1995) 379–394, [hep-ph/9404302].

[13] T. Konstandin, T. Prokopec and M. G. Schmidt, *Axial currents from CKM matrix CP violation and electroweak baryogenesis*, *Nucl. Phys. B* **679** (2004) 246–260, [hep-ph/0309291].

[14] K. Kajantie, M. Laine, K. Rummukainen and M. E. Shaposhnikov, *Is there a hot electroweak phase transition at $m_H \gtrsim m_W$?*, *Phys. Rev. Lett.* **77** (1996) 2887–2890, [hep-ph/9605288].

[15] K. Rummukainen, M. Tsypin, K. Kajantie, M. Laine and M. E. Shaposhnikov, *The Universality class of the electroweak theory*, *Nucl. Phys. B* **532** (1998) 283–314, [hep-lat/9805013].

[16] F. Csikor, Z. Fodor and J. Heitger, *Endpoint of the hot electroweak phase transition*, *Phys. Rev. Lett.* **82** (1999) 21–24, [hep-ph/9809291].

[17] Y. Aoki, F. Csikor, Z. Fodor and A. Ukawa, *The Endpoint of the first order phase transition of the SU(2) gauge Higgs model on a four-dimensional isotropic lattice*, *Phys. Rev. D* **60** (1999) 013001, [hep-lat/9901021].

[18] LZ collaboration, J. Aalbers et al., *First Dark Matter Search Results from the LUX-ZEPLIN (LZ) Experiment*, 2207.03764.

[19] V. Barger, P. Langacker, M. McCaskey, M. Ramsey-Musolf and G. Shaughnessy, *Complex Singlet Extension of the Standard Model*, *Phys. Rev. D* **79** (2009) 015018, [0811.0393].

[20] V. Barger, M. McCaskey and G. Shaughnessy, *Complex Scalar Dark Matter vis-\'a-vis CoGeNT, DAMA/LIBRA and XENON100*, *Phys. Rev. D* **82** (2010) 035019, [1005.3328].

[21] M. Gonderinger, H. Lim and M. J. Ramsey-Musolf, *Complex Scalar Singlet Dark Matter: Vacuum Stability and Phenomenology*, *Phys. Rev. D* **86** (2012) 043511, [1202.1316].

[22] G.-C. Cho, C. Idegawa and E. Senaha, *Electroweak phase transition in a complex singlet extension of the Standard Model with degenerate scalars*, *Phys. Lett. B* **823** (2021) 136787, [2105.11830].

[23] G.-C. Cho, C. Idegawa and R. Sugihara, *A complex singlet extension of the standard model and multi-critical point principle*, *Phys. Lett. B* **839** (2023) 137757, [2212.13029].

[24] G.-C. Cho and C. Idegawa, *Analyzing cancellation mechanism of the dark matter-quark scattering in a complex singlet extension of the Standard Model*, *Nucl. Phys. B* **994** (2023) 116320, [2304.10096].

[25] G.-C. Cho, C. Idegawa and E. Senaha, *CP-violating effects on gravitational waves in a complex singlet extension of the Standard Model with degenerate scalars*, *Phys. Rev. D* **106** (2022) 115012, [2205.12046].

[26] C. Idegawa and E. Senaha, *Electron electric dipole moment and electroweak baryogenesis in a complex singlet extension of the Standard Model with degenerate scalars*, 2309.09430.

[27] I. Affleck and M. Dine, *A New Mechanism for Baryogenesis*, *Nucl. Phys. B* **249** (1985) 361–380.

[28] F. R. Klinkhamer and N. S. Manton, *A Saddle Point Solution in the Weinberg-Salam Theory*, *Phys. Rev. D* **30** (1984) 2212.

[29] A. D. Linde, *Decay of the False Vacuum at Finite Temperature*, *Nucl. Phys. B* **216** (1983) 421.

[30] H. H. Patel and M. J. Ramsey-Musolf, *Baryon Washout, Electroweak Phase Transition, and Perturbation Theory*, *JHEP* **07** (2011) 029, [1101.4665].

[31] N. K. Nielsen, *On the Gauge Dependence of Spontaneous Symmetry Breaking in Gauge Theories*, *Nucl. Phys. B* **101** (1975) 173–188.

[32] R. Fukuda and T. Kugo, *Gauge Invariance in the Effective Action and Potential*, *Phys. Rev. D* **13** (1976) 3469.

[33] C.-W. Chiang, M. J. Ramsey-Musolf and E. Senaha, *Standard Model with a Complex Scalar Singlet: Cosmological Implications and Theoretical Considerations*, *Phys. Rev. D* **97** (2018) 015005, [1707.09960].

[34] C.-W. Chiang, Y.-T. Li and E. Senaha, *Revisiting electroweak phase transition in the standard model with a real singlet scalar*, *Phys. Lett. B* **789** (2019) 154–159, [1808.01098].

[35] R. R. Parwani, *Resummation in a hot scalar field theory*, *Phys. Rev. D* **45** (1992) 4695, [hep-ph/9204216].

[36] P. B. Arnold and O. Espinosa, *The Effective potential and first order phase transitions: Beyond leading-order*, *Phys. Rev.* **D47** (1993) 3546, [hep-ph/9212235].

[37] M. Joyce, T. Prokopec and N. Turok, *Electroweak baryogenesis from a classical force*, *Phys. Rev. Lett.* **75** (1995) 1695–1698, [hep-ph/9408339].

[38] M. Joyce, T. Prokopec and N. Turok, *Nonlocal electroweak baryogenesis. Part 1: Thin wall regime*, *Phys. Rev. D* **53** (1996) 2930–2957, [hep-ph/9410281].

[39] M. Joyce, T. Prokopec and N. Turok, *Nonlocal electroweak baryogenesis. Part 2: The Classical regime*, *Phys. Rev. D* **53** (1996) 2958–2980, [hep-ph/9410282].

[40] J. M. Cline, M. Joyce and K. Kainulainen, *Supersymmetric electroweak baryogenesis*, *JHEP* **07** (2000) 018, [hep-ph/0006119].

[41] L. Fromme and S. J. Huber, *Top transport in electroweak baryogenesis*, *JHEP* **03** (2007) 049, [hep-ph/0604159].

[42] J. M. Cline and K. Kainulainen, *Electroweak baryogenesis at high bubble wall velocities*, *Phys. Rev. D* **101** (2020) 063525, [2001.00568].

[43] P. Basler, M. Mühlleitner and J. Müller, *BSMPT v2 a tool for the electroweak phase transition and the baryon asymmetry of the universe in extended Higgs Sectors*, *Comput. Phys. Commun.* **269** (2021) 108124, [2007.01725].

[44] J. Hisano, R. Nagai and N. Nagata, *Effective Theories for Dark Matter Nucleon Scattering*, *JHEP* **05** (2015) 037, [1502.02244].

[45] J. Hisano, *Effective theory approach to direct detection of dark matter*, 1712.02947.

[46] S. Abe, G.-C. Cho and K. Mawatari, *Probing a degenerate-scalar scenario in a pseudoscalar dark-matter model*, *Phys. Rev. D* **104** (2021) 035023, [2101.04887].

[47] C. Gross, O. Lebedev and T. Toma, *Cancellation Mechanism for Dark-Matter–Nucleon Interaction*, *Phys. Rev. Lett.* **119** (2017) 191801, [1708.02253].

[48] CMS collaboration, V. Khachatryan et al., *Observation of the Diphoton Decay of the Higgs Boson and Measurement of Its Properties*, *Eur. Phys. J. C* **74** (2014) 3076, [1407.0558].

[49] E. Fuchs, S. Thewes and G. Weiglein, *Interference effects in BSM processes with a generalised narrow-width approximation*, *Eur. Phys. J. C* **75** (2015) 254, [1411.4652].

[50] B. Das, S. Moretti, S. Munir and P. Poulose, *Two Higgs bosons near 125 GeV in the NMSSM: beyond the narrow width approximation*, *Eur. Phys. J. C* **77** (2017) 544, [1704.02941].

[51] K. Sakurai and W. Yin, *Suppression of Higgs Mixing by Quantum Zeno Effect*, 2204.01739.

[52] LHC Higgs Cross Section Working Group collaboration, J. R. Andersen et al., *Handbook of LHC Higgs Cross Sections: 3. Higgs Properties*, 1307.1347.

[53] ATLAS collaboration, M. Aaboud et al., *Constraints on off-shell Higgs boson production and the Higgs boson total width in $ZZ \to 4\ell$ and $ZZ \to 2\ell 2\nu$ final states with the ATLAS detector*, *Phys. Lett. B* **786** (2018) 223–244, [1808.01191].

[54] CMS collaboration, A. Tumasyan et al., *Measurement of the Higgs boson width and evidence of its off-shell contributions to ZZ production*, *Nature Phys.* **18** (2022) 1329–1334, [2202.06923].

[55] D. L. Bennett and H. B. Nielsen, *Predictions for nonAbelian fine structure constants from multicriticality*, *Int. J. Mod. Phys. A* **9** (1994) 5155–5200, [hep-ph/9311321].

[56] D. L. Bennett and H. B. Nielsen, *Gauge couplings calculated from multiple point criticality yield alpha**(-1) = 136.8 +- 9: At last the elusive case of U(1)*, *Int. J. Mod. Phys. A* **14** (1999) 3313–3385, [hep-ph/9607278].

[57] D. L. Bennett, *Multiple point criticality, nonlocality, and fine tuning in fundamental physics: Predictions for gauge coupling constants gives alpha**-1 = 136.8 +- 9*, Ph.D. thesis, 5, 1996. hep-ph/9607341.

[58] C. D. Froggatt and H. B. Nielsen, *Standard model criticality prediction: Top mass 173 +- 5-GeV and Higgs mass 135 +- 9-GeV*, *Phys. Lett. B* **368** (1996) 96–102, [hep-ph/9511371].

[59] K. Kannike, N. Koivunen and M. Raidal, *Principle of Multiple Point Criticality in Multi-Scalar Dark Matter Models*, *Nucl. Phys. B* **968** (2021) 115441, [2010.09718].

[60] D. J. Chung, A. J. Long and L.-T. Wang, *125 gev higgs boson and electroweak phase transition model classes*, *Physical Review D* **87** (2013) 023509.

[61] G. Belanger, A. Mjallal and A. Pukhov, *Recasting direct detection limits within micrOMEGAs and implication for non-standard Dark Matter scenarios*, *Eur. Phys. J. C* **81** (2021) 239, [2003.08621].

[62] G.-C. Cho, C. Idegawa and R. Inumiya, *A complex singlet extension of the Standard Model with a singlet fermion dark matter*, 2312.05776.

[63] E. Witten, *Cosmic Separation of Phases*, *Phys. Rev. D* **30** (1984) 272–285.

[64] C. J. Hogan, *Gravitational radiation from cosmological phase transitions*, *Mon. Not. Roy. Astron. Soc.* **218** (1986) 629–636.

[65] M. Jiang, L. Bian, W. Huang and J. Shu, *Impact of a complex singlet: Electroweak baryogenesis and dark matter*, *Phys. Rev. D* **93** (2016) 065032, [1502.07574].

[66] W. Cheng and L. Bian, *From inflation to cosmological electroweak phase transition with a complex scalar singlet*, *Phys. Rev. D* **98** (2018) 023524, [1801.00662].

[67] B. Grzadkowski and D. Huang, *Spontaneous CP-Violating Electroweak Baryogenesis and Dark Matter from a Complex Singlet Scalar*, *JHEP* **08** (2018) 135, [1807.06987].

[68] N. Chen, T. Li, Y. Wu and L. Bian, *Complementarity of the future e^+e^- colliders and gravitational waves in the probe of complex singlet extension to the standard model*, *Phys. Rev. D* **101** (2020) 075047, [1911.05579].

[69] C. L. Wainwright, *CosmoTransitions: Computing Cosmological Phase Transition Temperatures and Bubble Profiles with Multiple Fields*, *Comput. Phys. Commun.* **183** (2012) 2006–2013, [1109.4189].

[70] K. Funakubo, A. Kakuto, S. Otsuki, K. Takenaga and F. Toyoda, *CP violating profile of the electroweak bubble wall*, *Prog. Theor. Phys.* **94** (1995) 845–860, [hep-ph/9507452].

[71] K. Funakubo, S. Otsuki and F. Toyoda, *Transitional CP violation in the MSSM and electroweak baryogenesis*, *Prog. Theor. Phys.* **102** (1999) 389–406, [hep-ph/9903276].

[72] S. J. Huber, P. John, M. Laine and M. G. Schmidt, *CP violating bubble wall profiles*, *Phys. Lett. B* **475** (2000) 104–110, [hep-ph/9912278].

[73] S. J. Huber and M. G. Schmidt, *Electroweak baryogenesis: Concrete in a SUSY model with a gauge singlet*, *Nucl. Phys. B* **606** (2001) 183–230, [hep-ph/0003122].

[74] S. J. Huber, P. John and M. G. Schmidt, *Bubble walls, CP violation and electroweak baryogenesis in the MSSM*, *Eur. Phys. J. C* **20** (2001) 695–711, [hep-ph/0101249].

[75] C. Grojean and G. Servant, *Gravitational Waves from Phase Transitions at the Electroweak Scale and Beyond*, *Phys. Rev. D* **75** (2007) 043507, [hep-ph/0607107].

[76] C. Caprini et al., *Science with the space-based interferometer eLISA. II: Gravitational waves from cosmological phase transitions*, *JCAP* **04** (2016) 001, [1512.06239].

[77] A. Kosowsky, M. S. Turner and R. Watkins, *Gravitational radiation from colliding vacuum bubbles*, *Phys. Rev. D* **45** (Jun, 1992) 4514–4535.

[78] A. Kosowsky, M. S. Turner and R. Watkins, *Gravitational waves from first-order cosmological phase transitions*, *Phys. Rev. Lett.* **69** (Oct, 1992) 2026–2029.

[79] A. Kosowsky and M. S. Turner, *Gravitational radiation from colliding vacuum bubbles: envelope approximation to many bubble collisions*, *Phys. Rev. D* **47** (1993) 4372–4391, [astro-ph/9211004].

[80] M. Kamionkowski, A. Kosowsky and M. S. Turner, *Gravitational radiation from first order phase transitions*, *Phys. Rev. D* **49** (1994) 2837–2851, [astro-ph/9310044].

[81] C. Caprini, R. Durrer and G. Servant, *Gravitational wave generation from bubble collisions in first-order phase transitions: An analytic approach*, *Phys. Rev. D* **77** (2008) 124015, [0711.2593].

[82] S. J. Huber and T. Konstandin, *Gravitational Wave Production by Collisions: More Bubbles*, *JCAP* **09** (2008) 022, [0806.1828].

[83] M. Hindmarsh, S. J. Huber, K. Rummukainen and D. J. Weir, *Gravitational waves from the sound of a first order phase transition*, *Phys. Rev. Lett.* **112** (2014) 041301, [1304.2433].

[84] J. T. Giblin, Jr. and J. B. Mertens, *Vacuum Bubbles in the Presence of a Relativistic Fluid*, *JHEP* **12** (2013) 042, [1310.2948].

[85] J. T. Giblin and J. B. Mertens, *Gravitional radiation from first-order phase transitions in the presence of a fluid*, *Phys. Rev. D* **90** (2014) 023532, [1405.4005].

[86] M. Hindmarsh, S. J. Huber, K. Rummukainen and D. J. Weir, *Numerical simulations of acoustically generated gravitational waves at a first order phase transition*, *Phys. Rev. D* **92** (2015) 123009, [1504.03291].

[87] C. Caprini and R. Durrer, *Gravitational waves from stochastic relativistic sources: Primordial turbulence and magnetic fields*, *Phys. Rev. D* **74** (2006) 063521, [astro-ph/0603476].

[88] T. Kahniashvili, A. Kosowsky, G. Gogoberidze and Y. Maravin, *Detectability of Gravitational Waves from Phase Transitions*, *Phys. Rev. D* **78** (2008) 043003, [0806.0293].

[89] T. Kahniashvili, L. Campanelli, G. Gogoberidze, Y. Maravin and B. Ratra, *Gravitational Radiation from Primordial Helical Inverse Cascade MHD Turbulence*, *Phys. Rev. D* **78** (2008) 123006, [0809.1899].

[90] T. Kahniashvili, L. Kisslinger and T. Stevens, *Gravitational Radiation Generated by Magnetic Fields in Cosmological Phase Transitions*, *Phys. Rev. D* **81** (2010) 023004, [0905.0643].

[91] C. Caprini, R. Durrer and G. Servant, *The stochastic gravitational wave background from turbulence and magnetic fields generated by a first-order phase transition*, *JCAP* **12** (2009) 024, [0909.0622].

[92] P. Binetruy, A. Bohe, C. Caprini and J.-F. Dufaux, *Cosmological Backgrounds of Gravitational Waves and eLISA/NGO: Phase Transitions, Cosmic Strings and Other Sources*, *JCAP* **06** (2012) 027, [1201.0983].

[93] TianQin collaboration, J. Luo et al., *TianQin: a space-borne gravitational wave detector*, *Class. Quant. Grav.* **33** (2016) 035010, [1512.02076].

[94] X.-C. Hu, X.-H. Li, Y. Wang, W.-F. Feng, M.-Y. Zhou, Y.-M. Hu et al., *Fundamentals of the orbit and response for TianQin*, *Class. Quant. Grav.* **35** (2018) 095008, [1803.03368].

[95] W.-R. Hu and Y.-L. Wu, *The Taiji Program in Space for gravitational wave physics and the nature of gravity*, *Natl. Sci. Rev.* **4** (2017) 685–686.

[96] W.-H. Ruan, Z.-K. Guo, R.-G. Cai and Y.-Z. Zhang, *Taiji program: Gravitational-wave sources*, *Int. J. Mod. Phys. A* **35** (2020) 2050075, [1807.09495].

[97] P. Amaro-Seoane, H. Audley, S. Babak, J. Baker, E. Barausse, P. Bender et al., *Laser interferometer space antenna*, *arXiv preprint arXiv:1702.00786* (2017) .

[98] C. Caprini et al., *Detecting gravitational waves from cosmological phase transitions with LISA: an update*, *JCAP* **03** (2020) 024, [1910.13125].

[99] N. Seto, S. Kawamura and T. Nakamura, *Possibility of direct measurement of the acceleration of the universe using 0.1-Hz band laser interferometer gravitational wave antenna in space*, *Phys. Rev. Lett.* **87** (2001) 221103, [astro-ph/0108011].

[100] S. Kawamura et al., *The Japanese space gravitational wave antenna DECIGO*, *Class. Quant. Grav.* **23** (2006) S125–S132.

[101] V. Corbin and N. J. Cornish, *Detecting the cosmic gravitational wave background with the big bang observer*, *Class. Quant. Grav.* **23** (2006) 2435–2446, [gr-qc/0512039].

[102] J. R. Espinosa, B. Gripaios, T. Konstandin and F. Riva, *Electroweak Baryogenesis in Non-minimal Composite Higgs Models*, *JCAP* **01** (2012) 012, [1110.2876].

[103] J. M. Cline and K. Kainulainen, *Electroweak baryogenesis and dark matter from a singlet Higgs*, *JCAP* **01** (2013) 012, [1210.4196].

[104] J. M. Cline, A. Friedlander, D.-M. He, K. Kainulainen, B. Laurent and D. Tucker-Smith, *Baryogenesis and gravity waves from a UV-completed electroweak phase transition*, *Phys. Rev. D* **103** (2021) 123529, [2102.12490].

[105] ACME collaboration, V. Andreev et al., *Improved limit on the electric dipole moment of the electron*, *Nature* **562** (2018) 355–360.

[106] T. S. Roussy et al., *An improved bound on the electron's electric dipole moment*, *Science* **381** (2023) adg4084, [2212.11841].

[107] S. M. Barr and A. Zee, *Electric Dipole Moment of the Electron and of the Neutron*, *Phys. Rev. Lett.* **65** (1990) 21–24.

[108] T. Abe, J. Hisano, T. Kitahara and K. Tobioka, *Gauge invariant Barr-Zee type contributions to fermionic EDMs in the two-Higgs doublet models*, *JHEP* **01** (2014) 106, [1311.4704].

[109] Particle Data Group collaboration, R. L. Workman et al., *Review of Particle Physics*, *PTEP* **2022** (2022) 083C01.

[110] M. Quiros, *Field theory at finite temperature and phase transitions*, *Helv. Phys. Acta* **67** (1994) 451–583.

[111] G. Passarino and M. J. G. Veltman, *One Loop Corrections for e+ e- Annihilation Into mu+ mu- in the Weinberg Model*, *Nucl. Phys. B* **160** (1979) 151–207.